Photonic Crystal Fibres for Coherent Supercontinuum Generation

Hooper, Lucy

Award date:
2012

Awarding institution:
University of Bath

Photonic Crystal Fibres for Coherent Supercontinuum Generation

submitted by

Lucy Ellen Hooper

for the degree of Doctor of Philosophy

of the

University of Bath

Department of Physics

January 2012

Summary

In this research photonic crystal fibres were developed for the purpose of generating coherent supercontinua. Two photonic crystal fibres were fabricated with all-normal group velocity dispersion profiles, with low dispersion at pump wavelengths 800 nm and 1064 nm. Supercontinua generated using these fibres were shown to have superior stability and coherence compared with supercontinua generated in fibres with anomalous dispersion at the pump wavelength.

Using a short piece of photonic crystal fibre with all-normal group velocity dispersion, pumped at 1064 nm, a self phase modulation spectrum spanning 200 nm was generated. The supercontinuum was re-compressed using linear chirp compensation to 26 fs, which was within a factor of two of the theoretical transform limit. This demonstrates the high spectral coherence, stability, and almost-linear chirp of the supercontinuum. Simulations showed that pulse compression using a supercontinuum generated in a photonic crystal fibre with anomalous dispersion at the pump wavelength would be limited by shot-to-shot fluctuations in the spectral intensity and phase, and the nonlinear chirp.

Using a longer piece of all-normal dispersion photonic crystal fibre, supercontinuum is generated by self phase modulation, and optical wave breaking. A broad flat supercontinuum spanning 700 nm, centred at 1064 nm was generated. This supercontinuum was spectrally filtered, and the pulses obtained analysed in the temporal domain. Clean, stable sub-picosecond pulses were achieved, demonstrating the applicability of such a supercontinuum as part of a compact, tunable laser source. The same experiment was carried out using a photonic crystal fibre with anomalous dispersion at the pump wavelength, resulting in pulses with a large portion of energy contained in broad shoulders, and higher order modes.

Interferometric coherence measurements were carried out at 800 nm using a Ti:Sapphire laser. A supercontinuum was generated in all-normal dispersion photonic crystal fibre with low dispersion at 800 nm, spanning 400 nm. Supercontinuum pulses generated by consecutive laser pulses were brought together in time using an interferometer. The interference between consecutive pulses was viewed spectrally, and the interference fringes had high visibility across the whole supercontinuum bandwidth. This demonstrates high spectral coherence. A supercontinuum generated in photonic crystal fibre with anomalous dispersion at 800 nm was tested in the same way, and the interference fringes obtained had lower visibility, indicating low spectral coherence.

The research presented demonstrates that photonic crystal fibres with all-normal dispersion profiles can be used to generate supercontinua with high coherence and intensity stability. This type of supercontinuum is applicable to ultra-short pulse compression, and can be spectrally filtered to create a broadband tunable ultra-short laser source.

Acknowledgements

First of all, thank you Jonathan for believing in me, and for all of your advice and support over the last three years.

Pete, thanks for all the time spent in the lab, for being a great teacher, and for reading this thesis.

Ali, thanks for helping me to get started, and since then for being an equipment-lender, a chapter-reader and a tea-buyer.

William, thank you for all of your invaluable advice and suggestions.

Steve, Alan and Brian, thank you for all of your practical advice on drawing fibres, and help in the fibre drawing tower.

Thank you to Fei and Brian for fabricating some of the all-normal dispersion fibres.

Jim, thanks for providing me with nice noisy supercontinuum fibres.

And to everyone else in the CPPM, past and present, thanks for making it a nice place to work.

Thanks also to John Dudley, for allowing me use your GNLSE code, and especially for the time you devoted to teaching me how to use it.

Thanks also to Philipp Kukura's group in Oxford for allowing us to use their laser.

Finally thanks to Rob, for always being there for me.

Contents

Introduction

The research described in this thesis concerns supercontinuum generation. A supercontinuum is a broad spectrum which has been generated through nonlinear optical effects, usually by propagating high intensity laser light in a highly nonlinear bulk medium or optical fibre. Nonlinear optical effects are a result of the nonlinear response of the bound electrons in a dielectric medium when subject to an intense field, for example a high-power ultra-short pulsed laser. Nonlinear optical effects usually result in the generation of new frequencies, and thus can increase the spectral bandwidth of an originally narrow-band pump. A common method for the generation of supercontinuum is to use highly nonlinear photonic crystal fibres (PCF). These are micro-structured optical fibres, usually consisting of fused silica with a lattice of air holes which run the entire length of the fibre. The micro-structure is on the scale of a wavelength of light, which gives the fibre some interesting properties. PCF have two properties which make them superior to conventional solid optical fibres for supercontinuum generation. Firstly the refractive index contrast between the core and the cladding can be much higher in PCF, allowing for tighter confinement to the core, and therefore enhanced nonlinearity. Secondly the group velocity dispersion of PCF can be modified to a greater extent, which is important for controlling the nonlinear dynamics, and is of key importance in the research presented in this thesis. Supercontinua generated in PCF have many applications in physics, chemistry and biology, due to their high brightness and spatial coherence, and have therefore been extensively researched over the past decade.

Group velocity dispersion (GVD) arises from the frequency dependence of the refractive index, and in the absence of nonlinear optical effects causes the frequency components of a laser pulse to spread apart in time. Group velocity dispersion is conventionally described in two regimes; "normal" GVD means that low frequencies have a higher group velocity than high frequencies, and "anomalous" GVD means that the opposite is true.

A common method of generating a broadband supercontinuum in PCF is to use a laser with a central wavelength in the anomalous GVD regime of the fibre. In this case, nonlinearity and dispersion act against one another, forming pulses known as solitons. These solitons are very sensitive to perturbations and break down in a process which results in a broad supercontinuum. However, the break down process is very sensitive to laser noise, and results in a spectrum which fluctuates in intensity and phase from one laser pulse to the next. The unstable spectral intensity and phase results in poor spectral coherence. Although the laser technical noise can

be reduced by improving laser design, there exist fundamental quantum fluctuations inside the laser cavity which are significant enough to completely destroy the coherence in some cases.

The aim of this research was to develop PCFs which can be used to generate a stable and coherent supercontinuum light source. Supercontinuum stability is essential for many applications, including ultra-short pulse generation, frequency metrology, spectroscopy and microscopy. The solution implemented in this work was to generate supercontinuum in the normal GVD regime of a PCF, in which solitons are prohibited from forming, thus eliminating unwanted noisy effects. Under normal GVD, nonlinearity and dispersion compound one another, and spectral broadening occurs via self phase modulation, which is not sensitive to pump pulse fluctuations. A disadvantage of pumping in the normal GVD regime is that rapid temporal broadening occurs, limiting the achievable bandwidth. Due to the wide dispersion engineering capability of PCF, it is possible to fabricate PCF which have normal GVD at all wavelengths. However this condition is only true over a narrow range of structural parameters of the micro-structure array, and therefore requires precision during the fabrication process.

This thesis is organised as follows:

Chapter 1 provides an introduction to optical fibres and PCF, including fabrication methods. The chapter then concentrates on the important linear optical properties including guidance mechanisms, dispersion, loss and birefringence.

Chapter 2 introduces nonlinear optics, and focuses on nonlinear optical effects which can contribute to supercontinuum generation in PCF. The interplay between dispersion and nonlinearity, and the dynamics of supercontinuum generation in various dispersion regimes are explained. Finally, a generalised nonlinear Schrödinger equation solver code used to simulate nonlinear pulse propagation is described.

Chapter 3 describes the overall process of designing and fabricating all-normal GVD PCFs. This includes numerical modelling of fibre dispersion, stack design, fibre draw details and fibre dispersion measurements.

Chapter 4 contains the results of pulse re-compression of an all-normal GVD supercontinuum. Using only linear chirp compensation, the supercontinuum pulses generated in a short length of all-normal GVD PCF can be compressed to 26 fs, which is within a factor of two of the theoretical minimum compressed pulse duration. This demonstrates high spectral coherence and stability. Simulations show that a supercontinuum generated in anomalous GVD PCF using the same input pulses would not be compressible using linear chirp compensation.

Chapter 5 demonstrates that a tunable coherent source of picosecond pulses can be obtained by spectral filtering of an all-normal GVD supercontinuum. Results obtained when filtering an anomalous GVD supercontinuum were found to be inferior.

Chapter 6 contains results of interferometric coherence measurements, using a delayed pulse method. The visibility of the interference fringes obtained in this experiment is directly linked

to the spectral coherence. Full fringe visibility was observed for the all-normal GVD supercontinuum. For comparison, the coherence of a supercontinuum generated in a PCF with anomalous GVD at the pump wavelength was measured. This displayed low spectral coherence outside the vicinity of the pump wavelength.

This thesis ends with a concluding chapter which also contains proposals for further research.

Chapter 1

Optical fibres

1.1 Introduction

This chapter contains an introduction to optical fibres, focusing on the linear properties which are essential for understanding the theory and results presented in later chapters. Firstly conventional all-solid step-index fibres, and photonic crystal fibres and their fabrication are described. Linear propagation in optical fibres is described by introducing the propagation constant β, which has a dependence on optical frequency. This dependence on frequency gives rise to group velocity dispersion. It is then shown that group velocity dispersion can be widely engineered in photonic crystal fibres due to a strong contribution from waveguide dispersion. A method for measuring group velocity dispersion in an optical fibre is also described. Other important properties of photonic crystal fibres such as loss, band gap guidance and birefringence are then briefly explained.

1.2 Standard step-index fibre

Conventional silica fibres are optical waveguides consisting of a core with high refractive index, surrounded by a cladding material with lower index. Because of this index contrast, guidance of light in the core can occur by total internal reflection. Figure 1-1 shows a typical refractive index profile for a "step index" fibre. Other refractive index profiles exist; some fibres are "graded index" where the refractive index is slowly reduced as a function of fibre radius, and there are other more exotic index profiles available depending on the application [1]. Optical fibres are typically 125 μm in diameter, and the diameter of the core can range from a few microns to tens of microns.

Guiding light via total internal reflection in a strand of dielectric material was first demonstrated in the 19th century, in a stream of water [2]. This was later extended to guiding light in glass strands [3]. In the 1950s, the concept of adding a cladding with lower index to the outside of a glass fibre was introduced [4]. This improved transmission properties because it removed the problem of scattering at the dielectric surface. Since the 1950s the transmission in optical

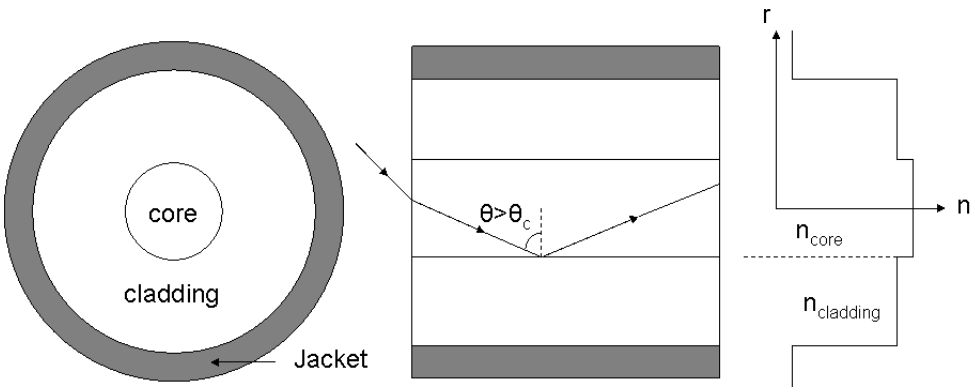

Figure 1-1: Left to right: Step-index fibre cross-section, guidance by total internal reflection in the fibre core, and the refractive index profile cross the fibre diameter

fibres has been slowly improved from 1% over a km in 1970 to 96% over a km in 1990 [5]. The invention of the laser in 1960 [6] aided the transmission of data over long distances using light. Communications systems based on optical fibres can have a large bandwidth, and are less prone to cross-talk than traditional copper wires. Since the first transatlantic fibre optics cable was laid in 1988 [7], they have become commonplace in telecommunications systems, making this their most well-known application. However, optical fibre applications are not only limited to telecommunications. The ability to deliver light from one place to another is useful for medical applications, for example imaging using endoscopes. They can also be used for astronomy [8], sensing [9], and used to form lasers [10, 11]. In the field of nonlinear optics they are of vital importance, because they allow tight confinement of light over a long interaction length.

Optical fibres are often fabricated from silica glass. The transparency window of silica covers the entire range of visible wavelengths and into the infra red, and it is easy to draw into fibres due to its slow variation of viscosity with temperature. It is also inexpensive, as the raw material needed to make it (sand) is abundantly available. In step-index fibres, the refractive index of silica glass is modified by adding dopants. The core index can be increased by doping with germanium or phosphorous, or the cladding index can be reduced by doping with boron or fluorine [12]. Step-index fibres are generally fabricated using vapour deposition techniques [1]. This process is used to create a macroscopic version of the desired final structure, known as a "preform". This is typically 1 metre long and a few centimetres in diameter. The preform is then drawn to fibre on a fibre drawing tower, which is described in more detail in section 1.3.1.

1.3 Photonic crystal fibre

Photonic crystals are dielectric periodic structures on the scale of a wavelength of light. Photonic crystals can be incorporated into the cladding of an optical fibre, producing photonic crystal fibres (PCFs). These types of fibres were first introduced in the 1990s [13]. Photonic

crystals have some unique properties which set PCF apart from conventional optical fibre technology. Figure 1-2 contains examples of various types of PCF. Usually PCF are fabricated from silica, with an array of air holes in the cladding which run the entire length of the fibre. Alternatively, doped silica rods can be used instead of air, or the air holes can be filled after fabrication with liquid or gas.

PCFs can be split into two main groups - index guiding PCF and band gap guiding PCF. Index guiding PCF have a solid core, which is a defect in the air-hole array, or in other words, a missing hole. Examples of these are shown in figure 1-2 (a) and (b). Guidance in solid-core PCF occurs in a similar way to total internal reflection in conventional fibres. The effective refractive index of the air hole lattice in the cladding is lower than the refractive index of the core material, and so guidance occurs via "modified total internal reflection".

There are two main properties of the photonic crystal cladding which allow new capabilities in PCF. First is the large core-cladding index contrast achievable in silica-air fibres. This allows higher confinement to the core and therefore increases nonlinearity [14]. The index contrast also increases the contribution of waveguide dispersion to overall dispersion, meaning the dispersion engineering capability is much higher than in conventional fibres. Dispersion engineering in PCF is key to the experimental work in subsequent chapters, and is discussed in more detail in section 1.5.2. The second important property of the PCF cladding is the photonic band gap effect, which is described in more detail in section 1.7. This effect allows light to be guided in a low-index core, such as a hollow air core, as can be seen in figure 1-2 (c) and (f). Figure 1-2 (d) is another band gap guiding PCF, made from fused silica with an array of high index rods in the cladding to provide the photonic band gap.

The dimensions of the photonic crystal cladding are described using the hole-to-hole spacing, or pitch (Λ), and the hole diameter (d). These are illustrated in figure 1-3. By changing the pitch and hole size, the dispersion and nonlinearity can be changed. The number of rings of air holes in the cladding is also an important quantity, impacting on confinement loss (see section 1.6). The birefringence of PCF can be modified easily by introducing two-fold symmetry to the cladding, as illustrated in the highly birefringent PCF in figure 1-2 (e). Fibre birefringence is discussed in more detail in section 1.8. PCF can also be fabricated with multiple cores [15] to provide a high packing density of cores for endoscopy applications, or to provide cores with different properties suitable for pulse delivery and collection [16]. Air-silica PCFs are useful for sensing, because gases and liquids are able to penetrate into the air holes either from the fibre end or by drilling holes at regular intervals into the cladding along the length of the fibre [17]. Hollow core PCF can be filled with gases [18] and liquids [19] in order to increase their nonlinearity, and they can also be used to confine and guide particles [20, 21].

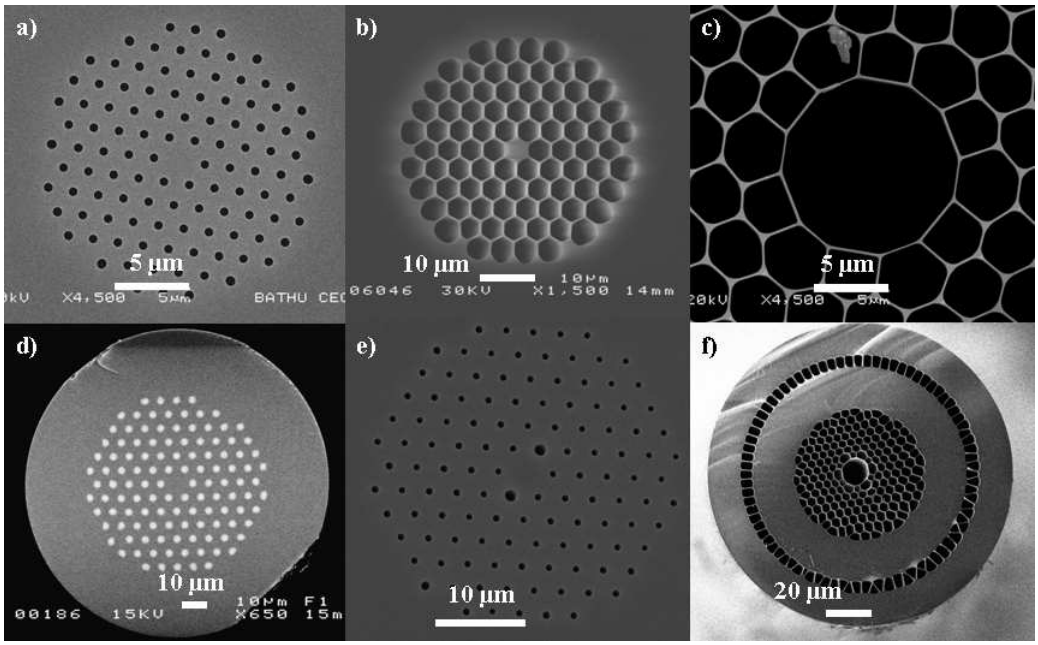

Figure 1-2: Scanning electron microscope images of photonic crystal fibres; a) solid core fibre, b) high air filling fraction solid core fibre, c) hollow core fibre, d) solid band-gap fibre consisting of a mixture of doped silica glasses, e) a birefringent solid core fibre, f) double-clad hollow core fibre. Images are courtesy of Jim Stone, Brian Mangan, Laure Lavoute and Alistair Muir

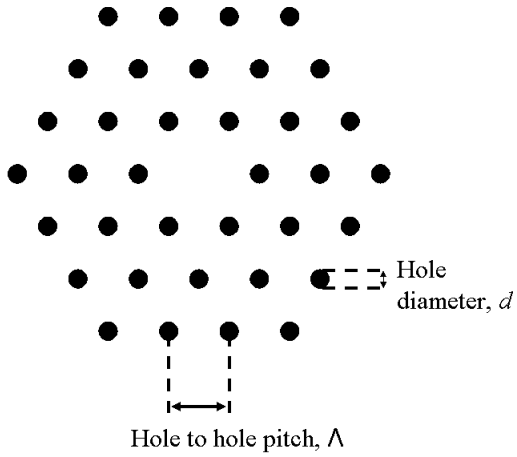

Figure 1-3: Representation of a cross-section of solid core photonic crystal fibre, showing important structural parameters pitch Λ and hole diameter d

1.3.1 Fabrication

PCFs can be fabricated using a variety of different materials, and methods. The vapour deposition techniques used for conventional fibres are not practical for the creation of PCF. The most common method is the stack and draw method, which involves stacking capillaries and rods, which are then drawn down to create a preform. This is the method used to fabricate the all-normal group velocity dispersion PCFs described in chapter 3.

Most fibre fabrication techniques, including the stack and draw method, use a fibre drawing tower. Figure 1-4 shows a schematic representation of a fibre drawing tower system. The basic idea is that the material to be drawn is clamped above the furnace, and lowered into it. The furnace heats the preform to a temperature of approximately 2000 °C. The preform is then fed into the furnace at a relatively low speed (mm/min) and the glass emerging from the bottom of the furnace is pulled at a higher speed (usually m/min).

The overall procedure for the stack and draw method is shown in figure 1-5. Firstly the capillaries and rods required to build the stack are drawn on the fibre drawing tower. The starting materials are fused silica rods and tubes which are produced commercially, and are typically 1 m long and 2-3 cm in diameter. The final capillaries and rods typically have a length of 1 m and a diameter of around 1 mm. These are then stacked by hand in a hexagonal arrangement. Solid core fibres have a solid rod at the centre of the capillary array to act as the core. Hollow core fibres are created by simply removing some of the central capillaries. The stack is then inserted into another fused silica tube, known as the jacketing tube, which is again around 1 m long and a few centimetres in diameter. To make sure the hexagonal array of capillaries fits snugly inside the circular jacketing tube, the corner capillaries of the array are removed, and solid packing rods are added to make the stack approximately circular. A typical stack design is shown in figure 1-6 (a), and a photograph of a stack is shown in figure 1-7.

PCF stacks are generally drawn to fibre in two stages. In the first step the stack is drawn into canes, which are generally a few millimetres thick and 1 m in length. A microscope image of a typical PCF cane is shown in figure 1-6 (b). When drawing canes a vacuum is applied to the space around the outside of the capillaries, to encourage them to fuse to form a structure close to the desired PCF structure. The canes are stiff, and are pulled using the cane puller (see figure 1-4), which is a pair of rotating rubber bands which grip the cane.

In the second step a cane is inserted inside another jacketing tube, to create a preform. The preform is then drawn to fibre. Pressure typically in the region 10-30 kPa is applied to the air holes and a vacuum is applied to the space between the cane and the jacketing tube. Scanning electron microscope images of fibres drawn from the same cane, with low and high pressure applied to the holes are shown in figure 1-6 (c) and (d) respectively. As the fibre emerges from the furnace it passes through a coating die and UV curer, which coats it in a layer of polymer to increase its strength. The final fibre is flexible enough to be wound onto a collection spool, and typically several kilometres of fibre can be collected during one fibre draw.

PCF can also be fabricated by extrusion. Molten glass is forced through a die which moulds it to the correct structure [23]. This can be used to create structures not possible using stack and

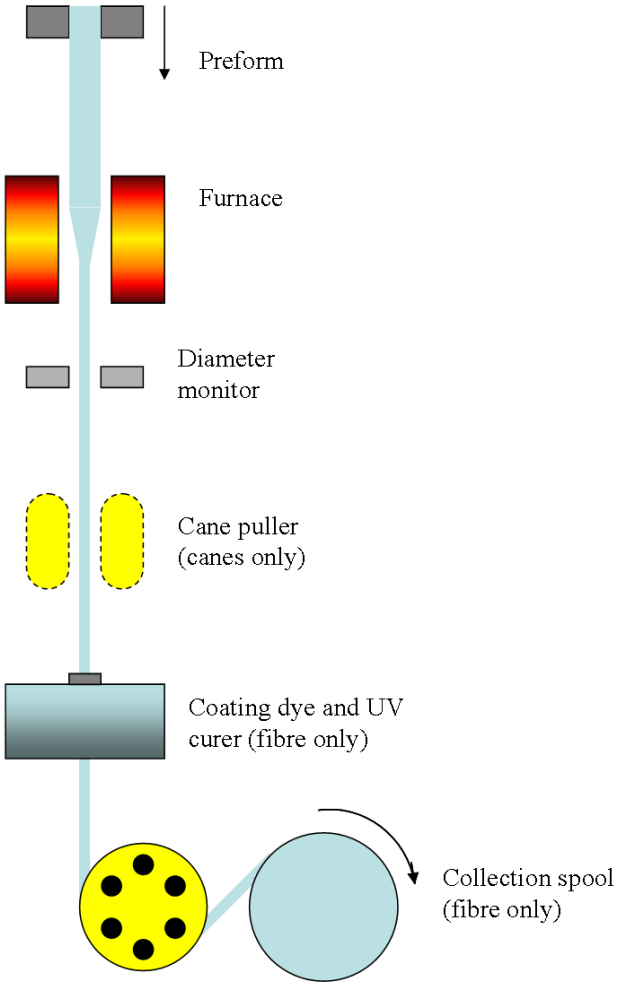

Figure 1-4: Schematic illustration of fibre drawing tower

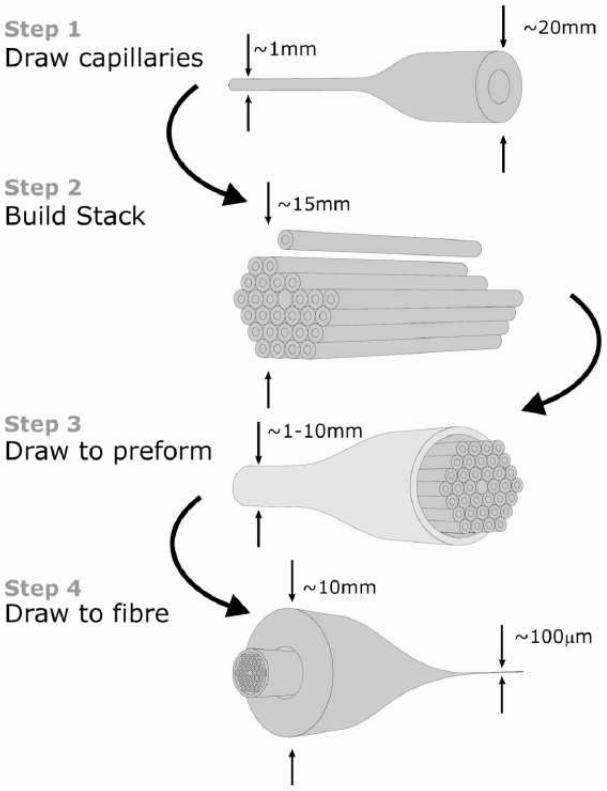

Figure 1-5: Procedure for fabrication of photonic crystal fibres using the stack and draw method [22]

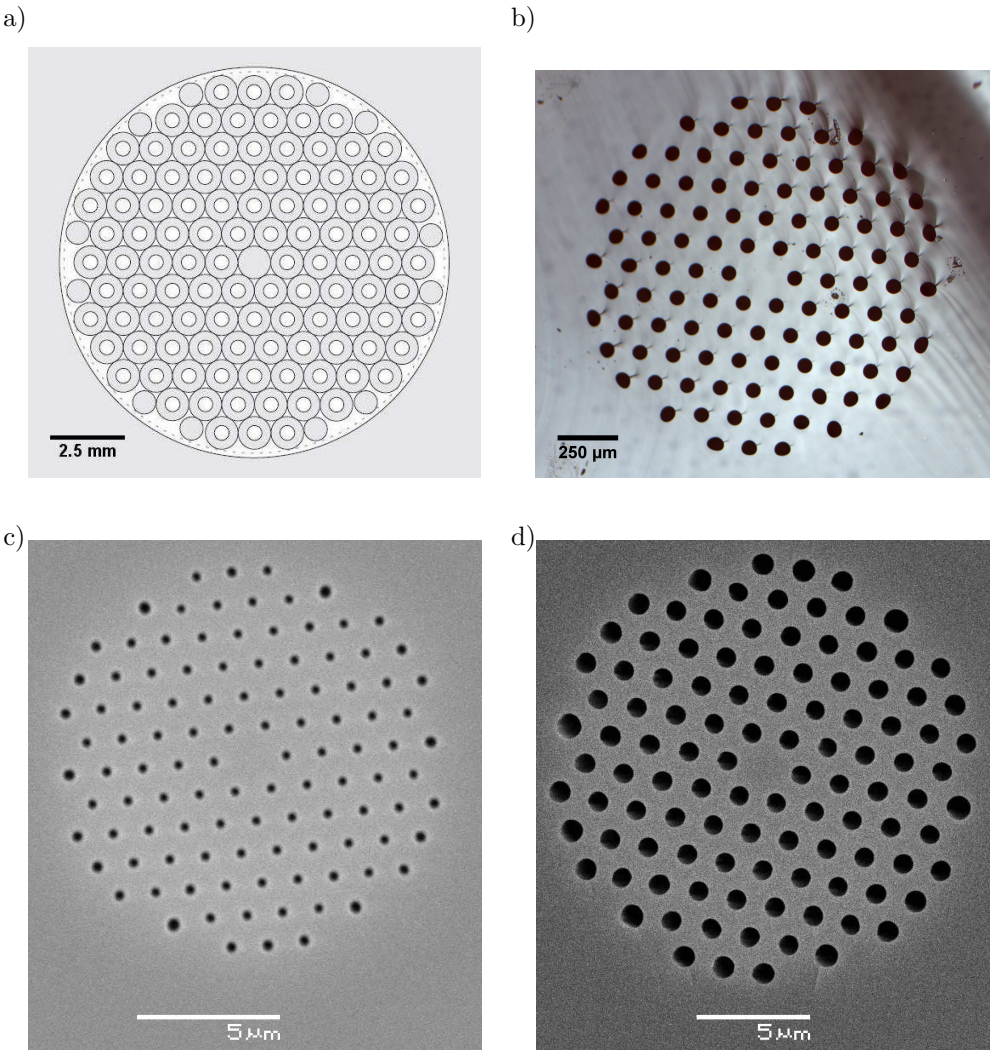

Figure 1-6: a) Typical solid core stack design, b) Optical microscope image of corresponding cane cross section, c) and d) Scanning electron microscope images of two different fibres which can be fabricated from the cane shown in (b) by applying different pressures during the fibre draw

Figure 1-7: Photograph of a solid core fibre stack, inserted into a jacketing tube, ready to be drawn to canes

draw method, and is useful when using materials such as doped silica, polymer, or chalcogenide glasses which are not commonly available in tube form. Another possible method for creating a preform is to drill holes in a solid glass or polymer rod. In this case the preform length is limited by the maximum drill-hole depth.

1.4 The propagation constant β

The ray optics representation of light guidance in an optical fibre, shown in figure 1-1 is only valid for fibres with a core diameter which is large compared to the wavelength of light. Most optical fibres, especially those used in nonlinear optics, have core diameters comparable to the wavelength of light. In this case the wave nature of light plays a role, namely diffraction effects must be taken into account [24]. This leads to discrete "modes" of light propagation in the fibre. A mode is a solution of Maxwell's equations and the boundary conditions imposed by the fibre [12]. Physically, it is a light wave which propagates without change of its field distribution, except for the phase.

Each mode has effective refractive index $n_{\text{eff}} = \beta/k_0$ where $k_0 = 2\pi/\lambda$ is the wave number where λ is the wavelength, and the propagation constant β is the component of the wave-vector parallel to the fibre axis [25]. A bound mode (a mode which is confined to the fibre core via total internal reflection) will have an effective index, n_{eff} which satisfies $n_{\text{core}} > n_{\text{eff}} > n_{\text{cladding}}$. The mode with the highest n_{eff} is the "fundamental mode", and all modes with smaller values of n_{eff} are higher order modes. Fibres which guide only the fundamental mode are known as "single-mode", and fibres which can guide higher order modes are known as "multi-mode". A useful parameter which provides an indication of the number of modes supported by a fibre is

the V parameter, given by [12]

$$V = k_0 \rho (n_{co}^2 - n_{cl}^2)^{1/2} \tag{1.1}$$

where ρ is the core radius, and n_{co} and n_{cl} are the refractive indices of the core and cladding respectively. If $V < 2.404$ then the fibre is single mode, and otherwise it is multi mode. This thesis generally deals with single-mode propagation, unless otherwise indicated.

It can be seen from equation 1.1 that the larger the index contrast between the core and the cladding, or the larger the core, the more modes the fibre can support. This can be understood by thinking about the confinement of light in the core being analogous to electrons confined in a potential well. For a higher index contrast (higher 'sides' of the potential well), more modes can be confined. Similarly, for a larger core (wider potential well), more modes are confined.

Each mode propagates along the fibre with a different velocity, determined by its propagation constant. A pulse of light in a multi-mode fibre will therefore spread out as it propagates, and this is known as "intermodal dispersion" [12]. Using equation 1.1 it is possible to design a step index fibre which is "single mode" at a specified wavelength. At some shorter wavelength the fibre will support more than one mode. Conversely, it is possible to make PCF "endlessly single mode", in the case where the waveguide dispersion counteracts the dependence of the V parameter on wavelength [26]. It is worth noting that no fibre can be truly "single mode" because all "single mode" fibres support two orthogonal polarisation modes.

1.5 Dispersion

Dispersion is the effect which causes propagating light pulses to spread, and arises from the frequency dependence of the refractive index of dielectric materials. It is sometimes called "chromatic dispersion" in order to distinguish it from polarisation mode dispersion or intermodal dispersion. In this thesis "dispersion" refers to chromatic dispersion unless otherwise stated.

Dispersion is of great importance for most optical fibre systems, and crucial to nonlinear optics using ultra-short pulses. Ultra-short pulses consist of a broad spectrum of frequencies, and in a dispersive medium these all experience a different refractive index, so in general the pulse lengthens in time. The peak power of the pulse and therefore the nonlinearity is reduced in magnitude. Also, the sign and magnitude of the dispersion affects which nonlinear mechanisms may dominate. The work in this thesis is concerned with the careful engineering of fibre dispersion in order to control nonlinear effects, and this is discussed in more detail in chapter 2.

The transmission window of fused silica spans from 200 nm to 3000 nm. At the short wavelength end transmission is limited by electronic resonances, and at the long wavelength end loss occurs due to vibrational resonances [12]. The refractive index varies with frequency over this transmission window, giving rise to dispersion. The index variation for fused silica is plotted in figure 1-8, calculated using the Sellmeier equation [12]. The refractive index

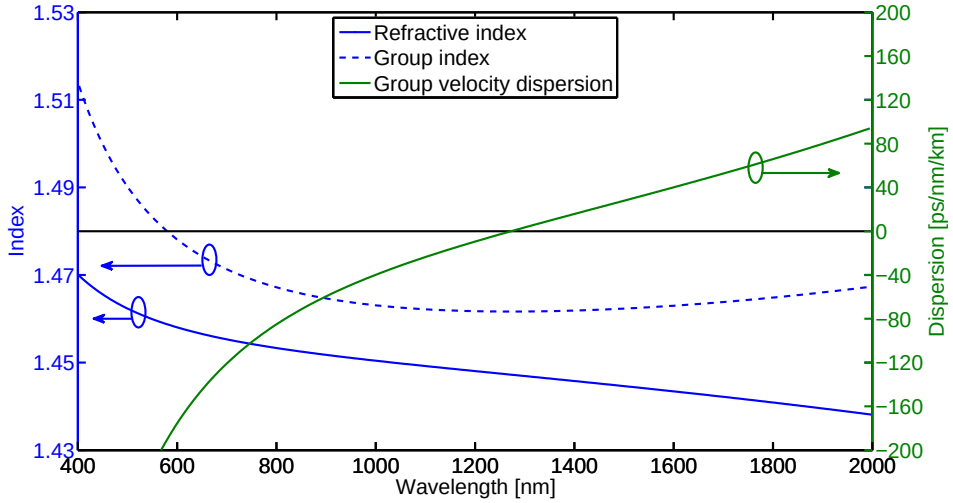

Figure 1-8: Wavelength dependence of the refractive index, the group index and the group velocity dispersion of bulk fused silica

corresponds to a phase velocity, given by

$$v_p = \frac{c}{n} = \frac{\lambda}{T} = \frac{\omega}{\beta} \tag{1.2}$$

where c is the speed of light in a vacuum, n is the refractive index, λ is the wavelength, T is the wave period, ω is the angular frequency and β is the propagation constant. Physically, the phase velocity is the speed of the phase front of a wave at a single frequency. As phase velocity is frequency dependent, the modulation envelope propagates with a different speed, the group velocity given by

$$v_g = \frac{d\omega}{d\beta} \tag{1.3}$$

The group velocity corresponds to a group index, given by [27]

$$n_g = \frac{c}{v_g} = n + \omega\frac{dn}{d\omega} \tag{1.4}$$

which is also plotted in figure 1-8. The group velocity is also frequency dependent, and this gives rise to "group velocity dispersion" (GVD), given by

$$\text{GVD} = \frac{d^2\beta}{d\omega^2} \tag{1.5}$$

GVD is usually given in units of s^2/m. To more fully describe GVD in fibres, the propagation constant β is expanded in a Taylor series about the pulse central angular frequency ω_0, as

$$\beta = \beta_0 + \beta_1(\omega - \omega_0) + \beta_2 \frac{1}{2}(\omega - \omega_0)^2 + ... \tag{1.6}$$

where β_n is the nth order derivative of β with respect to ω, at ω_0. It therefore follows that β_0 is β/ω_0, which is $1/v_p$, β_1 is equal to $1/v_g$, and β_2 is GVD. The higher order β coefficients represent the higher order dispersion, with β_3 describing the dispersion slope, and so on. Higher order dispersion is significant in experiments using extremely short pulses, or when pumping close to the zero dispersion wavelength (ZDW).

Dispersion can also be described using the "Dispersion parameter" D which is commonly expressed in convenient engineering unit ps/nm/km. It describes how a pulse with a given bandwidth (in nm) will have spread in time (in ps) after it has propagated along a certain length (in km) of fibre, and is given by [12].

$$D = \frac{d\beta_1}{d\lambda} = -\frac{2\pi c}{\lambda^2}\beta_2 = -\frac{\lambda}{c}\frac{d^2 n}{d\lambda^2} \tag{1.7}$$

The D parameter for fused silica is plotted in figure 1-8. As β_2 and D are opposite signs, "positive dispersion" and "negative dispersion" can mean different things depending on which parameter is used. A useful convention is to call dispersion "anomalous" when D is positive, and "normal" when D is negative, and this is the terminology used throughout this thesis. In the normal dispersion regime, higher frequencies have a lower group velocity than lower frequencies, and in the anomalous dispersion regime, the opposite is true.

When a pulse undergoes dispersion it becomes "chirped", meaning that it has a time dependent instantaneous frequency. The minimum pulse duration occurs when a pulse has no chirp, and it is transform limited. The transform limited pulse temporal profile is given by the Fourier transform of the pulse spectrum, with a flat spectral phase. The time-bandwidth product can be used to find out if a pulse is transform limited, or chirped. It is the product of the pulse temporal full-width half-maximum (FWHM), and the spectral bandwidth (in frequency). The time bandwidth-product for a transform limited Gaussian pulse is 0.441, and for a sech^2 pulse it is 0.315 [28].

1.5.1 Dispersion length

The dispersion length L_D defines a length scale over which dispersion is important for pulse evolution. It is approximately the propagation length required for a transform limited pulse to double in duration due to dispersion. It is given by

$$L_D = \frac{T_0^2}{|\beta_2|} \tag{1.8}$$

where T_0 is the half width at 1/e intensity point of the pulse. This is related to the FWHM of a Gaussian pulse by [12]

$$T_{\text{FWHM}} = 2(\ln(2))^{1/2} T_0 = 1.665 T_0 \tag{1.9}$$

For sech^2 pulse profiles, the 1.665 in the equation is replaced with 1.763.

1.5.2 Engineering photonic crystal fibre dispersion

This section describes the possibilities of dispersion engineering in PCFs. Optical fibres do not have the same dispersion as the bulk material from which they are made, because there is a contribution to their dispersion which depends on the geometry of the waveguide. Step index fibres have relatively small core-cladding index contrast (around 1%), so the mode is not tightly confined to the core. Therefore the waveguide contribution to dispersion is weak, and the dispersion profile is close to the bulk material dispersion. It is possible to shift the ZDW slightly by changing the core size or the doping level [29]. In PCF, the scope for dispersion engineering is far greater. The core cladding index contrast can be made much higher in PCF, so modes are much more strongly confined to the core. In this case waveguide dispersion becomes significant, and by changing the geometry of the core and cladding, dispersion can be modified drastically. For example, the ZDW can be shifted to visible wavelengths [30], and the dispersion can be flattened over a long wavelength range [31]. The work presented in chapters 3-6 of this thesis concern PCF which have all-normal dispersion profiles. This special dispersion profile is of vital importance for creating low-noise supercontinuum sources.

Waveguide dispersion arises because the modal index depends on core radius. Light at wavelengths shorter than the core radius is mostly confined to the core, and the modal index is therefore close to the core material index. For light with wavelengths longer than the core radius, the mode expands and overlaps more with the cladding. The modal index is therefore closer to the cladding index. Overall the modal index decreases with increasing wavelength. This can be seen in figure 1-9 (a), which shows how the modal index changes with wavelength for a strand of dielectric suspended in air with a fixed constant material index of 1.5. The dispersion corresponding to this index change is plotted in figure 1-9 (b). Waveguide dispersion is anomalous at short wavelengths, and normal at long wavelengths, which is the opposite of material dispersion.

The waveguide dispersion of PCF can be controlled by adjusting the pitch Λ and/or hole diameter d of the cladding. PCF with extremely high air filling fractions can be approximated as a strand of silica surrounded by air. For PCFs with smaller air filling fractions (0.8 or less) the air holes must be taken into account. Some examples of dispersion curves possible in PCF for different cladding dimensions are plotted in figure 1-10. These were calculated using the empirical formula in [32]. For a constant Λ, increasing d/Λ produces a "more anomalous" dispersion profile. For a constant value of d/Λ, increasing Λ makes the dispersion more anomalous, and also shifts the zero dispersion, or the minimum dispersion, to longer wavelengths.

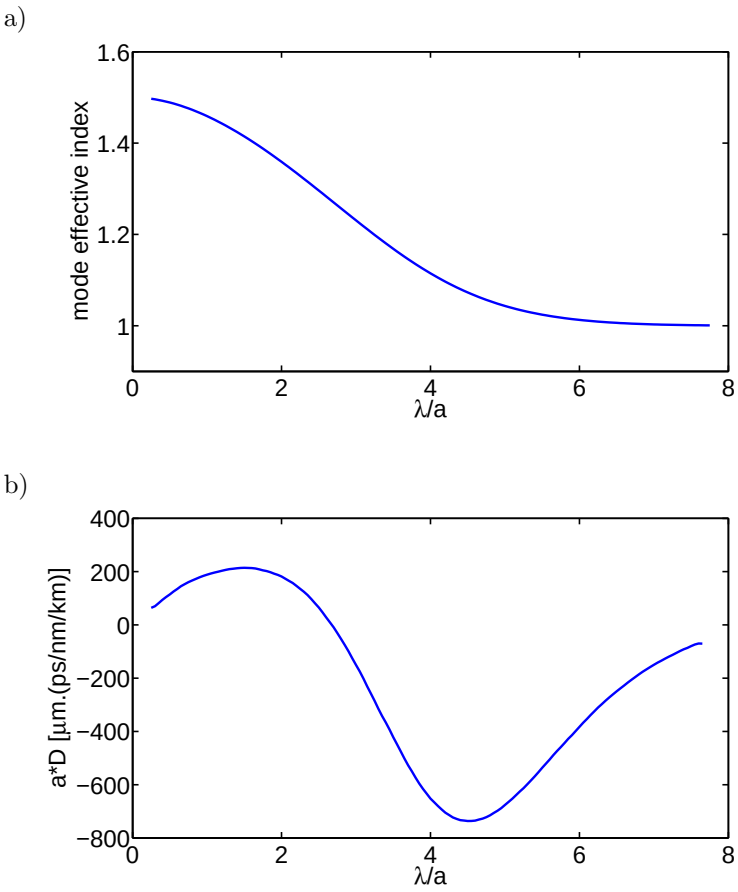

Figure 1-9: a) Modelled modal index variation in strand of material with constant refractive index = 1.5, suspended in air. The model is based on equations in [24]. The wavelength is normalised to the strand radius a. b) Dispersion resulting from modal index change in (a). D is scaled with strand radius a. Based on Fig. 5.3 in [27]

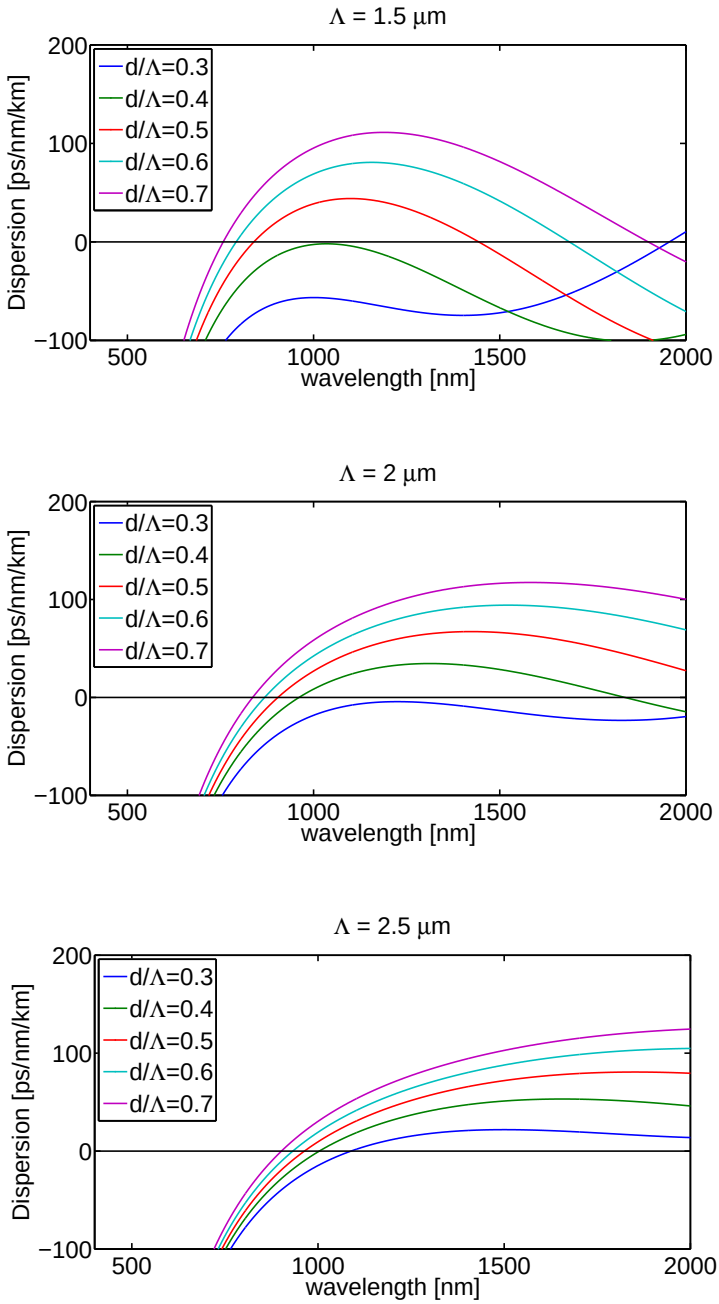

Figure 1-10: Disperison calculated using empirical formula in [32] for photonic crystal fibres with various Λ and d/Λ, to show how changing cladding parameters affects fibre dispersion

1.5.3 Measuring dispersion

To measure the GVD of an optical fibre, various techniques can be employed [33]. In this thesis the method used is white light interferometry. The measurement set-up is shown in figure 1-11. Pulses from a broadband supercontinuum source are split using a non-polarising beam-splitter into two arms of an interferometer. One arm of the interferometer contains the fibre being tested, and the other arm is a free space arm whose length can be changed by moving the motorised mirror stage. The beams are recombined in a second beam-splitter and delivered to a photo-receiver via a narrow band-pass filter to select the wavelength of interest. The free space arm contains two objectives to compensate for the dispersion of the input and output coupling objectives in the fibre arm. The fibre arm contains a chopper, which modulates the signal, allowing the lock-in amplifier to pick up the signal if it is weak.

The length of the free space arm is slowly changed, and when the pulses from each arm are overlapped at the detector interference fringes can be seen. An example of a typical interference pattern is plotted in figure 1-12. The intensity of the fringe envelope depends on the time delay; zero delay is when the visibility of the fringe is highest. The position of the motorised mirror stage, x, at which maximum fringe intensity can be observed, is recorded at each wavelength step. The value of x need not be absolute, because only the variation of the mirror positions with wavelength is needed to calculate dispersion. The difference in x with wavelength is equal to half the difference in optical path length with wavelength induced by the fibre. As the optical path length inside the fibre is $n_g l$ where n_g is the group index and l is the fibre length, then

$$\frac{dx}{d\lambda} = \frac{l}{2}\frac{dn_g}{d\lambda} \tag{1.10}$$

Taking equation 1.7 and $\beta_1 = 1/v_g = n_g/c$ then

$$D = \frac{d\beta_1}{d\lambda} = \frac{1}{c}\frac{dn_g}{d\lambda} \tag{1.11}$$

and combining equations 1.10 and 1.11 yields the expression

$$D = \frac{2}{lc}\frac{dx}{d\lambda} \tag{1.12}$$

For D in units of ps/nm/km, l is the fibre length in km, c is the speed of light in vacuum in mm/ps, x is in mm and wavelength λ is in nm.

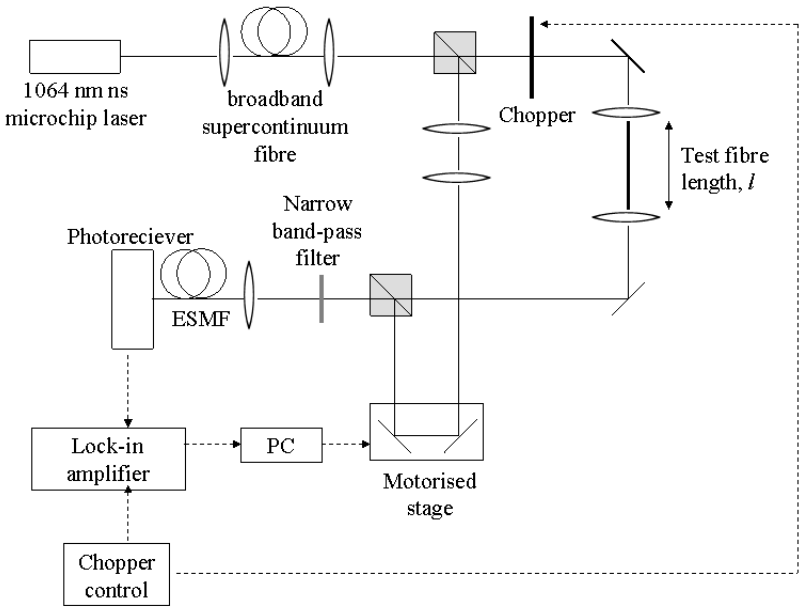

Figure 1-11: Experimental set-up for measuring fibre dispersion using white light interferometry. ESMF, endlessly single-mode fibre

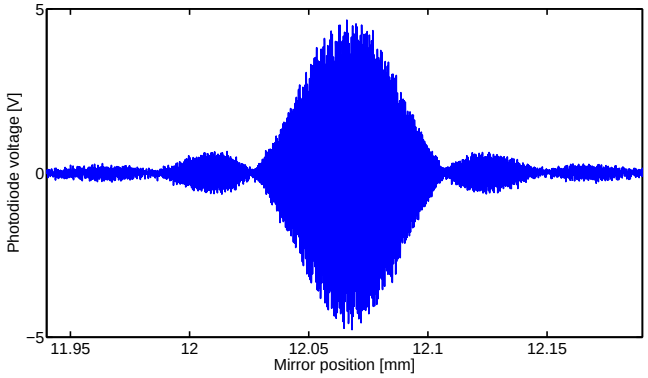

Figure 1-12: An example of interference fringes obtained during a dispersion measurement using white light interferometry. The mirror position at the maximum interference intensity is x in equation 1.12

1.6 Loss

The attenuation of light in silica optical fibres can occur via several effects, including Rayleigh scattering, material absorption, and scattering or absorption by impurities such as OH [34]. Loss can also occur due to insufficient confinement of light to the core, known as confinement loss, or by bending of the fibre, known as bend loss.

Confinement loss is a result of the finite extent of the photonic crystal cladding. The propagating mode has high intensity in the core region, which decays with radius. Therefore, a small amount of light extends into the cladding. If a significant part of the mode extends past the cladding, into the high index jacket then this light will no longer be confined and will be lost.

Figure 1-13 shows the variation in confinement loss for a typical PCF, with different numbers of rings of air holes, and different air-hole sizes. These were calculated using a multi-pole mode solver software "CUDOS MOF" [35, 36]. The software computes the complex effective refractive index of the mode at different wavelengths. Confinement loss in dB/m was calculated using [37]

$$\text{Confinement loss} = \frac{20}{\ln(10)} \frac{2\pi}{\lambda} \text{Im}(n_{\text{eff}}) \tag{1.13}$$

It can be seen from figure 1-13 that confinement loss increases for longer wavelengths, because the mode extends further into the cladding for longer wavelengths. Confinement loss is reduced by an increased number of air-hole rings in the cladding. The higher the number of rings, the less the mode extends past the cladding region. The confinement loss is also reduced for larger air holes, because a higher index contrast confines light more tightly in the core.

Bend loss occurs when a fibre is bent beyond a critical bend radius. At the fibre bend, part of the mode which is propagating in the cladding on the outside of the bend must travel faster than the light in the core in order to maintain a wavefront perpendicular to the direction of propagation. At a critical bend radius, the outside edge of the mode has to travel faster than the speed of light in the material to maintain the wavefront. As this is impossible, energy is lost through radiation [14]. The critical bend radius is larger for large mode area fibres, and it also increases for longer wavelengths, resulting in a long wavelength "bend edge", past which all light is lost [38].

Bend loss can be used to create single mode propagation in a multimode fibre. The critical bend radius for higher order modes is usually larger than for the fundamental mode, so by simply bending the fibre the higher order modes can be removed without disturbing the fundamental mode, provided there is no coupling between modes.

a)

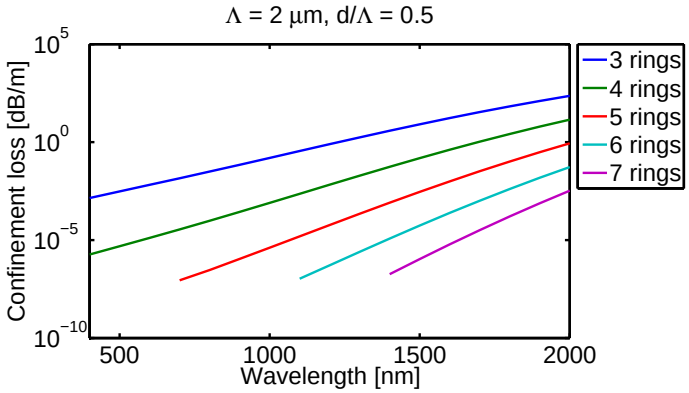

b)

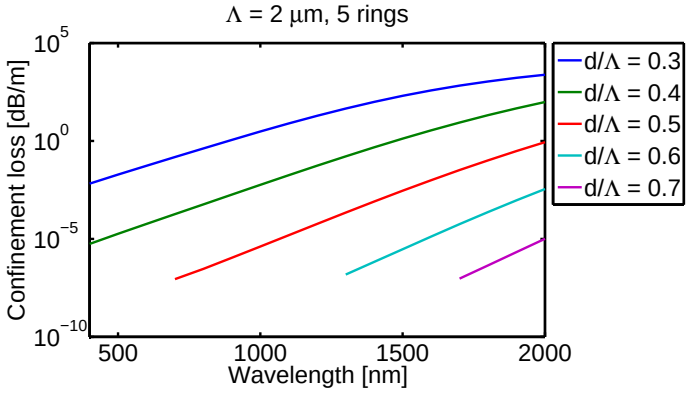

Figure 1-13: Confinement loss modelled using CUDOS for a) photonic crystal fibre with $\Lambda = 2$ μm and $d/\Lambda = 0.5$, with different numbers of air-hole rings surrounding the core, and b) photonic crystal fibre with $\Lambda = 2$ μm and 5 air-hole rings, with different values of d/Λ

1.7 Band gap guidance in hollow-core photonic crystal fibre

PCFs can guide light in a hollow core. The mechanism for guidance in this case cannot be total internal reflection, as there are no solid materials with a lower refractive index than air from which to form a cladding. Instead hollow core fibres can guide light because of the photonic band gap effect. A photonic band gap is a range of modal indices which are not supported by a photonic crystal. Therefore, modes which have indices within this range can be confined to the fibre core.

A way to understand the photonic band gap is the antiresonant reflecting waveguide (ARROW) model [39]. This is a simple physical model which considers the high index inclusions in the cladding as step-index waveguides which can support modes. In the band gap fibre shown in figure 1-2 (d) the high index inclusions are rods of doped silica with a higher index than the silica surround. In the hollow-core fibre shown in 1-2 (c), the high index inclusions are at the intersections in the web of the cladding structure. The high index inclusions are said to be "resonant" at their modal cut-off wavelengths, and this is where minima in fibre transmission occur. At other wavelengths the high index inclusions are "anti-resonant" and light is confined to the low index core of the fibre. An interesting aspect of this model is that the location and separation of the high index inclusions do not affect the photonic band gap; only the shape, size and index of the inclusions are important. Guidance of light in a hollow core is useful because air has very low dispersion and nonlinearity, so hollow core PCF can be used to deliver pulses with little distortion. Hollow core fibres also have anomalous GVD across most of the transmission band, so they can be used for soliton propagation, a nonlinear phenomenon which is described in chapter 2. A disadvantage of hollow core PCF is the transmission bandwidth is typically 200 or 300 nm, so they are unable to deliver broadband signals.

1.8 Fibre birefringence

Single mode fibres are not strictly single mode because they can support two orthogonal polarisation modes. In a fibre with perfect circular symmetry, these modes are degenerate and no coupling occurs between them. In this case the polarisation state at the fibre input is maintained at the output. In real life all fibres have some unintentional asymmetry as a result of the fabrication method, and so each polarisation mode has a different value of propagation constant β [12]. This is known as linear modal birefringence, so called to distinguish it from nonlinear birefringence which is power-dependent. The difference between the two modal propagation constants fluctuate randomly along the length of the fibre due to small fluctuations introduced during fabrication, impurities or stresses such as bending. The result of this is that linearly polarised light at the fibre input will have a mixed polarisation at the output. Because the polarisation modes have different propagation constants the pulse spreads in time, and this is known as polarisation mode dispersion (PMD).

To understand this phenomenon, it is useful to consider a length of fibre with constant

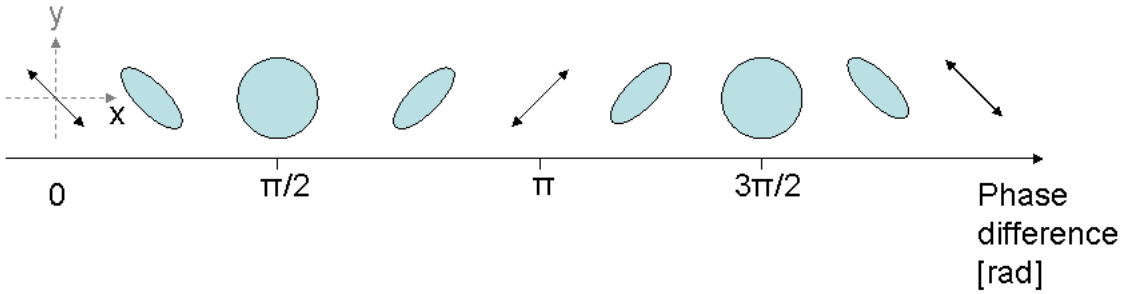

Figure 1-14: Evolution of polarisation state over one beat length when linearly polarised light is launched into a birefringent fibre at 45° to the slow and fast axes

birefringence. A commonly used parameter describing linear birefringence is the difference in the modal index of the two orthogonal polarisation modes, given by

$$B_F = n_x - n_y = \frac{(\beta_x - \beta_y)}{2\pi/\lambda} \tag{1.14}$$

where λ is the wavelength of light, n_x and n_y are the indices of the slow and fast modes respectively, and similarly β_x and β_y are the propagation constants for the slow and fast modes [14]. Linear birefringence can vary between 10^{-6} for very low birefringence fibres [12], and 10^{-3} for highly birefringent fibres [40].

If linearly polarised light is launched at an angle to one of the polarisation axes, then both polarisation modes will be excited. The difference in propagation constant means that there is a constantly changing phase difference between the light in the two modes. This results in beating of the polarisation, over a fibre length equal to the beat length L_B, given by

$$L_B = \frac{2\pi}{(\beta_x - \beta_y)} = \lambda/B_F \tag{1.15}$$

For a linearly polarised input at 45° to the slow and fast axes, the polarisation changes over the beat length as shown in figure 1-14. The light is initially linearly polarised, and becomes elliptically polarised. At $\pi/2$ phase difference the light is circularly polarised. At π phase difference, the light is linearly polarised again but at 90° to the input. The polarisation then goes through elliptical to circular at $3\pi/2$ and back to its original state when there is 2π phase difference. Beat lengths in fibres can vary between metres for low birefringence fibres and millimetres for highly birefringent fibres.

If linearly polarised light is launched into either the slow or fast axis of a fibre with low birefringence, and neglecting the random fluctuations in the fibre, the polarisation will be maintained. In reality, random fluctuations in the fibre perturb the field in the fibre, causing some light to be coupled into the other polarisation axis, resulting in PMD. To reduce PMD, fibres can be made highly birefringent, and these are known as polarisation maintaining fibres.

The circular symmetry of the core or cladding is purposefully broken in order to create a large difference in modal indices between the two polarisation states. In this case the difference in β between the polarisation modes is so large that small fluctuations in β due to perturbations are insignificant. Conventional fibres can be made birefringent by adding glass rods to the cladding with a different thermal expansion coefficient, or making the core elliptical. In PCF high birefringence can be achieved by creating a pattern of holes in the cladding with rotational symmetry of order two. An example of highly birefringent PCF is shown in figure 1-2. The degree of birefringence achievable in PCF can be around 10 times larger than in conventional fibres [40].

Chapter 2

Nonlinear optics and supercontinuum generation

2.1 Introduction

The previous chapter discussed linear optical fibre properties such as dispersion and loss. These effects originate from the motion of bound electrons in the material which is proportional to the applied field. However, this is only true for the propagation of low intensity light. When using high intensity light sources such as ultra-short laser pulses, the material can respond in a nonlinear way such that the electron displacement is no longer proportional to the optical field. This is nonlinear optics, and in general gives rise to the generation of new frequencies.

This chapter contains an overview of nonlinear optics, concentrating on the nonlinear optical effects involved in supercontinuum generation. Supercontinuum generation is generally a combination of many nonlinear effects occurring simultaneously. The dynamics of supercontinuum generation under different pumping conditions are described and related to the spectral coherence properties, which is of key importance for this work. Finally, a numerical code based on the generalised nonlinear Schrödinger equation which was used for simulations presented later in the thesis, is described.

Much of the nonlinear optical theory described in this chapter can be found in references [12] and [41].

2.2 Nonlinear optics

In the linear optical regime, the induced polarisation in a dielectric material is given by

$$\mathbf{P} = \varepsilon_0 \chi \mathbf{E} \tag{2.1}$$

where ε_0 is the permittivity of free space, χ is the susceptibility and $\mathbf{E}$ is the electric field. For high intensity fields the nonlinear response of the material needs to be taken into account by

expanding the induced polarisation to include higher order terms [12]

$$\mathbf{P} = \varepsilon_{\mathbf{0}}(\chi^{(\mathbf{1})}.\mathbf{E} + \chi^{(\mathbf{2})}.\mathbf{EE} + \chi^{(\mathbf{3})}.\mathbf{EEE} + \dots) \tag{2.2}$$

where $\chi^{(n)}$ is the nth order susceptibility. $\chi^{(1)}$ is the linear susceptibility, which is related to linear optical effects like absorption and linear refractive index. $\chi^{(2)}$ is the 2nd order susceptibility which relates to nonlinear effects including second harmonic generation. However, $\chi^{(2)} = 0$ for materials which have inversion symmetry at a molecular level, which includes silica glass. Therefore, most nonlinear effects in silica fibres originate from the 3rd order susceptibility, $\chi^{(3)}$. These include Kerr nonlinearity, and Raman scattering.

2.2.1 Kerr nonlinearity

Kerr nonlinearity is the intensity dependence of refractive index. It is directly related to the $\chi^{(3)}$ term in the induced polarisation. Given that $\chi^{(2)} = 0$ in optical fibres, the induced polarisation can be re-written as

$$\mathbf{P} = \varepsilon_{\mathbf{0}}(\chi^{(\mathbf{1})}.\mathbf{E} + \chi^{(\mathbf{3})}.\mathbf{EEE}) \tag{2.3}$$

and from Maxwell's equations, the electric flux density is given by

$$\mathbf{D} = \varepsilon_{\mathbf{0}}\mathbf{E} + \mathbf{P} = \varepsilon_{\mathbf{0}}\mathbf{n^2}\mathbf{E} \tag{2.4}$$

By substituting equation 2.3 into equation 2.4 it can be shown that the refractive index has an intensity dependent contribution. The total refractive index is given by [12]

$$n = n_0 + |E|^2 n_2 \tag{2.5}$$

where $n_0 = \sqrt{(1 + \chi^{(1)})}$ is the linear contribution to refractive index and n_2 is the nonlinear contribution, given by [12]

$$n_2 = \frac{3}{8n}\chi^{(3)} \tag{2.6}$$

Kerr nonlinearity gives rise to many nonlinear effects, including self phase modulation, cross phase modulation, self-steepening, modulation instability and four wave mixing.

2.2.2 Nonlinear length

The nonlinear length is the propagation length after which nonlinear effects become significant (the phase shift due to nonlinearity is equal to 1 radian). It is given by

$$L_{\mathrm{NL}} = \frac{1}{\gamma P_0} \tag{2.7}$$

where P_0 is the pulse peak power, and γ is the nonlinear coefficient, which can be calculated using

$$\gamma = \frac{n_2^I \omega_0}{c A_{\text{eff}}} \tag{2.8}$$

Here ω_0 is the central frequency, c is the speed of light, and n_2^I is the nonlinear index coefficient defined, for convenience, with respect to the intensity I as $n = n_0 + I n_2^I$. A typical value of n_2^I for silica glass is $3.2 \times 10^{-20}\ m^2 W^{-1}$ [12]. A_{eff} is the effective area of the mode, which is given by

$$A_{\text{eff}} = \frac{(\int\int_{-\infty}^{\infty} |E(x,y)|^2\, dxdy)^2}{\int\int_{-\infty}^{\infty} |E(x,y)|^4\, dxdy} \tag{2.9}$$

where $E(x, y)$ is the mode field profile.

2.2.3 Four wave mixing

Four wave mixing (FWM) is a process in which four optical waves interact non-linearly inside a dielectric medium. Each wave passing through the medium sets up a modulation of the refractive index of the material. If two waves with different frequencies ω_1 and ω_2 are propagating together in the medium, then the modulation of the refractive index has terms at two new frequency components given by $\omega_3 = 2\omega_1 - \omega_2$ and $\omega_4 = 2\omega_2 - \omega_1$. This process is non-degenerate FWM. The higher frequency component is known as the signal, and the low frequency component the idler. Light at the new frequencies is generated provided there is sufficient phase matching. This means that the generated waves must be matched in phase in order for effective accumulation of newly generated frequencies to take place. The phase mismatch, given by $\Delta\kappa = \beta_3 + \beta_4 - \beta_1 - \beta_2$ should be as close as possible to zero.

Degenerate FWM can also occur for the case $\omega_1 = \omega_2$. In this case two pump photons are annihilated to produce a signal photon and an idler photon. These new frequency components are seeded from noise and their positions depend on the phase matching conditions.

FWM is the mechanism underlying many nonlinear effects including self phase modulation, cross phase modulation, and modulation instability.

2.2.4 Self phase modulation

Self phase modulation (SPM) is the self induced phase shift of a pulse due to Kerr nonlinearity. Because the refractive index is intensity dependent, it induces an intensity dependent phase shift, given by

$$\phi(z,t) = nk_0 z = (n + n_2|E(z,t)|^2)k_0 z \tag{2.10}$$

where z is the effective propagation length and $k_0 = 2\pi/\lambda_0$ where λ_0 is the central wavelength of the pulse. The nonlinear phase shift due to the Kerr effect is therefore

$$\phi_{NL}(z,t) = n_2 k_0 z |E(z,t)|^2 \tag{2.11}$$

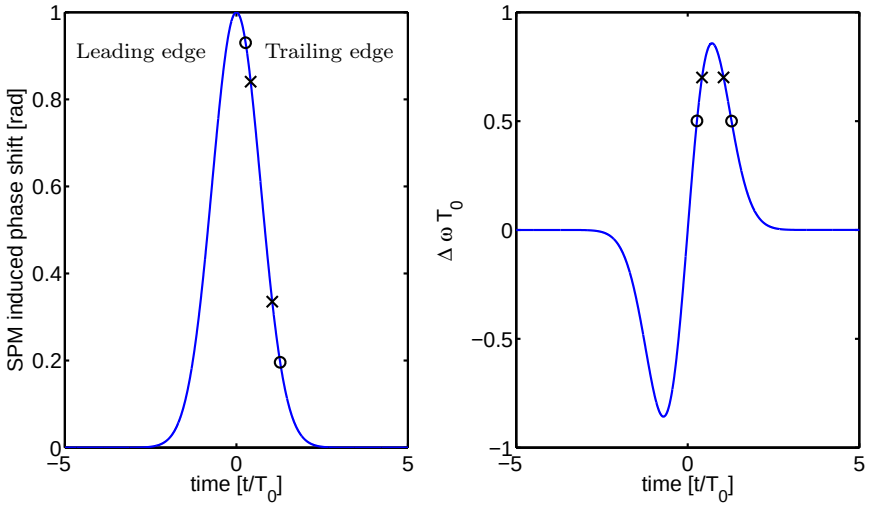

Figure 2-1: Time dependent self phase modulation induced a) nonlinear phase shift and b) frequency shift for a Gaussian pulse. Points marked with circles show temporal positions within the pulse with the same frequency shift, but different phase shift. Light at these positions interfere and produce the modulations on the spectrum

The nonlinear phase shift is time dependent, because the intensity profile of the pulse is time dependent. This time dependent phase shift corresponds to a frequency shift, given by [12]

$$\delta\omega(t) = -\frac{\delta\phi_{NL}}{\delta t} \tag{2.12}$$

The phase shift and frequency shift for a Gaussian pulse due to SPM are plotted in figure 2-1. The maximum phase shift is set equal to 1, and the time scale is normalised to pulse duration T_0. The leading edge of the pulse experiences a negative frequency shift, and so longer wavelengths are generated. At the trailing edge of the pulse, the opposite is true and shorter wavelengths are generated. At the point of maximum intensity, and in the pulse tails the frequency shift is zero, so here the central frequency of the pump is maintained. In the absence of dispersion, the temporal pulse profile is not modified, but the spectrum broadens. Figure 2-2 shows the spectrum generated after different amounts of nonlinear phase shift, in the absence of dispersion. The spectrum broadens symmetrically in frequency around the pump, and has distinctive modulations in the spectral intensity.

The modulations in the spectrum are a result of interference between light of the same frequency, originating from two different temporal positions within the pulse. In figure 2-1 (b) it can be seen that in general light at two different temporal positions within the pulse undergoes the same frequency shift. For example, the two points marked with circles in figure 2-1 (b) have the same frequency shift, and similarly for the two points marked with crosses. The equivalent temporal positions are marked similarly in 2-1 (a). In both cases there is a phase

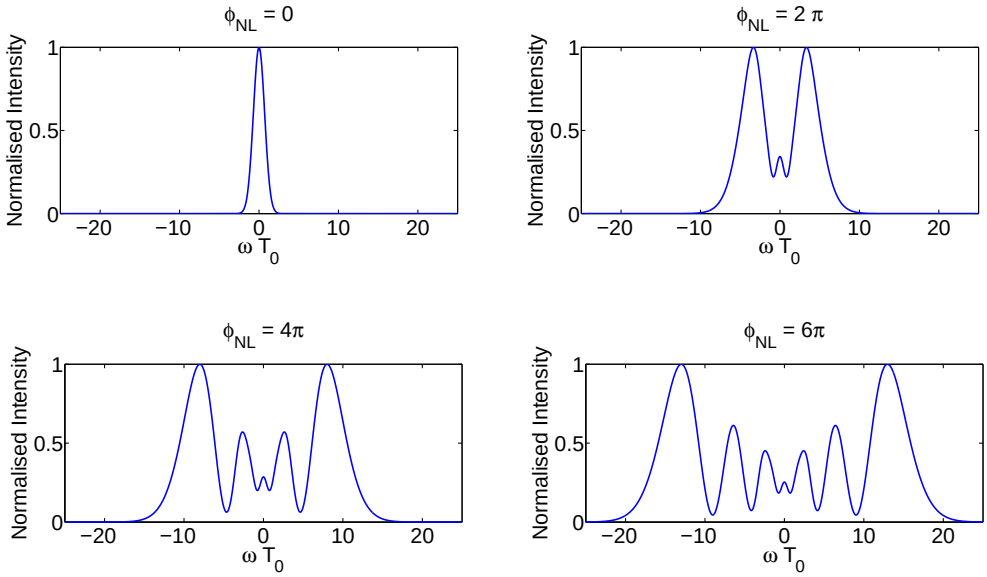

Figure 2-2: Calculated evolution of the self phase modulation spectrum generated by a Gaussian pulse in the absence of dispersion. The total nonlinear phase shift ϕ_{NL} is given above each spectrum, and the frequency is normalised with respect to the pulse duration. The number of modulation peaks in each spectrum is equal to $(\phi_{NL}/\pi) + 1$

difference between identical frequency components, which determines the spectral intensity at that frequency. A peak in the spectrum thus corresponds to a phase difference of $m2\pi$ between the identical frequency components where m is an integer.

2.2.5 Dispersion and self phase modulation

The previous section described SPM in the absence of dispersion. However, in reality dispersion usually has a significant role to play in pulse propagation. When SPM occurs in a dispersive medium, qualitatively different results are obtained depending on the sign of the GVD.

Anomalous dispersion

When a pulse undergoes SPM, low frequencies are generated at the leading edge, and high frequencies are generated at the trailing edge of the pulse. In the anomalous dispersion regime, the SPM induced chirp and dispersion act against one another. Newly generated frequencies move towards the pulse centre, so the pulse is compressed. In some cases the dispersion and nonlinearity exactly cancel one another and produce a pulse which travels without distortion, known as a fundamental soliton.

Solitons are exact solutions of the nonlinear Schrödinger equation, and take the form

$$E(z,t) = N\sqrt{\frac{|\beta_2|}{\gamma T_0^2}}\ \mathrm{sech}\left(\frac{T}{T_0}\right) \tag{2.13}$$

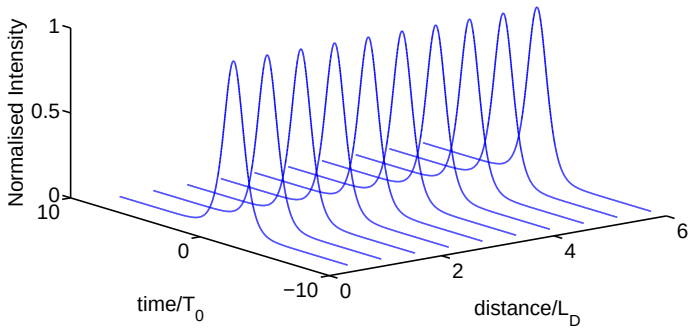

Figure 2-3: Propagation of a sech^2 pulse with initial conditions for an N=1 soliton, over 6 dispersion lengths and anomalous dispersion ($\beta_2 < 0$). It propagates without any change of its temporal profile.

where N is the soliton order, β_2 is the GVD, T is the time at a frame of reference moving with the pulse, and T_0 is the pulse duration. The soliton order is given by $N^2 = L_D/L_{NL}$ [41] where L_D and L_{NL} are the characteristic dispersive and nonlinear length scales given in equations 1.8 and 2.7.

A fundamental soliton has soliton order $N = 1$, ie. the dispersion length and nonlinear length are equal. A fundamental soliton propagates without any change to its temporal or spectral profile, as can be seen in figure 2-3. The pulse profiles were calculated using the generalised nonlinear Schrödinger equation solver code which is described later in section 2.4. Only Kerr nonlinearity and a constant β_2 were included in the simulation.

Higher order solitons have $N > 1$, and in that case SPM and dispersion are not exactly balanced. Unlike fundamental solitons they do not maintain their temporal and spectral shape during propagation, and instead periodically split and re-combine over a distance known as the soliton period $z_0 = (\pi/2)L_D$. The temporal change with propagation of a soliton with $N = 3$ is plotted in figure 2-4. The intensity axis is normalised to the input intensity, so it is clear that for the case of a higher order soliton there is significant initial compression.

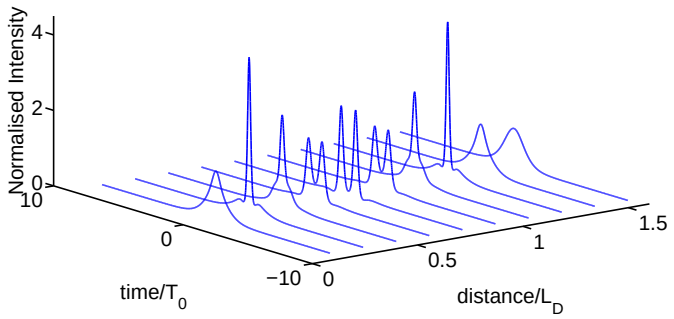

Figure 2-4: Propagation of a sech^2 pulse with initial conditions for an N=3 soliton, over 1 soliton period and with anomalous dispersion ($\beta_2 < 0$). The temporal profile changes periodically with propagation length.

Normal dispersion

Under normal GVD, the dispersion and SPM-induced chirp reinforce one another. The low frequencies generated at the leading edge of the pulse have a higher group velocity than the central frequency, and high frequencies generated at the trailing edge of the pulse have a lower group velocity. If viewing the pulse from a frame of reference moving with the pulse in time, the newly generated frequencies move away from the pulse centre. The pulse broadens rapidly with propagation, and this can be seen in figure 2-5.

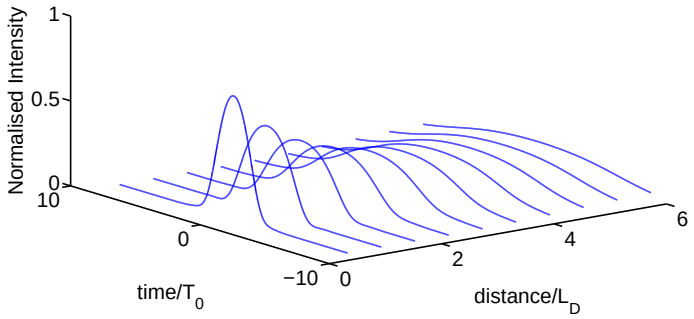

Figure 2-5: Propagation of a sech^2 pulse with initial conditions for an N=1 soliton, over 6 dispersion lengths and normal dispersion ($\beta_2 > 0$).

2.2.6 Cross phase modulation

Cross phase modulation (XPM) is the nonlinear modification of a light wave by another co-propagating light wave with a different frequency, or polarisation. Light is generated at initial frequencies ω_1 and ω_2, and at new frequencies $2\omega_1 - \omega_2$ and $2\omega_2 - \omega_1$. The new frequency terms are only generated efficiently if there is phase matching. This is a non-degenerate four wave mixing process.

2.2.7 Modulation instability

Modulation instability (MI) is the nonlinear amplification of fluctuations on the envelope of continuous wave (CW) or pulsed light. It results in the break up of the optical envelope into a series of ultra-short pulses, and the generation of frequency side bands. The main requirement is anomalous dispersion. When a perturbation causes a small increase in intensity at one temporal position, this part of the field undergoes SPM and then compression due to the anomalous dispersion. The peak intensity thus increases, and the process continues to happen.

The frequency shift at maximum MI gain is given by [12]

$$\Omega_{\max} = \pm\left(\frac{2\gamma P_0}{|\beta_2|}\right)^{1/2} \tag{2.14}$$

and the maximum MI gain is given by $g_{\max} = 2\gamma P_0$.

2.2.8 Self Steepening

Self steepening occurs due to the intensity dependence of the group index. The pulse peak has higher group index than the rest of the pulse, and so propagates with a lower velocity than the rest of the pulse. The result is that the intensity gradient of the leading edge is reduced, and the intensity gradient of the trailing edge is increased. If self steepening is significant, then

spectral broadening via SPM will occur asymmetrically, with increased spectral broadening on the short wavelength side of the spectrum, and higher spectral intensity on the long wavelength side to conserve energy in the FWM process [12]. Self steepening is more significant for shorter pulses.

2.2.9 Raman scattering

The nonlinear optical effects described up until this point are elastic processes involving the induced motion of electrons, in which no energy is transferred to or from the material. Raman scattering is an inelastic process, where energy is transferred to or from the material, as a result of molecular vibrational or rotational motion. If a pump photon with energy $\hbar\omega_{\mathrm{p}}$ excites a vibrational state of a molecule of the propagation medium, a Stokes photon is scattered with lower energy $\hbar\omega_{\mathrm{s}}$. An anti-Stokes photon with higher energy $\hbar\omega_{\mathrm{as}}$ can also be emitted if the molecule is already in an excited vibrational state when the photon arrives, however this is less likely because there are fewer molecules already in an excited state. This effect can therefore be used in spectroscopy to probe specific vibrational resonances of a material [42, 43]. In silica glass Raman scattering can occur over a broad range of frequency shifts, because the amorphous nature of the material means the molecular vibrational frequencies form a continuum.

Raman scattering can occur spontaneously, however this is a relatively weak effect. Stimulated Raman scattering is a nonlinear inelastic process in which highly efficient Raman scattering can occur under the influence of high intensity laser beam. Stimulated Raman scattering can occur within solitons whose bandwidth exceeds the Raman gain bandwidth in silica. The low frequency components experience amplification at the expense of the high frequencies, and the overall effect is that the pulse shifts to longer wavelengths. This is also known as soliton self frequency shift (SSFS) [44].

2.2.10 Soliton fission

Higher order solitons are sensitive to perturbations due to Raman scattering, higher order dispersion or MI. Under the influence of these perturbations, instead of following the periodic propagation described in section 2.2.5, higher order solitons decay into a series of fundamental solitons. This process is known as soliton fission. The break-up always occurs at the point of maximum compression, giving rise to a fission length L_{fiss} given by L_D/N. A higher order soliton of order N will emit N fundamental solitons, which are emitted in decreasing order of peak intensity. They can then undergo SSFS, forming a continuum of solitons Raman shifted to different wavelengths, and due to dispersion, different temporal positions. If a soliton is propagating close to the ZDW, then some energy can be transferred into the normal dispersion regime. This is known as a dispersive wave, and its generation requires phase matching with the Raman shifted solitons. The overall result is a broadband continuum, so this is a mechanism by which supercontinua can be generated.

2.3 Supercontinuum generation

Supercontinuum generation is the significant spectral broadening of a pump pulse due to nonlinear optical effects, to produce a spectrally continuous output. Supercontinuum generation is a growing technology; a search on Web of Knowledge for papers with the word "supercontinuum" in the title results in 169 papers published up until the year 1999. Since the year 2000 to the time of writing, there have been 2755 papers published. Supercontinuum generation was first observed in bulk BK7 glass in the 1970s [45, 46]. Supercontinua were also generated in conventional fibres [47, 48], with improved efficiency and spatial properties compared to bulk.

The advent of PCF greatly improved supercontinuum technology. One reason for this was the ability to engineer the dispersion, moving the ZDW to shorter wavelengths [49]. This allowed the broadest spectra to be obtained by pumping in the anomalous dispersion regime, using commonplace Ti:Sapphire lasers centred around 800 nm. Another advantage was the ability of PCF to tightly confine light to the core, increasing nonlinearity, and thus efficiency. In general the aim for research into supercontinuum generation has been to enhance bandwidth. In the year 2000 the first octave spanning supercontinuum was generated in PCF using nanojoule pulses from a Ti:Sapphire laser [30]. Previously, supercontinuum generated in bulk required microjoule sources to obtain comparative spectral broadening. Pulses longer than femtoseconds can also be used to generate supercontinuum in PCF; from picosecond [50] and nanosecond pulses [51], to high power CW lasers [52]. Single mode guidance properties of PCF are also useful, as this allows the output to be focused into a diffraction-limited spot. Comparable supercontinuum spectra can also be observed in a tapered solid fibre [53]. PCFs are therefore not necessary to obtain broad supercontinua, however they are more mechanically stable, and easier to produce in large quantities than fibre tapers.

Supercontinua generated in PCF have found applications in spectroscopy [54–57], optical coherence tomography [58], pulse compression [59–64], tunable lasers [65, 66], and optical frequency metrology [67, 68].

In general, many nonlinear effects occur simultaneously to create a supercontinuum. These can include SPM, XPM, Raman scattering, MI, soliton fission, SSFS and dispersive wave generation. Depending on the combinations of input pulse duration and wavelength, and fibre dispersion and nonlinearity, different nonlinear effects can dominate the broadening. Dramatic differences in the spectral width, shape, and noise properties of the supercontinuum can be observed by changing these parameters. A brief overview is presented here, which focuses on the generation of supercontinua using femtosecond pulses. For a more extensive study of supercontinuum dynamics, the reader is directed to [69].

The most common way to generate broadband supercontinuum in PCF using femtosecond pump pulses is to select a PCF with a ZDW which falls just below the laser wavelength. Because the dispersion is anomalous at the pump wavelength, the supercontinuum is generated by soliton dynamics. The fission of a higher order soliton produces a series of fundamental solitons which are Raman shifted to longer wavelengths, and a dispersive wave is generated at short wavelengths. This mechanism can produce a broad supercontinuum spectrum. However,

soliton dynamics are extremely sensitive to pump pulse fluctuations. Small fluctuations in the pump amplitude or phase from shot to shot can cause significant fluctuations in spectral intensity and phase of the resulting supercontinuum. These fluctuations are averaged out over thousands of pulses when viewing the spectrum on a spectrometer, so the spectrum may appear smooth, but in reality there may be large deviations from this average in each pulse. The fluctuating spectral intensity and phase translates into loss of spectral coherence. The origin of the pump fluctuations is fundamental quantum fluctuations in the laser cavity, which cannot be eradicated. Larger fluctuations due to laser technical noise can also be an issue, but can be reduced by using a less noisy laser.

When pumping below the ZDW, solitons cannot form and spectral broadening can occur only via SPM and Raman scattering. This process is less efficient and will not produce a spectrum as broad as that produced by soliton dynamics. This is due to the rapid temporal spreading of pulses under SPM and normal dispersion. The advantage of generating supercontinuum in the normal dispersion regime is that the spectral broadening is not seeded from noise, and does not amplify pump fluctuations. If some of the light generated reaches into the anomalous dispersion regime, then these frequency components will by affected by soliton dynamics. The aim of this research was to reduce supercontinuum fluctuations, by generating supercontinuum in a PCF with an all-normal dispersion profile, thus eliminating soliton effects. This is explained in more detail in chapter 3.

2.4 Modelling supercontinuum generation

This thesis contains some results of numerical modelling of nonlinear pulse propagation, carried out using a code written by John Dudley. The code solves numerically the generalised nonlinear Schrödinger equation (GNLSE), which describes the evolution of an optical pulse envelope. The particular form of the GNLSE used in the modelling is taken from [70] and is given by

$$\frac{\partial A}{\partial z} + \frac{\alpha}{2}A - \sum_{k\geq 2}\frac{i^{k+1}}{k!}\beta_k\frac{\partial^k A}{\partial T^k} = i\gamma\left(1 + i\tau_{\text{shock}}\frac{\partial}{\partial T}\right)\left(A(z,t)\int_{-\infty}^{\infty}R(T')|A(z,T-T')|^2dT'\right) \tag{2.15}$$

where A is the field envelope and z is the propagation distance. The left hand side models linear propagation effects. α is the linear loss, β_k are the dispersion coefficients from the Taylor expansion of β about ω_0. The right hand side of the equation contains the nonlinear effects. γ is the nonlinear coefficient given previously in equation 2.8. $\tau_{\text{shock}} = 1/\omega_0$ is the characteristic time scale for self steepening and optical shock formation, which can be generalised if necessary to include the wavelength dependence of effective area [71]. $R(t)$ is the Raman response function, which includes the instantaneous electronic and delayed Raman contributions. The right hand side also contains Kerr nonlinearity.

The full GNLSE (equation 2.15) does not have an analytical solution. The split step Fourier method is used to solve it. A differential operator $\hat{D}$ and a nonlinear operator $\hat{N}$ can be used

to express the full GNLSE in the form

$$\frac{\partial A}{\partial z} = [\hat{D} + \hat{N}]A \tag{2.16}$$

where the operators are given by

$$\hat{D} = -\frac{\alpha}{2} + \sum_{k\geq 2} \frac{i^{k+1}}{k!}\beta_k \frac{\partial^k}{\partial T^k} \tag{2.17}$$

$$\hat{N} = i\gamma \left(1 + i\tau_{shock}\frac{\partial}{\partial T}\right)\left(\int_{-\infty}^{\infty} R(T')|A(z, T-T')|^2 dT'\right) \tag{2.18}$$

The nonlinear operator can be solved in the time domain, and the dispersive operator solved in the frequency domain. The total propagation length is split into discrete steps of length h. The nonlinear and dispersive operators are solved one after the other at each step. Of course in reality, the dispersive and nonlinear effects occur simultaneously. As long as h is small compared to the dispersion length and the nonlinear length, the simulation will yield accurate results. Some other numerical considerations are that the time window should be wide enough to fully enclose the temporal pulse. Also, the number of points in the simulation must give adequate resolution in both the temporal and spectral domain.

The nonlinear step involves integration using a 2nd order Runge-Kutta method. This method finds a solution over the interval by combining the information from two Euler steps, as follows

$$k_1 = hf(x_n, y_n) \tag{2.19}$$

$$k_2 = hf(x_n + \frac{1}{2}h, y_n + \frac{1}{2}k_1) \tag{2.20}$$

$$y_{n+1} = y_n + k_2 \tag{2.21}$$

where $f(x_n, y_n)$ is the derivative of the function at the starting point, and h is the step size. This advances the solution from x_n to $x_{n+1} = x_n + h$. For the dispersion step, the temporal field is Fourier transformed and the dispersion can be added straightforwardly in the frequency domain.

The effect of laser noise can be modelled using the code. This is of crucial importance for understanding how to generate low noise supercontinuum. Fundamental quantum shot noise is modelled semi-classically by adding one photon with random phase to each frequency bin. Laser technical noise can also be modelled by adding a random intensity within a specified percentage of the overall intensity to each point in time.

The mutual spectral coherence can then be calculated over a large number of single-shot simulations, using the following expression [72]

$$|g_{12}(\lambda, t_1 - t_2)| = \left| \frac{\langle E_1^*(\lambda, t_1) E_2(\lambda, t_2) \rangle}{[\langle |E_1(\lambda, t_1)|^2 \rangle \langle |E_2(\lambda, t_2)|^2 \rangle]^{1/2}} \right| \tag{2.22}$$

where $t_1 - t_2$ is the time between consecutive pulses, and the angular brackets denote an ensemble average over independently generated pairs of spectra. For $t_1 - t_2 = 0$ this expression is equal to the visibility of interference fringes which can be produced experimentally [73], and therefore is a very practical measure of the supercontinuum coherence.

Chapter 3

Photonic crystal fibres with all normal group velocity dispersion

3.1 Introduction

The aim of this research was to produce a supercontinuum which does not suffer from coherence-destroying intensity and phase fluctuations. The proposed method for achieving this is to generate supercontinuum in a PCF with all-normal dispersion, thus eliminating soliton effects. This chapter gives background and theory justifying the use of this method, and details of the fibre design and fabrication.

As described in the previous chapter, current state-of-the-art supercontinuum sources rely on pumping nonlinear fibres in the anomalous dispersion regime, close to the zero-dispersion wavelength (ZDW). Spectral broadening in this case is created by the process of soliton fission, SSFS and dispersive wave generation. This process is sensitive to pump pulse fluctuations, and can be induced by noise-seeded MI, resulting in large differences in spectral structure from pulse to pulse [69, 72]. Seen another way, this causes large fluctuations in intensity and phase from pulse to pulse at any specific wavelength within the supercontinuum spectrum, resulting in poor spectral coherence [74]. There is also a complex structure on the spectrum in each single shot, which is washed out when measured over many shots [75].

Intensity and phase fluctuations can be a problem for applications. Coherence is important for the generation of frequency combs for frequency metrology [73]. The generation of ultra-short pulses by re-compression of supercontinua is limited by poor spectral coherence and complex spectral structure [62, 63, 76]. A stable source is important for applications such as fluorescence microscopy [77], optical coherence tomography (OCT) [58] and coherent anti-stokes Raman scattering (CARS) spectroscopy [78]. For microscopies where the laser focus is raster scanned across a sample to build up a 2-D image or 3-D image, instabilities in the intensity would reduce the resolution.

Supercontinuum fluctuations can be improved in a variety of different ways. These ap-

proaches involve either reducing or eliminating soliton dynamics. To reduce the dominance of MI seeded soliton dynamics, the soliton fission should occur before MI gain becomes significant, ie. the soliton fission length should be much shorter than the MI length. The propagation length after which MI becomes significant is approximately $L_{MI} = 16L_{\mathrm{NL}}$ where L_{NL} is the nonlinear length given by equation 2.7. The fission length is given by $L_{\mathrm{fiss}} = L_D/N$ where L_D is the dispersion length given in equation 1.8, and the soliton order $N^2 = L_D/L_{\mathrm{NL}}$. Therefore, for a coherence-maintaining supercontinuum a rule of thumb is $N << 16$ [69]. So, by keeping the soliton order low, high coherence can be achieved. This can be done by pumping deep in the anomalous dispersion regime where the dispersion is high [79]. Low soliton order can also be achieved by using very short pulses, typically less than 100 fs [69, 80].

Another way to reduce the extent of soliton effects is to use PCF with two closely spaced ZDWs [81–83]. In these fibres broadening is due to soliton fission and self frequency shift, and dispersive wave generation on the normal dispersion side of each ZDW. Because the Raman shift of the solitons in the anomalous dispersion region of the fibre is limited, the resulting spectrum is stable. However, the spectrum develops a two-peak structure which has limited applications. Fibres with two ZDWs can be tapered so that their dispersion is gradually made "more normal" and have an all-normal dispersion profile after some length. This allows initial broadening due to soliton dynamics, which then ceases once the fibre dispersion is all-normal [84]. Alternatively, if the fibre is tapered from anomalous to normal in such a way as to inhibit soliton breakup, then the result is a highly coherent supercontinuum [85]. Another scheme to reduce intensity noise uses an optical feedback loop [86].

The simplest way to eliminate soliton effects altogether is to pump in the normal dispersion regime of the fibre where solitons do not form, and spectral broadening occurs via SPM only. Broadening by SPM is not sensitive to pump pulse fluctuations and produces a coherent supercontinuum. However, if the spectrum extends on the long wavelength side into the anomalous dispersion regime of the fibre, soliton dynamics will come into play and reduce the coherence. To avoid this in conventional fibres, the pump wavelength should be far below the ZDW, in the normal dispersion regime. The spectral broadening will be therefore limited by the large magnitude of the dispersion. This problem can be reduced by taking advantage of the widely engineerable dispersion of solid core PCF as described in chapter 1. Over a narrow range of pitch (Λ) and hole size (d) values, PCF can be fabricated which have normal GVD over the entire visible and near infra-red wavelength range, and low dispersion at the desired pump wavelength. A range of all-normal dispersion curves modelled using the empirical formula described in [32] are plotted in figure 3-1 to illustrate this. Because the dispersion is always normal, there can be no phase matching for seeded four-wave mixing processes. Close to the minimum dispersion wavelength, the second order dispersion is low, which is an advantage for re-compressing the supercontinuum pulses using linear chirp compensation techniques such as a grating pair or prism pair compressor. Chapter 4 of this thesis contains results of re-compression of an all normal dispersion supercontinuum using a prism pair.

In this chapter the design and fabrication of two different all-normal dispersion PCF with low dispersion for pumping at 1064 nm and 800 nm are described. These are common laser

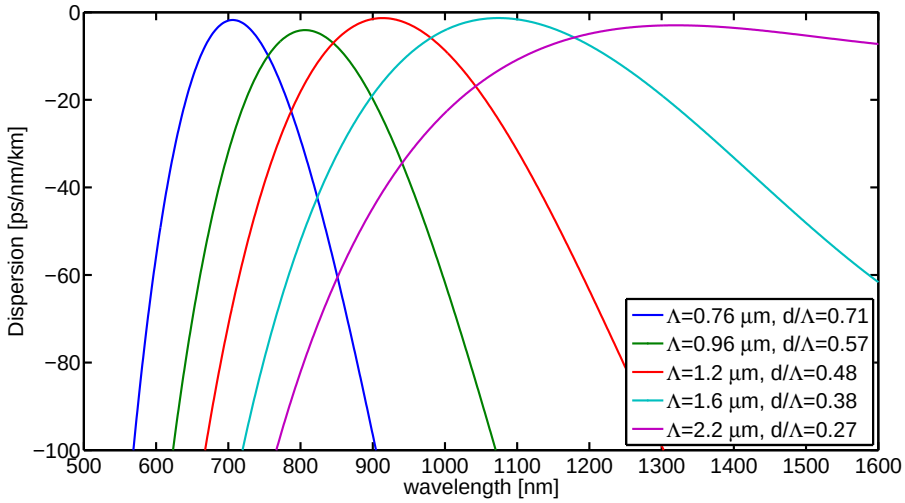

Figure 3-1: Dispersion calculated using empirical formula, showing how by varying pitch Λ and hole size d, all-normal dispersion profiles can be achieved, with low dispersion at a range of wavelengths in the visible and near infra-red range

wavelengths. The 1064 nm fibre (ND1064) was pumped using a compact ytterbium-doped amplified mode-locked fibre laser (Fianium Ltd), and the 800 nm fibre (ND800) was pumped using a Ti:Sapphire laser system. The 1064 nm fibre laser is of particular interest for applications because it is small and portable, so could form part of a mobile device such as a spectroscopy system for diagnostics. Ti:Sapphire systems are commonplace in laser research labs, so many existing set-ups currently using an anomalously pumped supercontinuum PCF could use an all-normal dispersion PCF, and benefit from lower noise in their experiment, provided the generated bandwidth is adequate.

Previously, all-normal or dispersion flattened fibres existed for pumping at telecommunications wavelengths [87]. A PCF with an all-normal dispersion profile centred at 1060 nm was presented in [82], however at pJ pulse energies no significant broadening was observed. Now, powerful fibre laser sources centred at 1064 nm are available which make supercontinuum generation in all normal dispersion PCFs achievable. A fibre with all-normal dispersion profile for pumping at 1064 nm was fabricated by the author, and original work including the first results of supercontinua generated in all-normal dispersion fibre at 1064 nm were submitted to a conference [88]. A few months later, before the author's conference paper was published, a purely theoretical paper was published by another group previously unknown to the author, proposing all-normal dispersion PCF for 1064 nm pumping [89]. After this, an all normal dispersion PCF for pumping at 1064 nm similar to that fabricated by the author became commercially available [90]. The commercial fibre was used by other groups working concurrently on all-normal dispersion supercontinuum experiments [59, 60, 89, 91–94].

For 800 nm pumping, low noise supercontinuum fibres with two ZDWs are available com-

mercially [95]. Some PCF with all normal dispersion for 800 nm pumping have been fabricated by others using a post-processing method [96], however using this technique only a small length of fibre can be created, so the spectral broadening is limited. The first all-normal dispersion fibre for 800 nm pumping not requiring post processing was fabricated as part of this thesis work.

3.2 Simulations

Simulations were carried out using the GNLSE code described in the previous chapter, to demonstrate the spectral coherence properties of supercontinua generated in both anomalous and all-normal dispersion PCF. The parameters used in the simulation are based on real PCFs; the anomalous dispersion PCF is a "white light" supercontinuum fibre with anomalous dispersion at 1064 nm [51], and the all-normal dispersion fibre was fabricated during this research with minimum dispersion of -6 ps/nm/km at 1064 nm (ND1064). The dispersion curves for both fibres are plotted in 3-2. The pump was a sech^2 pulse, with 20 kW peak power centred at 1064 nm. Raman scattering and self steepening were included. Propagation was modelled over a 10 cm length of fibre. The results of the simulations are plotted in figure 3-3. From left to right the input pulse duration is varied. The top two rows show the temporal and spectral profiles of the generated supercontinua. For each set of pulse and fibre conditions, 20 single-shot calculations were performed, each with a random quantum noise seed added to simulate fundamental quantum noise in the laser cavity. All 20 spectral and temporal profiles are plotted in grey, and the average is plotted in black. The bottom row shows spectral coherence, calculated over the ensemble of 20 independently generated supercontinua.

The temporal and spectral profiles in figure 3-3 (a) are typical of anomalous dispersion pumping. Multiple pulses corresponding to Raman shifted solitons can be seen in the spectral and temporal domain. For the 100 fs input pulse the spectrum is relatively stable, and the average spectrum has a complex spectral structure. For longer input pulses, the individual simulations have a complex spectral structure, but from shot to shot there are large fluctuations. The spectral and temporal intensities take large excursions from their average values. The resulting average spectral profile therefore appears smooth. This smooth spectrum represents what is observed when measuring a supercontinuum using a standard spectrometer, which due to the integration time averages over many thousands of pulses. The coherence plots show that the spectral coherence is high for 100 fs pulse duration, and is destroyed at wavelengths away from the vicinity of the pump for longer pulse durations. This trend can be explained by the relative dominance of MI in each case. For a short pulse, the fission length L_{fiss} is short, and soliton fission broadens the spectrum before MI has a strong effect, resulting in good spectral coherence and stability. For long input pulses, the fission length L_{fiss} is long, and MI becomes more significant, resulting in poor spectral coherence away from the vicinity of the pump.

The temporal and spectral profiles of the all-normal dispersion supercontinua in figure 3-3 (b) all have SPM peaks at the centre of the spectrum. For an input pulse with a FWHM of 300 fs, the spectrum is generated purely by SPM. For shorter input pulses, side lobes are

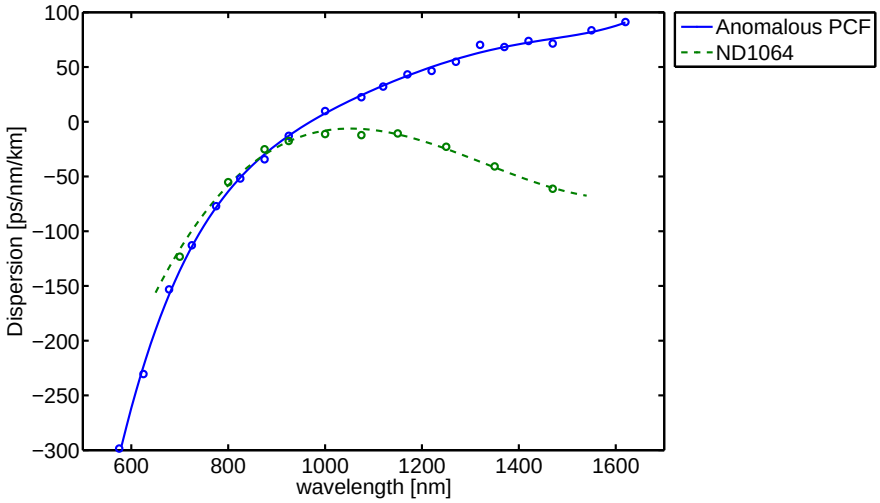

Figure 3-2: Measured dispersion profiles of two supercontinuum photonic crystal fibres used in simulations: a photonic crystal fibre with anomalous dispersion at 1064 nm [51] and all-normal dispersion photonic crystal fibre, ND1064. Circles show two-point differences measured from group delay data. Lines are the derivative of a 6th order polynomial fit to the group delay data for the anomalous dispersion photonic crystal fibre, and a 4th order polynomial fit to group delay data for ND1064. The polynomial order was chosen to give the best fit to the group delay data

generated at the short and long wavelength edges of the spectrum, which is a result of optical wave breaking. This is a FWM effect, resulting from the steepening of the pulse edges in the temporal domain under normal dispersion. This effect is described fully in chapter 4. The coherence of the all-normal dispersion PCF supercontinua in figure 3-3 (b) is unity over the entire bandwidth, for all values of input pulse duration. The spectral and temporal profiles are practically identical from shot to shot. The supercontinuum also remains a single pulse in the time domain, unlike the multi-pulse temporal profiles seen in the anomalous pumping case. Also unlike the anomalous dispersion supercontinua, there is a significant reduction in supercontinuum bandwidth for longer pulse lengths. As the peak power is kept constant for these simulations, the reduced broadening is a result of the reduced intensity gradient on the pulse.

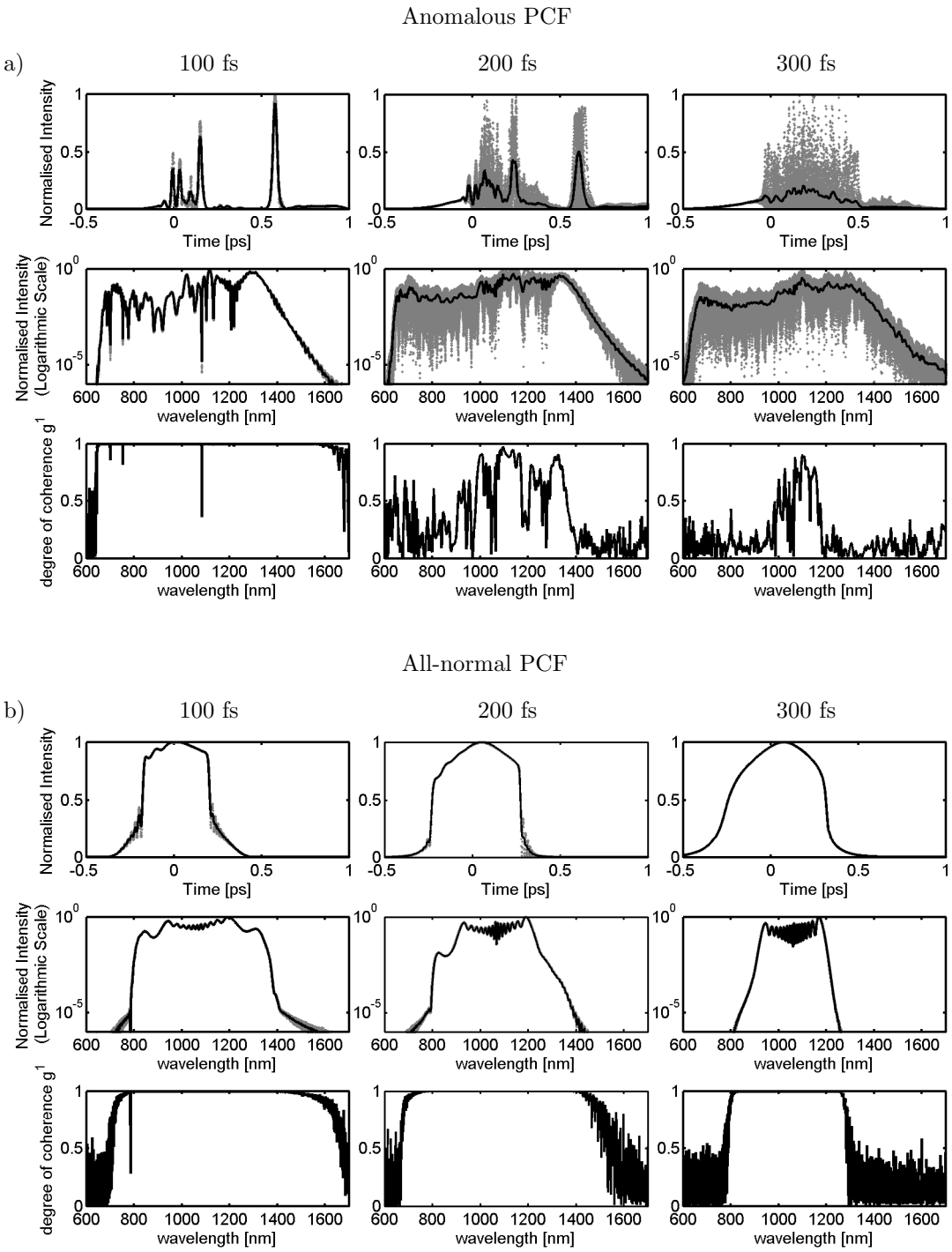

Figure 3-3: Simulated supercontinua generated using sech^2 pulses centred at 1064 nm with 20 kW peak power, in a) anomalous dispersion supercontinuum PCF and b) all-normal dispersion supercontinuum PCF (ND1064). In each plot the top two rows show temporal and spectral profiles of 20 individually generated supercontinua with random quantum noise seed added plotted in grey, and the average profiles plotted in black. On the bottom row is plotted the mutual degree of spectral coherence calculated over the 20 individually generated supercontinua. The pulse FWHM is varied between 100 fs and 300 fs from left to right

3.3 All-normal dispersion fibre for 1064 nm pumping

3.3.1 Design

The dispersion of solid-core PCF can be modified by changing the pitch, Λ, and hole size, d, of the cladding. To give an indication of the fibre dimensions required to produce an all-normal dispersion profile, dispersion modelling was carried out using two methods. One is the empirical formula described in reference [32]. In this paper, an empirical formula to predict dispersion is fitted to Finite Element Method modelling of various solid core fibres with d/Λ ratios between 0.2 and 0.8. The range of Λ over which the formula is valid is dependent upon wavelength and d/Λ ratio. The empirical formula provides a simple and time-efficient way of predicting dispersion profiles for simple solid core fibres; however it is not valid over all possible PCF dimensions. The second method uses "CUDOS MOF" [35, 36], a software package which uses the multi-pole method to calculate modes in PCF. It returns the effective refractive index of each mode, from which dispersion can be calculated using equation 1.7. When calculating the modes, CUDOS takes into account the number of rings of air holes in the cladding, in addition to Λ and d, and can therefore be used to calculate confinement loss as well. CUDOS is more reliable than the empirical code for calculating dispersion, as it is valid over all fibre dimensions. However, it is more time consuming. Therefore when modelling the dispersion, the empirical code is used to obtain an initial guess at required fibre parameters, and then a PCF with these parameters are modelled using CUDOS to obtain a more accurate result.

To create an all-normal dispersion PCF with low dispersion at 1064 nm, the "ideal" parameters are $\Lambda = 1.65$ μm and $d/\Lambda = 0.38$ according to the empirical code. This is compared with the result obtained using CUDOS in figure 3-4. There is a good match between the dispersion profiles, so the empirical code is valid for these fibre parameters.

There are a number of combinations of Λ and d/Λ which will produce low dispersion close to 1064 nm, however practically it is convenient to base the fibre d/Λ on the inner diameter/outer diameter ratio (ID/OD) of a commercially available fused silica tube. A tube with ID/OD = 0.38 is in the correct range for this fibre, so this is what set the d/Λ in the design. Capillaries can be inflated by a small amount during the draw, and the holes in the cane and fibre can also be inflated/collapsed as they are being drawn. However, if the d/Λ in the stack is very different from the d/Λ in the final fibre then the overall geometry deviates from the geometry used in the modelling. The core size might be small or large in relation to the photonic crystal cladding, which will have an impact on fibre dispersion.

Figure 3-5 shows the effect of variations in Λ and d/Λ on the dispersion, in the vicinity of the parameters used. These dispersion curves were calculated using the empirical formula. A change of just 0.01 in d/Λ results in a significant change in dispersion, as does a change of 0.1 μm in Λ. This emphasises the difficulty of fabricating the precise fibres required for this research. Qualitatively, the effect of changing Λ and d/Λ can be analysed from these diagrams. Increasing d/Λ moves the dispersion curve towards the anomalous, and increasing Λ has the same effect, as well as shifting the turning point towards longer wavelengths.

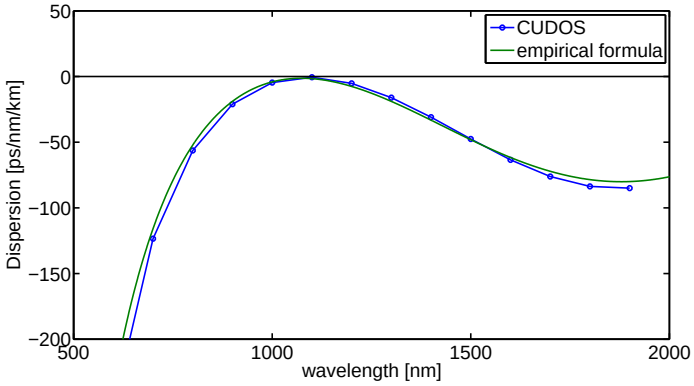

Figure 3-4: Comparison of dispersion curves calculated using the empirical formula and CUDOS for $\Lambda = 1.6$ μm and $d/\Lambda = 0.38$. Good agreement demonstrates the validity of the empirical formula for these parameters

a)

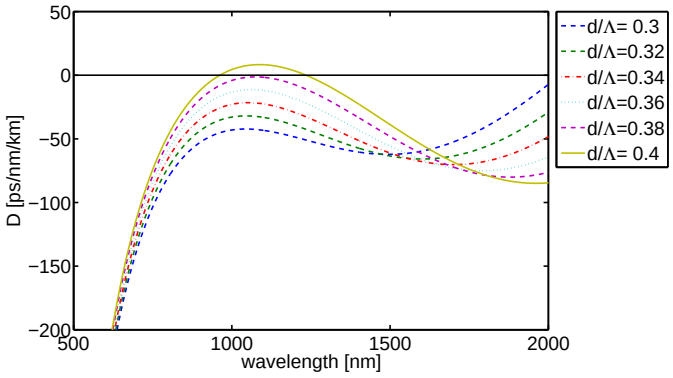

b)

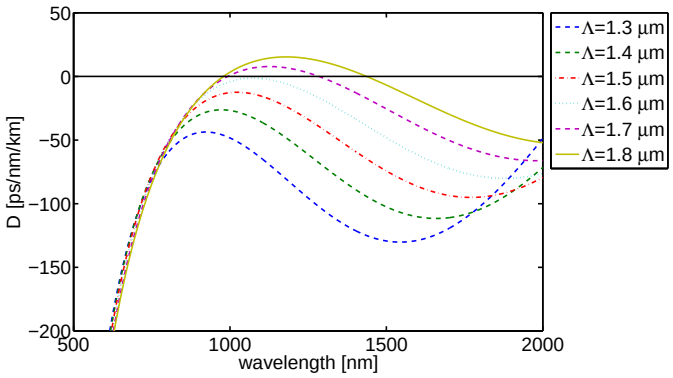

Figure 3-5: Dispersion curves calculated using the empirical formula, to show how sensitive dispersion is to fibre parameters in this range. a) d/Λ is varied close to $d/\Lambda = 0.38$ for constant $\Lambda = 1.6$ μm, b) Λ is varied close to $\Lambda = 1.68$ μm for constant $d/\Lambda = 0.38$.

3.3.2 5 ring fibre

The first set of PCFs fabricated had a 5 rings of air holes surrounding a central core. This number of rings was chosen as a compromise between ease of fabrication - requiring fewer rings, and the degree of confinement provided by the cladding - requiring more rings. The design and fabrication of this fibre was carried out by both the author and Alistair Muir. The stack design is shown in figure 3-6 (a). Solid packers are included at the edge of the stack, to ensure a snug fit into the jacketing tube, preventing distortion during the cane and fibre draw. The stack was drawn into approximately 30 canes with an outer diameter of 3 mm, with $\Lambda = 136$ μm and $d/\Lambda = 0.45$. An optical microscope image of a cane cross section is shown in figure 3-6 (b).

To draw fibre, one of the canes was inserted into a jacketing tube with 3 mm inner diameter (ID) and 10 mm outer diameter (OD). During the draw vacuum is applied between the cane and jacketing tube, and pressure is applied to the holes. During the first draw the pressure in the holes was varied between 10 kPa and 15 kPa. The feed rate and draw rate were set to give a fibre OD of 125 μm, and this was kept constant throughout, with a temperature of 2050 °C and a tension around 363 grams. Five fibres were drawn with Λ between 1.64 μm and 1.73 μm, and d/Λ between 0.13 and 0.33, measured from scanning electron microscope (SEM) images. The d/Λ of all the fibres was smaller than the required 0.38. A second fibre draw was therefore carried out, using higher pressure. The pressure was varied between 15 kPa and 20 kPa, with temperature constant at 2020 °C and the tension was approximately 250 grams. Twelve different PCF were drawn with Λ between 1.22 μm and 1.71 μm, and d/Λ between 0.21 and 0.63, measured from SEM images.

The empirical formula predictions were used in the first instance to give an indication of which fibres from the draw might have an all-normal dispersion profile. A dispersion measurement for single PCF can take up to a few days, whereas modelling using the empirical formula takes only a few seconds. Fibres with modelled dispersion curves close to the desired all-normal profile can then be characterised in the lab. The dispersion profiles predicted by the empirical formula for some of the PCFs fabricated during the second draw are plotted in figure 3-7. According to the empirical formula, fibres 2 and 3 have all-normal dispersion profiles. SEM images of each of the fibres are also included in figure 3-7. There is some distortion to the holes at the edge of the cladding, due to an insufficient number of packers around the outside of the stack.

The dispersion of fibre 3 was measured using the method described in chapter 1, and is plotted in figure 3-8. This is compared with the prediction using the empirical formula. The measured dispersion is "more anomalous" than the modelled dispersion, and this was found to be true for all measured dispersion profiles presented in this chapter. This is discussed in detail in section 3.3.3.

The transmission of the 5-ring fibres was found to be poor at long wavelengths, suggesting that there is significant confinement loss. For this reason, no further fibre draws were carried out using the 5-ring canes.

a) b)

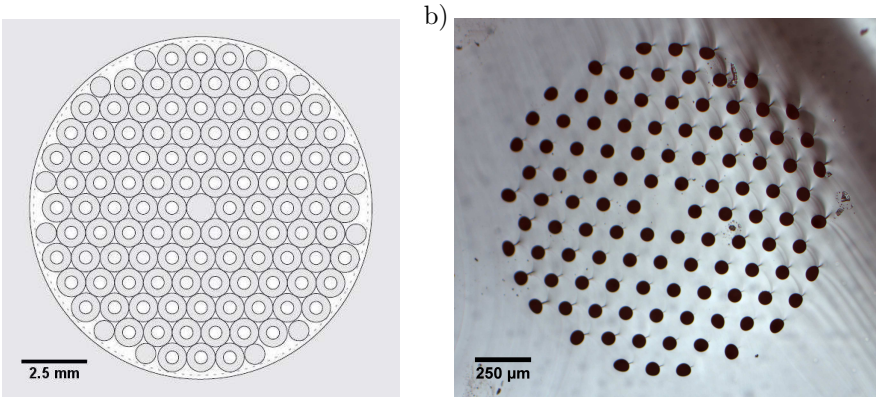

Figure 3-6: 5-ring fibre a) stack design and b) optical microscope image of 5-ring cane cross section with $\Lambda = 136$ μm and $d/\Lambda = 0.45$

a)

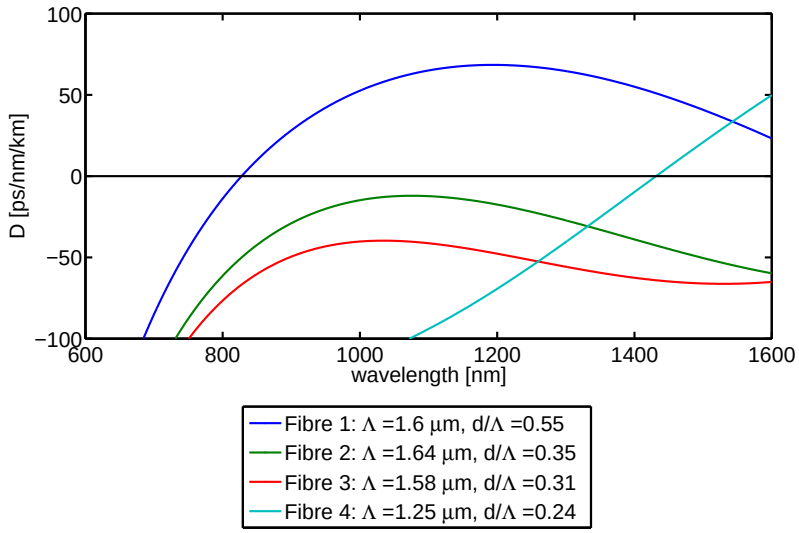

b)

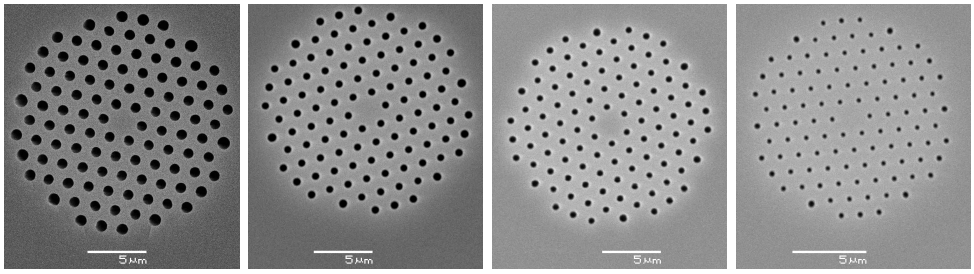

Fibre 1 Fibre 2 Fibre 3 Fibre 4

Figure 3-7: a) Dispersion profiles calculated using empirical formula for a selection of 5-ring fibres produced in second fibre draw b) Scanning electron microscope images of each 5-ring fibre. Scale bars are 5 μm

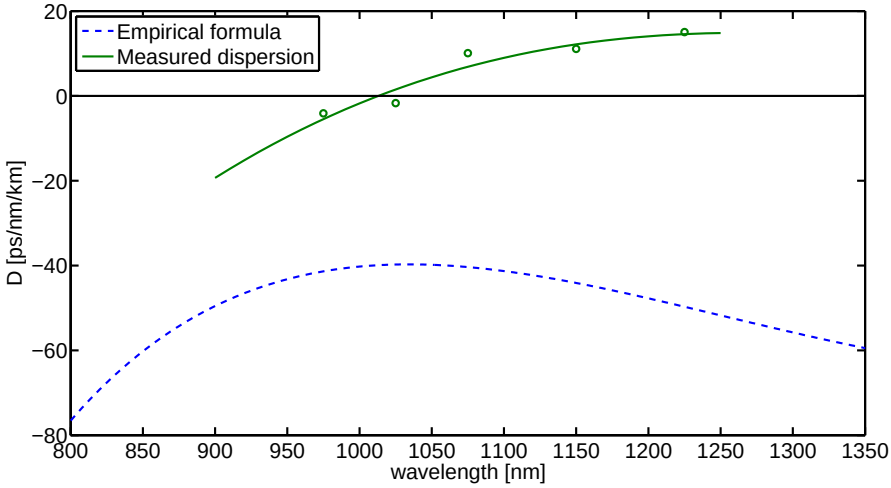

Figure 3-8: Empirical prediction of dispersion, and measured dispersion of "Fibre 3" with $\Lambda = 1.58\ \mu m$ and $d/\Lambda = 0.31$. The measured dispersion points are two-point differences derived from measured values of group delay, and the solid line is the derivative of a 4th order polynomial fit to the group delay data

3.3.3 8 ring fibre

To reduce fibre confinement loss, a second stack was created with 8 rings of air holes surrounding the core. The design and fabrication of this fibre was carried out by the author alone. The stack design is shown in figure 3-9 (a). More solid packers are included than in the previous stack to prevent distortion of the structure. The stack was drawn to produce around 30 canes with 3 mm diameter. An optical microscope image of the cane used to draw fibre can be seen in figure 3-9 (b). This cane has $\Lambda = 122\ \mu$m and $d/\Lambda = 0.40$.

One fibre draw was carried out. During the draw the feed and draw speed were set to give the required fibre outer diameter of approximately 130 μm, and the temperature remained constant at 2030 °C, giving a fibre tension of 255 g. The pressure in the holes was varied between 18 kPa and 22 kPa, giving 5 different fibres with Λ ranging between 1.58 and 1.64 μm, and d/Λ ranging from 0.18 to 0.32. The dispersion profiles predicted by the empirical formula for all five fibres are plotted in figure 3-10. According to the modelling, fibres 4 and 5 have low all-normal dispersion.

The dispersion of fibre 5 was measured, and is plotted in figure 3-11. The dispersion profile is all normal and has a minimum value of -6 ps/nm/km at 1064 nm. This fibre is therefore ideal for generating supercontinuum centred at 1064 nm. The fibre is re-named "ND1064" and used in experiments in chapters 4 and 5 of this thesis.

The empirical formula predicted dispersion is also plotted in figure 3-11. The measured dispersion is closer to the empirical calculation of dispersion than it was for the previous 5-ring fibre. However, the measured dispersion is more anomalous than the modelled dispersion, and this is true for all measured dispersion profiles in this chapter. This suggests that there is a

a) b)

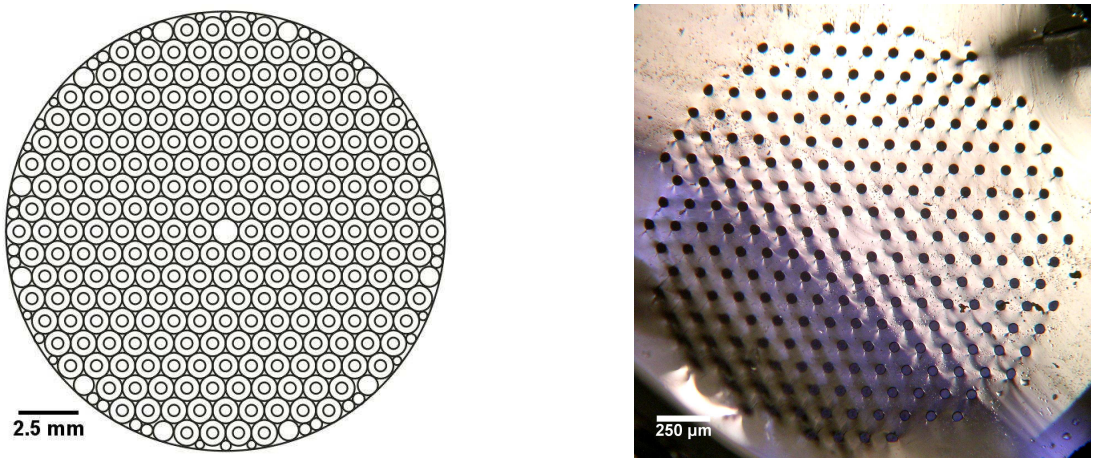

Figure 3-9: 8-ring fibre a) Stack design and b) Optical microscope image of a cane cross section with $\Lambda = 122\ \mu m$ and $d/\Lambda = 0.40$

systematic error in the measurement of the hole size from the fibre SEM images.

The empirical formula predicts a hole diameter close to 600 nm, for good agreement with the measured dispersion. However, the hole diameter measured from the SEMS is 530 nm. One possible reason for this difference could be the gold coating applied to the sample, which is approximately 100 nm thick and helps to provide a good secondary electron signal. The gold coating could enter the air holes, making them appear smaller than they really are. Also, when imaging secondary electrons, charge tends to build up at the air hole edges, creating a bright halo around the hole and making the position of the hole edges less certain. Since the research presented elsewhere in this chapter was carried out, these effects were investigated.

Figure 3-12 (a) shows a secondary electron image of the ND1064 cladding, with a 100 nm gold coating. The average hole diameter measured from this image was 530 nm. The charging at the hole edges is clear in this image. To remove the problem of charging, an image of the same coated sample was obtained at low vacuum using back-scattered electrons. This image is shown in figure 3-12 (b). Due to there being no charging, the hole size appears larger, and the hole diameter measured from this image is 560 nm. An uncoated sample was also imaged using the back-scattered signal, and is shown in figure 3-12 (c). The hole size appears much larger, and the average measured diameter is 640 nm. This proves that the gold coating can enter the air holes. However, the hole diameter is much larger than the 600 nm predicted by the empirical formula, the reason for which is not understood. In general, the accuracy of the hole diameter measured from SEM images is highly dependent on the image quality, the amount of charging on the sample and the detection geometry used. The absolute values of hole diameter presented in this thesis may not be accurate, but having been measured under the same conditions, their relative differences can provide valuable information.

a)

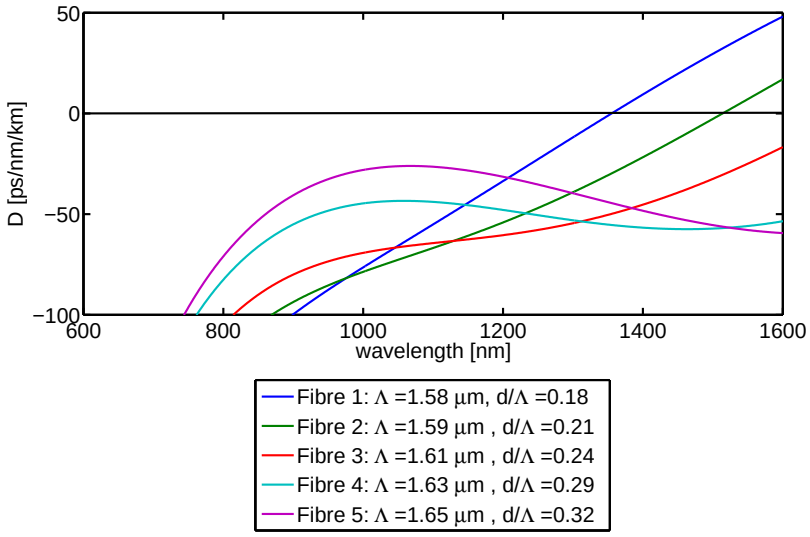

b)

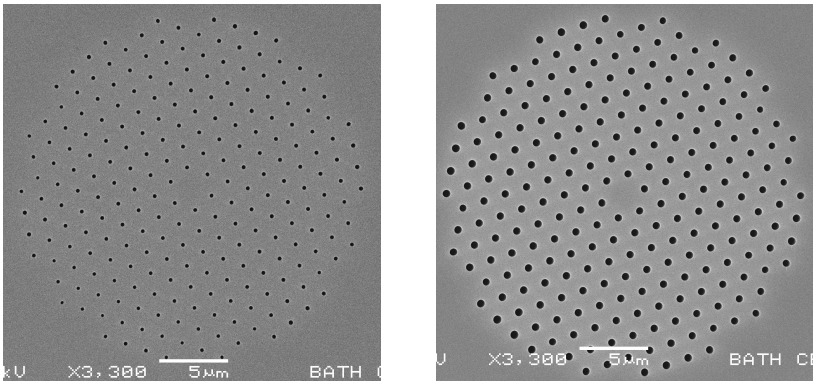

Fibre 1 Fibre 5

Figure 3-10: a) Dispersion profiles calculated using empirical formula for all 8-ring fibres b) Scanning electron microscope images of Fibre 1, with $\Lambda = 1.58\ \mu m$, $d/\Lambda = 0.18$ and Fibre 5, with $\Lambda = 1.65\ \mu m$, $d/\Lambda = 0.32$. Scale bars are 5 μm

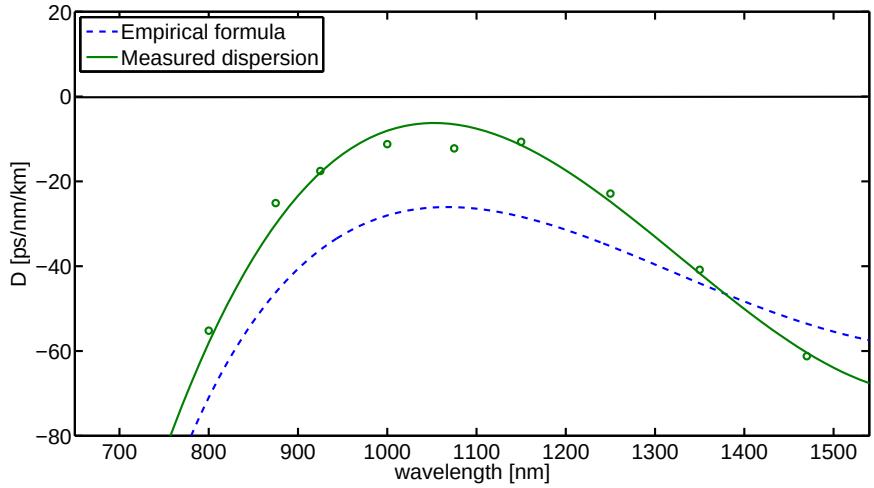

Figure 3-11: Dispersion calculated using empirical formula and measured dispersion of "ND1064" (Fibre 5) with $\Lambda = 1.65$ μm and $d/\Lambda = 0.32$. The measured dispersion points are two-point differences derived from measured values of group delay, and the solid line is the derivative of a 4th order polynomial fit to the group delay data. Dispersion measurements were carried out using a white light supercontinuum source pumped at 1064 nm, so there is reduced accuracy in the data near this wavelength

a) Secondary electron image, gold coated

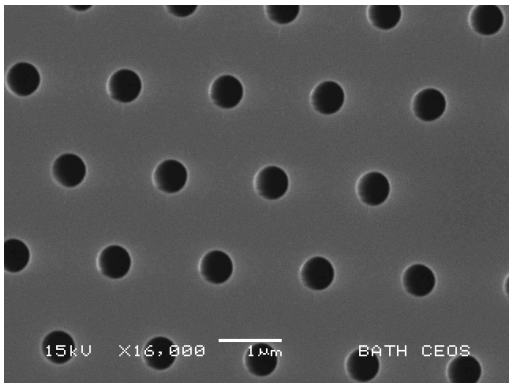

b) Back-scattered electron image, gold coated

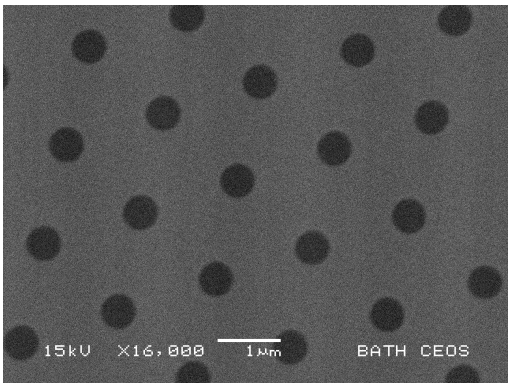

c) Back-scattered electron image, uncoated

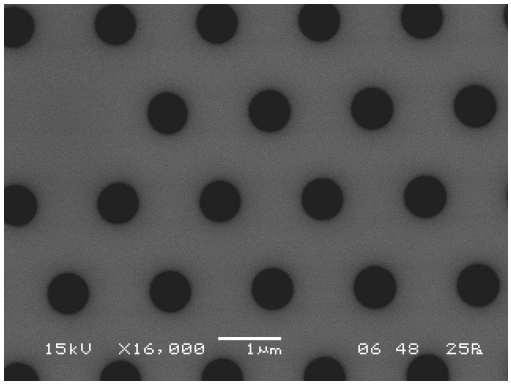

Figure 3-12: Scanning electron microscope images of ND1064 cladding, comparing the appearance of the hole size when imaging using secondary electrons or back-scattered electrons, and showing the difference between a gold-coated and an uncoated sample. Scale bars are all 1 μm

3.4 All-normal dispersion fibre for 800 nm pumping

3.4.1 Design

An all-normal dispersion fibre was fabricated with low dispersion for pumping at 800 nm, for use with Ti:Sapphire laser systems. According to the empirical formula, low dispersion at 800 nm is achieved in a PCF with $\Lambda = 0.96$ μm and $d/\Lambda = 0.57$. The dispersion of a PCF with these parameters was also modelled using CUDOS, and a comparison is plotted in figure 3-13. The agreement is not as good as it was for the previous fibre, because the empirical formula is based on PCF with Λ between 2 μm and 3 μm, and so becomes more inaccurate as Λ becomes much less than 2 μm. Again, the d/Λ was based on an available tube ID/OD.

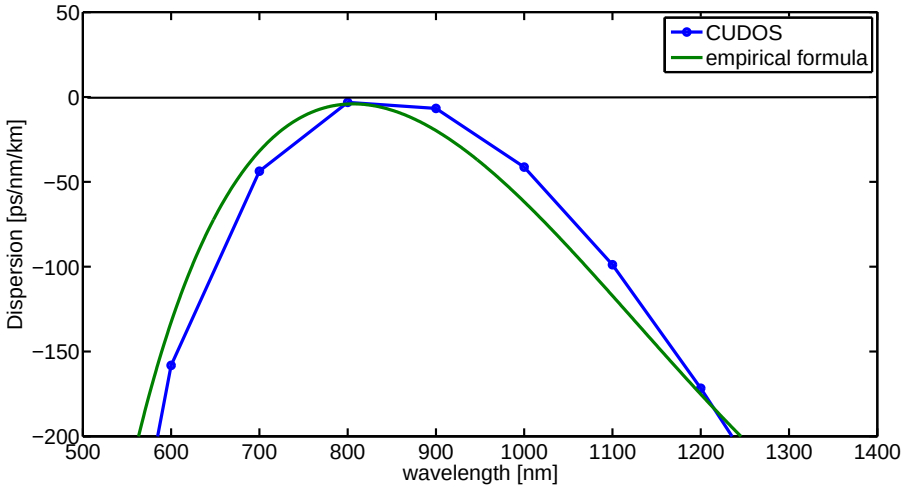

Figure 3-13: Comparison of calculated dispersion using the empirical formula and CUDOS for $\Lambda = 0.96$ μm and $d/\Lambda = 0.57$

The sensitivity of the dispersion to the fibre parameters is high for such small Λ. This is evident from the dispersion curves calculated using the empirical formula in figure 3-14. Λ and d/Λ are varied close to their "ideal" values, in the same increments used for figure 3-5. The sensitivity of the dispersion to d/Λ in the 800 nm PCF is slightly higher than for the 1064 nm PCF, however the sensitivity of dispersion to Λ is significantly higher.

a)

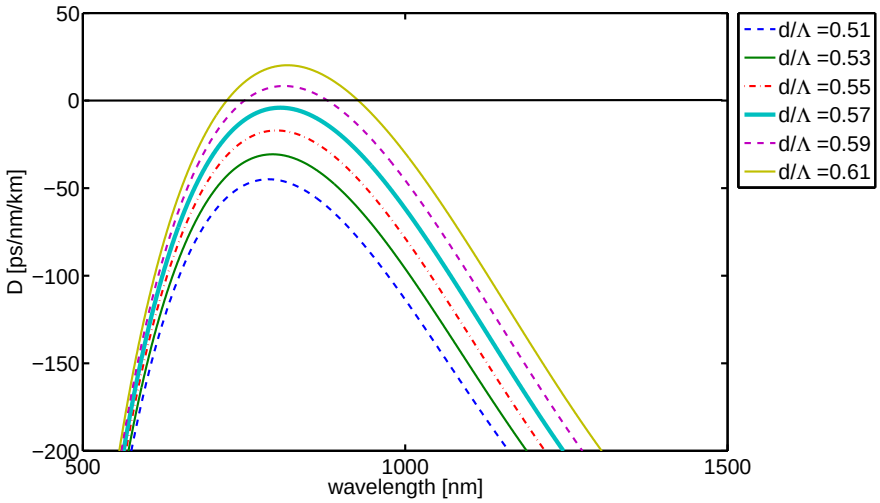

b)

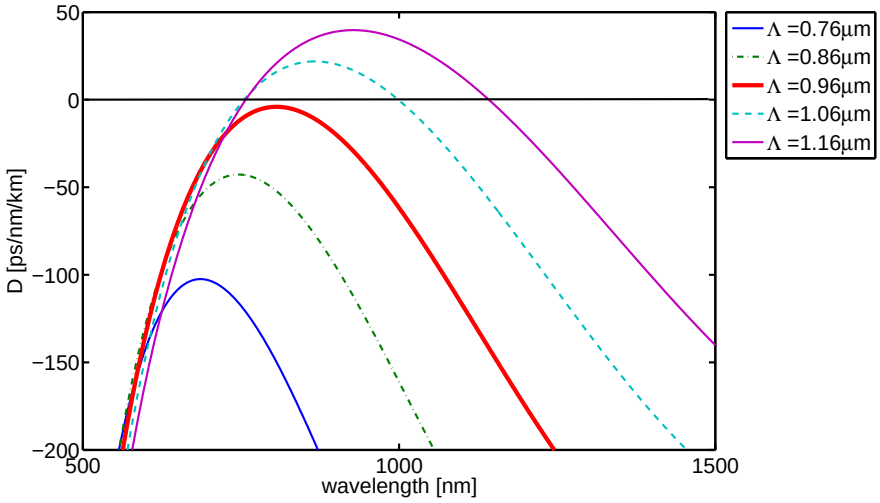

Figure 3-14: Dispersion curves calculated using the empirical formula, to show how sensitive dispersion is in this parameter range. a) d/Λ is varied close to $d/\Lambda = 0.57$ for constant $\Lambda = 0.96$ μm, b) Λ is varied close to $\Lambda = 0.96$ μm for constant $d/\Lambda = 0.57$

3.4.2 Fabrication

Initially fibres for 800 nm pumping were drawn by the author using the 8-ring canes designed for the 1064 fibre. To obtain the correct pitch, the outer diameter of the final fibres was reduced to approximately 80 μm. In the first two draws, the tension was reduced to around 150 grams to avoid fibre breaks. The low tension increases sensitivity of hole size to the pressure. The air holes were only present at pressures between 19 kPa and 22 kPa, below this range the holes collapsed completely and above this range the holes over-inflated, destroying the cladding structure. The hole sizes in the range varied between 100 nm and 500 nm. The all-normal dispersion profile is extremely sensitive to hole size; a 20 nm hole diameter difference modifies the dispersion by approximately 10 ps/nm/km. On the fibre drawing tower the pressure may be adjusted in increments of 0.1 kPa, however the hole size could not be tuned with pressure accurately enough. The cladding was also not generally uniform, and had distorted holes close to the core.

To eliminate the problems with pressure sensitivity during the draw, a new stack was made specifically for the 800 nm fibre. This was designed so that the final fibre had an outer diameter close to that of a standard fibre, and therefore it could be drawn at a higher tension. The stack design was the same as the 8 ring stack shown in figure 3-9, but this time with a smaller cladding region and thicker jacketing tube.

Two fibre draws using canes from this stack were carried out by the author. The first was at low tension, close to 177 grams. This resulted in PCF with non uniform cladding. Another draw was done at much higher tension, almost 300 grams. The temperature was dropped to 1958 $^{\circ}C$ to provide the increase in tension. This resulted in much more uniform fibres. The pressure was varied between 25 kPa and 30 kPa, resulting in 11 different PCF with Λ between 0.75 and 1.06 μm and d/Λ between 0.38 and 0.73. 7 of the 11 fibres had all-normal dispersion according to the empirical formula, and these are plotted at the top of figure 3-15. These fibres were also analysed by looking at the spectra obtained by pumping with Ti:Sapphire pulses centred at 800 nm, which are plotted at the bottom of figure 3-15. The spectra were studied because the empirical formula did not match the measured dispersion in previous experiments, and some useful information about the fibre dispersion can be obtained by looking at the supercontinuum generated. The supercontinuum generated in most of the fibres exhibited a two-peak structure characteristic of a spectrum generated in a fibre with two ZDWs. Only the spectra generated in fibres 6 and 7 had characteristic all-normal dispersion spectra. The dispersion of fibre 6 was measured and found to have all normal GVD, plotted in figure 3-16. Again, the measured dispersion is more anomalous than the dispersion predicted by the empirical formula. However, the fibre still has a high value of dispersion at 800 nm (-50 ps/nm/km) and therefore the PCF is not ideal because the high dispersion limits spectral broadening.

Three further draws were carried out by Brian Mangan and Fei Yu, using 800 nm fibre canes fabricated by the author. Draws were carried out at high tension (around 300 grams), over a narrower range of pressures. A range of fibres were fabricated, one with all-normal dispersion and almost zero dispersion at 800 nm. This fibre has $\Lambda = 0.95$ μm and $d/\Lambda = 0.49$, and is fibre

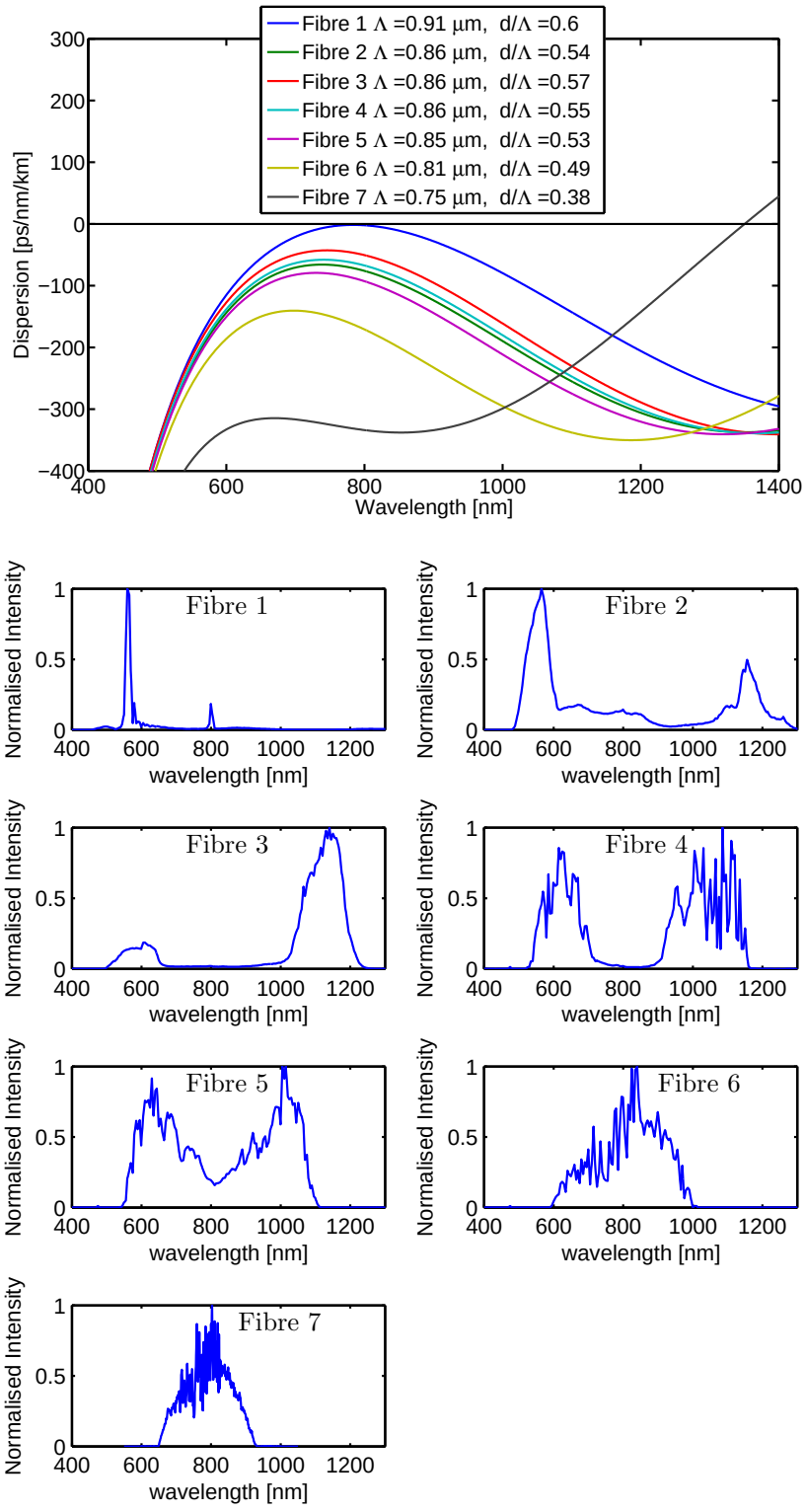

Figure 3-15: Top: dispersion curves calculated using empirical formula, for 7 different fibres drawn from canes designed for 800 nm fibre. Bottom: spectra generated in 30 cm of each of the 7 fibres, pumped with Ti:sapphire pulses centred at 800 nm with 100 mW average output power, 200 fs duration and 76 MHz repetition rate

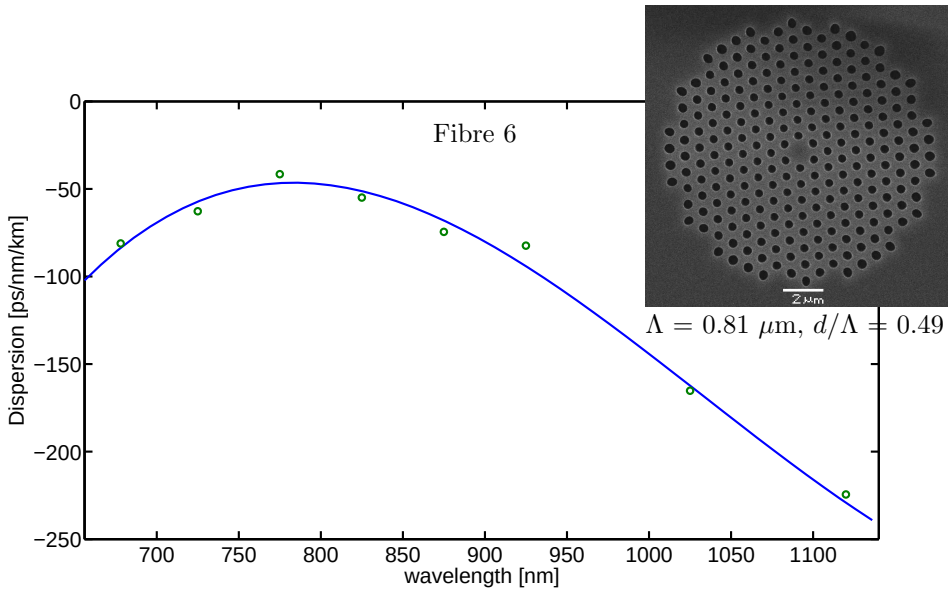

Figure 3-16: Top: measured dispersion of "Fibre 6", from the first two fibre draws done using the stack designed for 800 nm. Bottom: Scanning electron microscope image of Fibre 6, with 2 μm scale bar

3 in figure 3-17. This PCF is ideal for generating all-normal supercontinuum at 800 nm. It is referred to in the remainder of the thesis as "ND800", and is used in experiments in chapter 6. The dispersion predicted by empirical formula, and the measured dispersions of ND800 and some other PCF fabricated during the same draw are also plotted in figure 3-17. The dispersion of each fibre was measured by Fei Yu. The measured dispersion is again more anomalous than the dispersion predicted by the empirical formula.

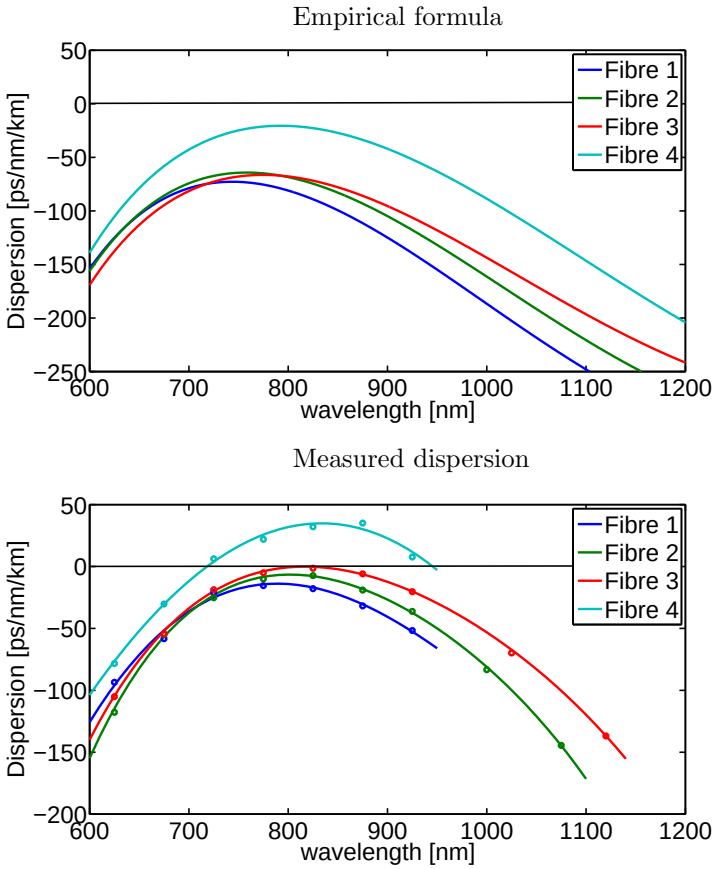

Fibre 1: $\Lambda = 0.88$ μm, $d/\Lambda = 0.52$
Fibre 2: $\Lambda = 0.91$ μm, $d/\Lambda = 0.51$
Fibre 3: $\Lambda = 0.95$ μm, $d/\Lambda = 0.49$
Fibre 4: $\Lambda = 0.95$ μm, $d/\Lambda = 0.55$

Figure 3-17: Empirical dispersion and measured dispersion of 4 different fibres fabricated by Fei Yu and Brian Mangan. The measured dispersion is consistently more anomalous than the empirical formula predicts

3.5 Summary

Traditionally supercontinua are generated in PCF by pumping a fibre with a single ZDW in the anomalous dispersion regime. The generated supercontinuum in this case is sensitive to laser noise, and the supercontinuum can have poor spectral coherence and fluctuating intensity. This is a problem for applications which require high stability and/or high spectral coherence. This problem can be solved by generating supercontinuum in the normal dispersion regime of a PCF. In this chapter two PCFs were fabricated which have all-normal dispersion profiles suitable for generating coherent supercontinua. PCF ND1064 has low dispersion for pumping at 1064 nm, and PCF ND800 has low dispersion for pumping at 800 nm. The measured dispersion and SEM images of both fibres are plotted in figure 3-18.

In subsequent chapters in this thesis, these fibres are used to generate supercontinua, and their useful properties are measured in a number of ways. In Chapter 4, the spectrum from a short length of ND1064 is re-compressed to within a factor of two of its transform limit using linear chirp compensation in a prism compressor, which is testament to the high spectral coherence of the supercontinuum. In Chapter 5, the spectrum from a longer piece of ND1064 is spectrally filtered to create a tunable source of sub-picosecond pulses. In Chapter 6 the coherence of the supercontinuum generated in ND800 pumped using a Ti:Sapphire oscillator is directly measured using an interferometric technique.

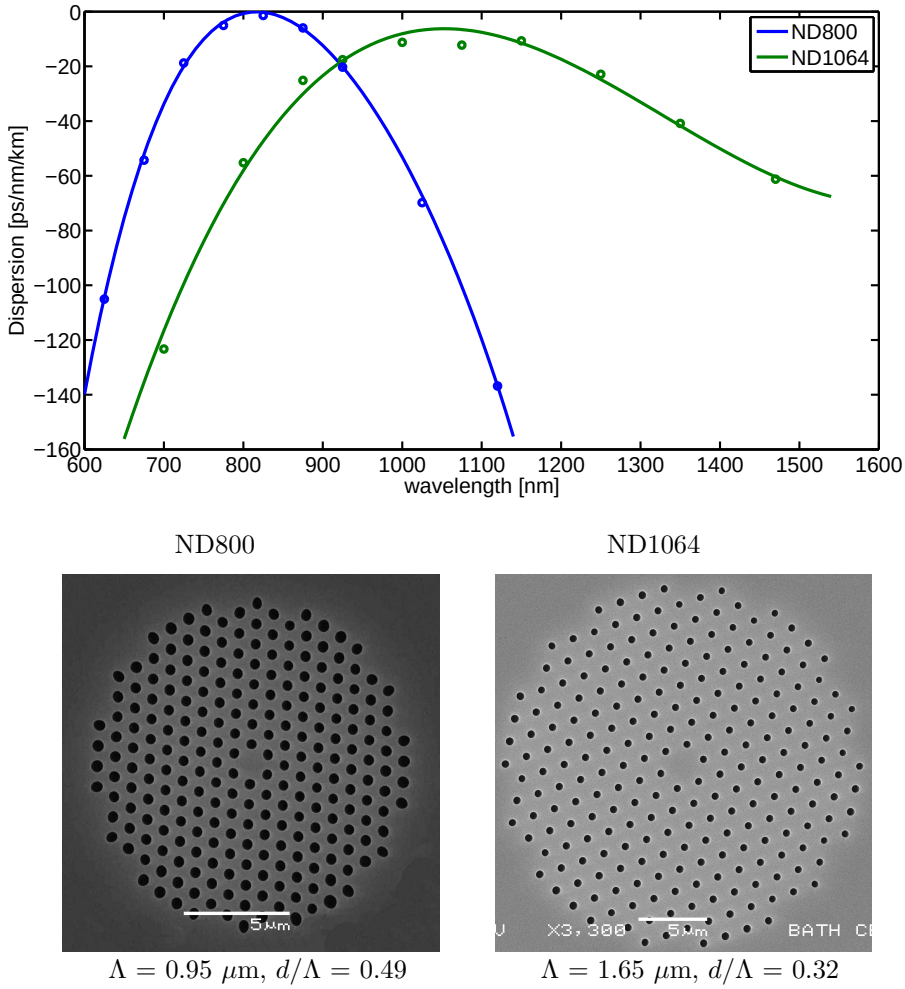

$\Lambda = 0.95$ μm, $d/\Lambda = 0.49$ $\Lambda = 1.65$ μm, $d/\Lambda = 0.32$

Figure 3-18: Measured dispersion and scanning electron microscope images of two all-normal dispersion PCF suitable for the generation of coherent supercontinuum. ND800 has low dispersion at 800 nm for pumping using a Ti:Sapphire laser source, and ND1064 has low dispersion at 1064 nm for pumping with a compact fibre laser. Scale bars on SEMs are both 5 μm

Chapter 4

Pulse re-compression

4.1 Introduction

The re-compressibility of a supercontinuum is dependent on the degree of spectral coherence. This chapter contains results of pulse re-compression of a supercontinuum generated in a short piece of all-normal dispersion fibre ND1064. This is a demonstration of the high spectral coherence, and high shot-to-shot stability of the all-normal dispersion supercontinuum. The experimental results contained in this chapter were published in [64, 88]. The experimental work presented in this chapter was carried out by the author and Peter Mosley. In addition, this chapter contains some numerical simulations performed using the code described in chapter 2. These simulations were carried out by the author alone, and compare the re-compressibility of an anomalous dispersion "white light" supercontinuum with the all-normal dispersion supercontinuum.

Pulse re-compression involves compensating the chirp in a dispersed pulse to obtain a shorter, ideally transform-limited pulse. Linear chirp compensation can be provided by a prism pair compressor [97], a grating pair compressor, chirped mirrors or an optical fibre with flat dispersion. Higher order chirp compensation requires a more complicated compression method, most commonly in the form of a spatial light modulator (SLM). The pulses to be re-compressed are spatially dispersed onto an array of liquid crystal pixels, which can be electronically controlled to vary the phase change induced by each one. Thus it is able to apply a complex phase modulation to the spectrum.

Ultra-short femtosecond pulses are essential for measuring events which happen on a femtosecond time scale, such as chemical reactions [98]. Ultra-short pulses are also important for micro-machining [99], broad-band frequency comb generation [67] and high harmonic generation [100].

Supercontinuum re-compression is an important candidate for the generation of ultra-short pulses. Laser pulse bandwidths are limited by the gain bandwidth of the crystal or doped fibre being used. To create shorter pulses the pulse spectrum must be broadened and the resulting chirp compensated in order to re-compress the pulse. However, even though the

spectra generated using PCF with anomalous dispersion at the pump wavelength can be ultra-broadband and with a transform limit of a few femtoseconds, pulse durations approaching the transform limit are difficult to achieve due to some significant practical limitations [62, 63, 101]. In anomalous dispersion supercontinua, the spectral phase is generally complex with a fine structure and a nonlinear chirp, so re-compression usually requires the use of a SLM. Also, as demonstrated in simulations in chapter 3, the spectral phase of an anomalous dispersion supercontinuum changes from shot to shot. This is a result of the sensitivity of the soliton break-up process to laser noise. In order to fully re-compress the pulse train, the phase applied by the SLM would need to adapt from one pulse to the next. This is not possible using the current technology at typical MHz laser repetition rates. Secondly, the spectral phase has a fine structure. Current state of the art SLMs have around 640 pixels over a bandwidth of 600 nm. This gives a spectral resolution of just less than 1 nm, which is larger than the fine features found in the spectral phase.

Ultra-short pulse compression using anomalous dispersion PCF can be improved by limiting the fibre length such that solitons do not break up and introduce intensity noise. The final pulse duration is thus limited by the bandwidth achievable in the fibre length [63, 101]. The all-normal dispersion supercontinuum does not suffer from these limitations. The high shot to shot coherence means that the relative phase is stable from pulse to pulse. In addition to this, for a short piece of fibre the spectrum generated is for the most part linearly chirped. These special properties of the all-normal dispersion supercontinuum have allowed re-compression to within a factor of two of the transform limit, using only linear chirp compensation. The supercontinuum generated in a longer length of all-normal dispersion PCF is not linearly chirped due to higher order dispersion, but the phase structure is relatively smooth so compression could be achieved using a SLM.

After the results presented in this chapter were published, re-compression of a normal dispersion supercontinuum was achieved by another group [59]. 1.7 mm of all-normal dispersion fibre was pumped with 15 fs Ti:Sapphire input pulses, and a compression ratio of 3 was achieved using linear chirp compensation. With such short input pulses, the coherence would be good for any PCF. The reason for using all-normal dispersion fibre in this case is the linear chirp of the generated supercontinuum. Later, using 6 fs Ti:Sapphire pulses in a longer section of fibre a 3.6 fs pulse was achieved, by employing an active phase shaping technique [94]. These studies concentrated purely on achieving the shortest possible pulses, demonstrating the linear chirp of the supercontinuum. They did not demonstrate the high stability of supercontinua generated in all-normal dispersion fibres. The results in this chapter demonstrate that all-normal dispersion fibre supercontinuum generated using 400 fs pump pulses from a relatively inexpensive compact fibre laser source can be re-compressed by a ratio of 16 using only linear chirp compensation. This would be impossible using an anomalous dispersion supercontinuum PCF.

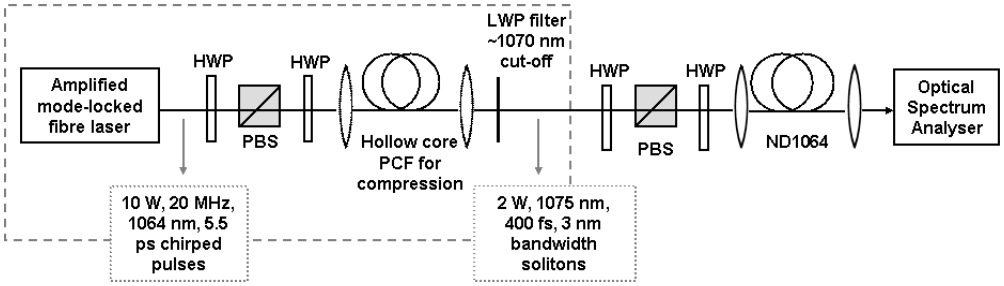

Figure 4-1: Experimental set up for generating supercontinuum in ND1064 using soliton-compressed pulses. HWP, half wave plate; PBS, polarizing beam splitter; LWP, Long-wave-pass filter

4.2 Supercontinuum generation

4.2.1 Soliton-compressed fibre laser source

To generate the supercontinuum a compact amplified mode-locked fibre laser (Fianium Ltd) was used. This laser emits pulses centred at 1064 nm, with a repetition rate of 20 MHz and 10 W average power. The pulses from the seed oscillator are 5.5 ps in duration assuming a Gaussian profile. These undergo SPM in the fibre amplifier, resulting in pulses with a bandwidth of 14 nm and strong normal chirp. To obtain shorter, approximately transform limited pulses for generating supercontinuua, the laser pulses are re-compressed using soliton compression in hollow core PCF (HC-PCF) [102]. During the first stage of propagation in the HC-PCF the pulse is linearly compressed due to anomalous dispersion. In the second stage of propagation a soliton is formed which is shifted to longer wavelengths by soliton self frequency shift (SSFS). The pulses from the fibre laser were launched into a seven-cell HC-PCF with 40% efficiency including coupling losses and attenuation in the fibre. The pulse power was controlled using a half-waveplate followed by a polarising beamsplitter, and a second half-waveplate was used to adjust the polarization axis at the fibre input. The compressed solitons Raman shifted to between 1075 and 1080 nm, depending on the input coupling conditions. Some of the energy which was not converted into the soliton propagated as a dispersive wave. This was removed after the HC-PCF with a long-wave-pass filter with cut-off at around 1070 nm. The cut-off wavelength could be tuned by adjusting the angle of the filter, so the dispersive wave could be completely removed. After the filter the average power was approximately 2 W. The resulting pulses were almost transform limited, with a duration between 350 and 450 fs FWHM (assuming sech^2 profile), depending on the input coupling conditions of the HC-PCF.

The set up is represented in figure 4-1. The spectrum of the laser, and an example of the soliton spectrum after compression in the HC-PCF before and after filtering are plotted in figure 4-2.

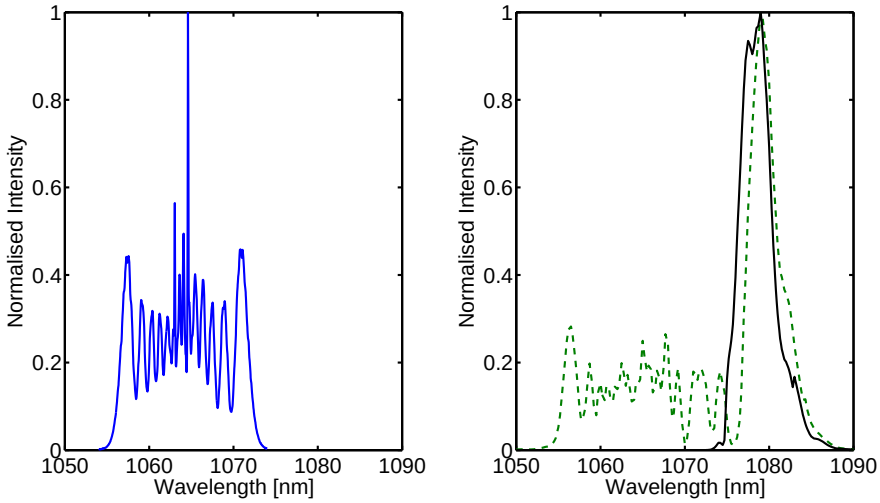

Figure 4-2: Left: Spectrum from fibre laser before soliton compression. The spectrum is characteristic of self phase modulation undergone by the pulses in the amplifier. Right: Spectrum after soliton compression in hollow-core photonic crystal fibre, before filtering the dispersive wave (dashed) and after filtering the dispersive wave (solid)

4.2.2 Supercontinuum generation

Length evolution

The compressed pulses from the HC-PCF were used to create supercontinuum in ND1064. In this case the soliton was centred at 1075 nm. Although the available input power was around 2 W, input powers above around 800 mW damaged the fibre input face. The power was attenuated to 800 mW using a half wave plate and polarising beam splitter, and the light was coupled into the fibre with an efficiency of 50%. The supercontinuum pulses were coupled into a multi-mode fibre cable for delivery to the optical spectrum analyser (OSA) (Ando AO-63158). The spectrum was recorded for different fibre lengths, and the results are plotted in figure 4-3. After 5 cm of propagation the generated supercontinuum spans approximately 250 nm and is symmetrical with evenly spaced peaks which are characteristic of SPM. After 10 cm propagation the SPM shape becomes disrupted, and peaks form at the edges of the spectrum. This is due to optical wave breaking, which is discussed later in this section. After 43 cm the spectrum is smooth and flat, spanning 700 nm. On the linear scale plot, the 43 cm spectrum is more intense on the long wavelength side as a result of the coupling into the multi-mode fibre cable. The spectrum did not change significantly with further propagation.

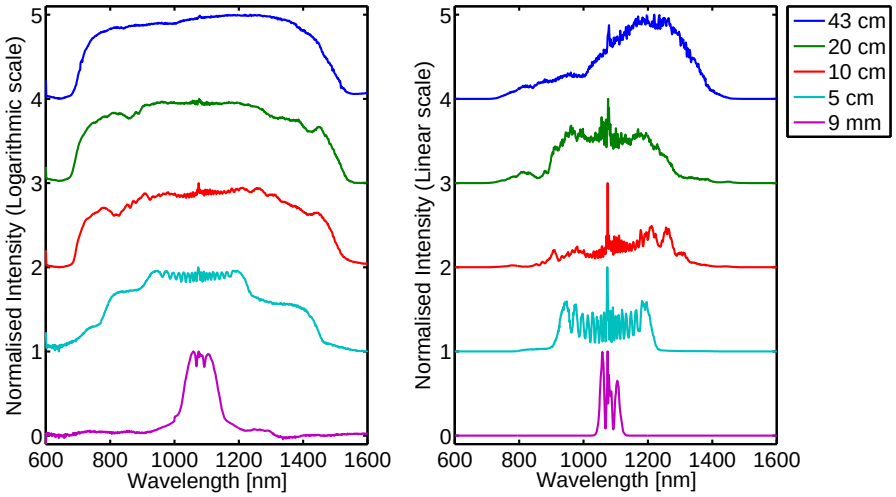

Figure 4-3: Evolution of generated supercontinuum with length in ND1064 PCF pumped with soliton-compressed fibre laser source. Pump pulses were centred at 1075 nm, with FWHM approximately 400 fs and average output power 400 mW at a repetition rate of 20 MHz. The spectra are plotted on a logarithmic scale (left) and a linear scale (right). Each spectrum is offset from the spectrum below by 1 normalised intensity unit

Short fibre length - self phase modulation

The supercontinuum generated in 4 cm of ND1064 using the soliton-compressed fibre laser source has a characteristic SPM shape and a spectral width of approximately 200 nm FWHM, and is plotted in figure 4-4 (a). This spectrum was generated using pulses centred at 1080 nm, with an average output power of 300 mW. For comparison a supercontinuum was generated in 4 cm of a standard single-mode step-index fibre (Nufern, 980HP), using the same pump pulses. The spectrum is plotted in figure 4-4 (b), which also displays characteristic SPM. However, for the same input pulses the generated bandwidth is much narrower, spanning approximately 50 nm. This is because the fibre has high value of normal dispersion (approximately -45 ps/nm/km) at the pump wavelength. The measured dispersion of both ND1064 and the standard fibre are plotted in figure 4-5. The increased dispersion leads to a longer output pulse, and the increased dispersion slope leads to spectral asymmetry. A supercontinuum was also generated in 4 cm of "white light" supercontinuum PCF [51] with anomalous dispersion at the pump wavelength. The measured dispersion for this fibre is also plotted in figure 4-5. The supercontinuum spectrum is plotted in figure 4-4 (c). The dominant broadening mechanism is soliton fission, which is expected for anomalous dispersion supercontinua, and which is evident from the large spectral bandwidth and complex spectral structure. The spectrum in fact spans from 600 nm to 1500 nm, but it is plotted over a narrower scale to allow comparison with the spectra in (a) and (b). The spectrum was recorded using an optical spectrum analyser (OSA) and hence represents an average spectrum over thousands of pump laser pulses.

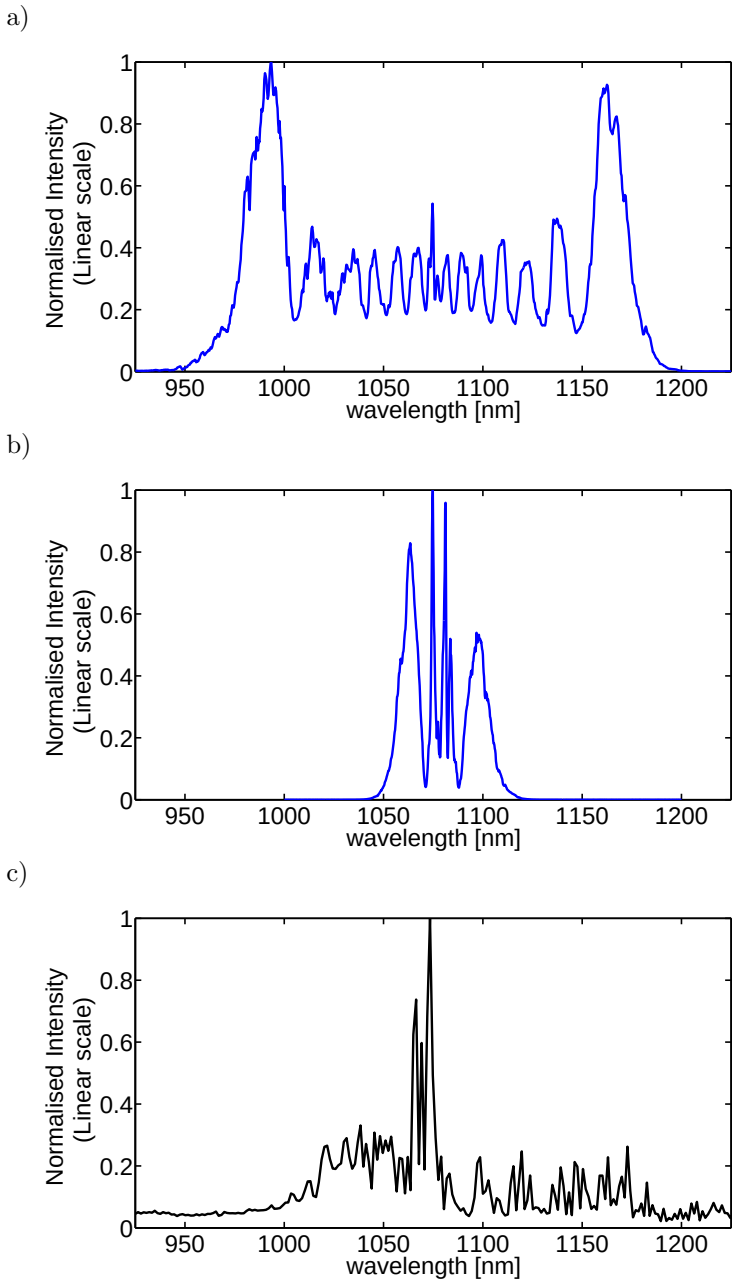

Figure 4-4: Measured supercontinua generated with soliton-compressed pulses centred at 1080 nm, with 400 fs FWHM and 300 mW average output power at 20 MHz repetition rate. Fibres are (a) 4 cm ND1064, (b) 4 cm conventional single mode fibre (Nufern, 980HP), (c) 4 cm anomalous dispersion PCF [51]

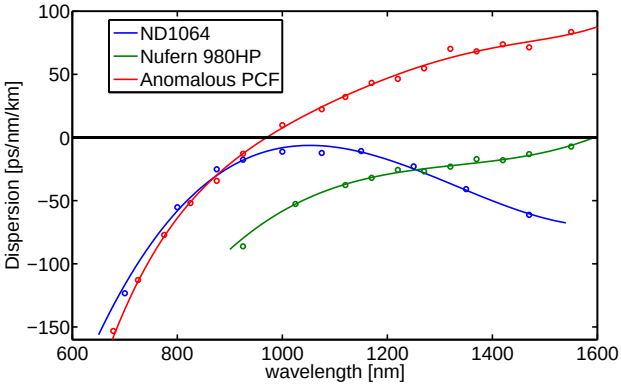

Figure 4-5: Measured dispersion of ND1064, conventional single mode fibre (Nufern, 980HP), and anomalous dispersion PCF [51]

The supercontinuum spectrum generated in 4 cm of ND1064 is convenient for comparing with simulations, because of the regular peaked structure. To obtain some insight into the broadening mechanisms involved in the generation of the supercontinuum, simulations were carried out using the GNLSE code described in chapter 2. The input pulses used in the simulation had a sech^2 profile centred at 1080 nm and with 300 mW average output power, to match the experimental conditions. The pulse FWHM, 350 fs, was optimised to give the best agreement with measured data when dispersion and all nonlinear effects were included. The dispersion of ND1064 over the full simulation window was generated using the empirical formula, with the fibre parameters optimised to produce a dispersion curve which fit closely to the measured dispersion data. The mode field diameter at the pump wavelength was 2.8 μm, calculated using CUDOS. Using $\tau_{\text{shock}} = 1/\omega_0$ produced good agreement with measured spectra, so the wavelength-dependence of the effective mode area was not considered significant.

The results are plotted in figure 4-6. The spectrum generated by SPM only in (a) extends further on the long wavelength side than the measured spectrum. When the fibre dispersion is included in (b), the simulated spectral bandwidth is close to the measured bandwidth, but shifted to longer wavelengths. In (c) the inclusion of self steepening produces a spectrum very similar to the measured spectrum. Raman effects are included in (d), and they do not have a significant effect on the final spectrum. The conclusion is therefore that SPM, dispersion and self steepening all have an impact on the spectral broadening in the short fibre length, but Raman effects have a negligible impact.

a) SPM, no dispersion

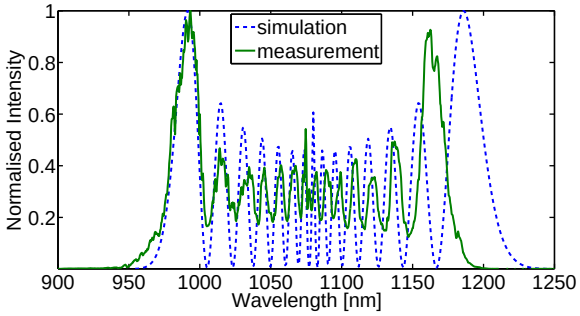

b) SPM and ND1064 dispersion

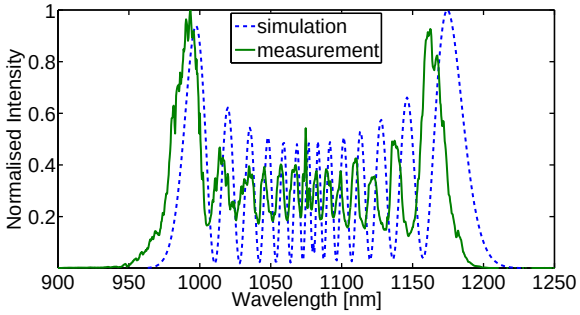

c) SPM, ND1064 dispersion and self-steepening

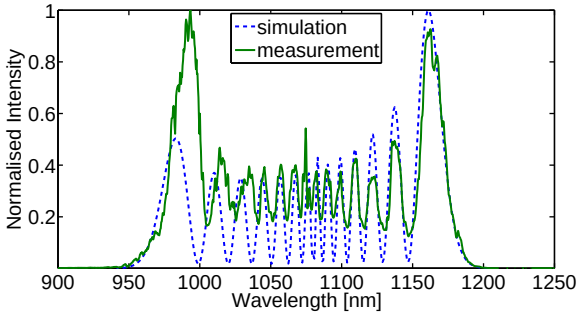

d) SPM, ND1064 dispersion, self-steepening and Raman scattering

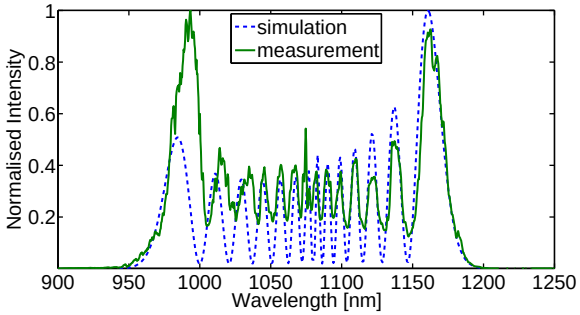

Figure 4-6: Simulated spectra compared with measured spectrum generated in 4 cm ND1064 using soliton compressed source. Nonlinear effects and dispersion are introduced to the simulation individually to show the significance of SPM, dispersion, self steepening and Raman scattering on the final spectrum. All are significant except for Raman scattering

Long fibre length - optical wave breaking

The initial stage of spectral broadening in ND1064 is a result of SPM. After further propagation, optical wave breaking (OWB) occurs, which causes the SPM modulations to flatten and side lobes to appear in the spectrum. OWB is the result of the steepening of the temporal pulse edges, and only occurs under normal dispersion conditions. In the normal dispersion regime, the higher frequencies generated at the steepest part of the pulse trailing edge have a lower group velocity than the tail on the trailing edge, which contains the pump frequencies. The newly generated frequencies are delayed with respect to the pulse tail. The edge thus becomes steeper, until at some point it approaches infinity and the tail "catches up" with the newly generated frequencies, and they interfere. This can also happen at the leading edge of the pulse, where the newly generated frequencies have a higher group velocity than the pulse tail. If a pump frequency in the tail is ω_1 and a newly generated frequency is ω_2 then light is generated at new frequencies $2\omega_1 - \omega_2$ and $2\omega_2 - \omega_1$ [12]. This can therefore be considered a FWM process. A broad side-band is generated in the spectrum, which manifests as fast oscillations at the edges of the pulse envelope in the time domain.

Figure 4-7 contains spectrograms simulated using the GNLSE code described in chapter 2, of the supercontinuum generated in increasing lengths of ND1064. The input pulse parameters are the same as those used for simulations in the previous section. In figure 4-7 (a), after 4 cm propagation the supercontinuum has been broadened by SPM only, and has an "S" shaped spectrogram. As discussed in chapter 2, each frequency in the spectrum occupies two temporal positions, and this is the origin of the modulations in the spectrum. In figure 4-7 (b), after 10 cm propagation the trailing pulse edge has steepened and the tail frequencies overlap with the high frequency components of the spectrum. This is OWB. A side band is generated on the short wavelength edge of the spectrum. OWB occurs on the short wavelength side first due to self steepening. In figure 4-7 (c), after 15 cm propagation OWB occurs on the long wavelength side of the spectrum, and there is a continual transfer of energy from the pulse tails into the spectral side-bands. In figure 4-7 (d), after 25 cm propagation, the pulse tails are depleted. There is no further spectral broadening for longer fibre lengths, only spreading in the time domain due to dispersion.

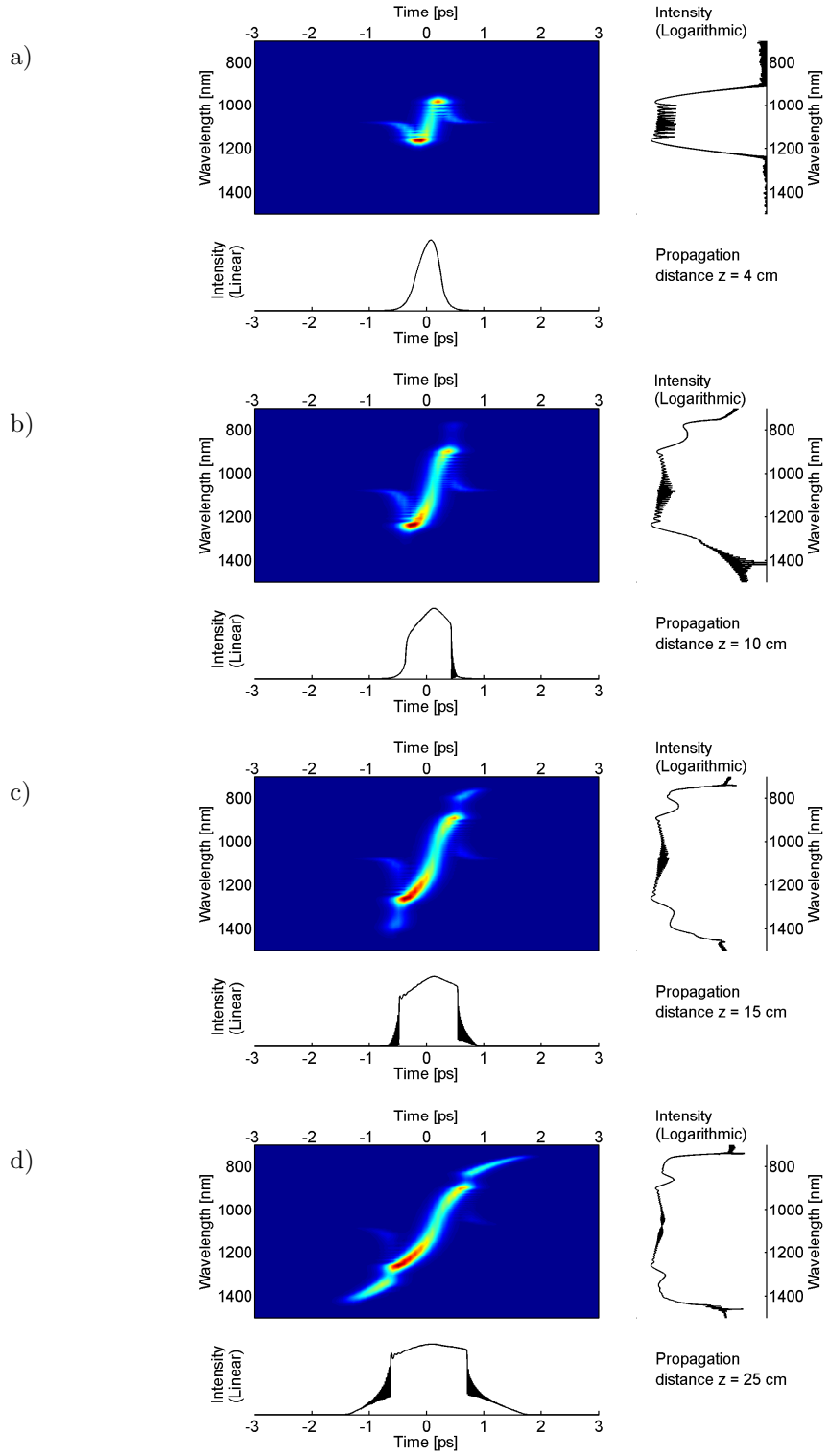

Figure 4-7: Simulated spectrograms for all-normal dispersion fibre supercontinuum generated in different lengths of ND1064, pumped using 350 fs FWHM sech^2 pulses centred at 1080 nm, with 300 mW average power at 20 MHz repetition rate. The onset of optical wave breaking can be seen in b) on the short wavelength side, and in c) on the long wavelength side of the spectrum

4.3 Pulse re-compression

4.3.1 Experiment

The experimental set up is represented in figure 4-8. 4 cm of ND1064 was used to generate a supercontinuum with an approximately linear chirp, to be re-compressed using a simple linear compressor. To re-compress the pulse, the beam was passed through a double-pass SF11 prism pair compressor [97]. The geometry of the prism compressor allows it to have anomalous dispersion, even though the prism material dispersion is normal over the bandwidth of interest. Coarse adjustment of the prism compressor dispersion was done by changing the distance between the prisms. Fine adjustment of the dispersion was achieved by changing the insertion of the second prism into the beam. The return beam from the prism compressor was reflected to a point above the input beam so that it could be collected from above using a D-shaped mirror.

The pulse durations were measured using an interferometric autocorrelator, shown in figure 4-8. The pulse to be measured was split to create two identical versions of the same pulse, which were then delayed with respect to one another. This was done in a Michelson interferometer with one fixed arm and one arm with a variable delay, consisting of a mirror mounted on an audio speaker. A glass microscope slide was used as a beam-splitter. The light from both arms was incident on a light-emitting diode (LED) which was polished back for use as a two-photon detector [103]. It was confirmed experimentally that the LED exhibited two-photon absorption across the full bandwidth of the pulses being measured, with low spectral dependence. The signal produced by the two-photon detector was measured as a function of delay. The signal was proportional to the square of the incident intensity, given by

$$I_{\mathrm{ac}}(\tau) = \int_{-\infty}^{\infty} (|E(t) + E(t+\tau)|^2)^2 dt \tag{4.1}$$

where τ is the delay between pulses.

The maximum fringe intensity should be eight times the background intensity for the data to reflect accurately the temporal pulse structure. The FWHM of the autocorrelation trace is longer than the pulse optical FWHM by a deconvolution factor which depends on the pulse shape. The deconvolution factor for a sech^2 pulse shape is 1.543, and for a Gaussian pulse shape is $\sqrt{2}$ [28].

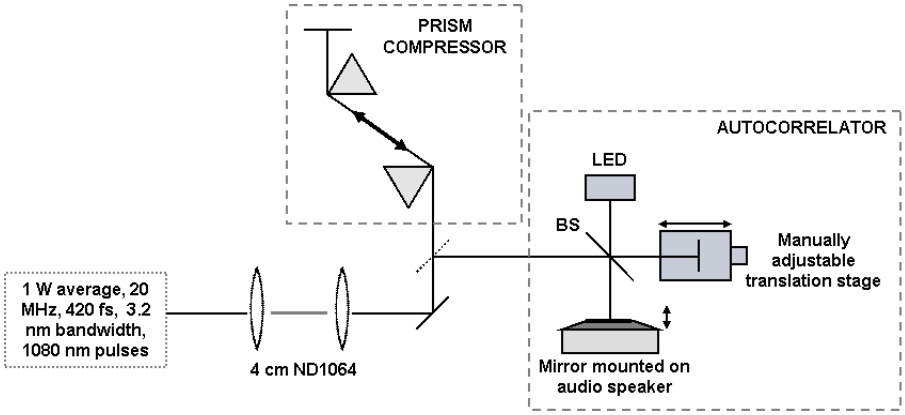

Figure 4-8: Set up for re-compression and autocorrelation measurements of supercontinuum pulses generated in 4 cm ND1064. BS, beam-splitter (glass microscope slide); LED, light-emitting diode polished back for use as a two-photon detector

4.3.2 Results

Autocorrelation traces obtained at different stages of the experiment are shown in figures 4-9 to 4-12. The first is an autocorrelation trace of the pulses emitted from the HC-PCF, which have an optical pulse FWHM of 420 fs assuming a sech^2 temporal profile. Their bandwidth is 3.2 nm, so they are almost transform limited with a time-bandwidth product of 0.35 (the time bandwidth product for a transform limited sech^2 pulse is 0.315). The autocorrelation trace of the output from 4 cm all-normal dispersion fibre is shown in figure 4-10. This exhibits a typical autocorrelation profile for a highly chirped pulse [41]. The pulse length can be estimated from the width of the pedestal, which has an autocorrelation FWHM of approximately 1 ps. Figure 4-11 shows the re-compressed pulse emerging from the prism pair compressor. The baseline is flat, indicating that the linear chirp has been compensated. The pulse has an optical pulse FWHM of 26 fs assuming a sech^2 temporal profile. The shoulders on the trace are due to the small amount of higher order dispersion in the fibre which cannot be compensated for with the prisms. The re-compressed pulse autocorrelation trace is plotted over a smaller scale in figure 4-12 to show that the interference fringes are fully resolved.

The irregularity of the wings of the autocorrelation traces in figs 4-10 and 4-11 is due to fluctuations in both the laser pulse amplitude and coupling into the HC-PCF and supercontinuum PCF. The fluctuations are fast compared to the time over which the autocorrelation trace is recorded.

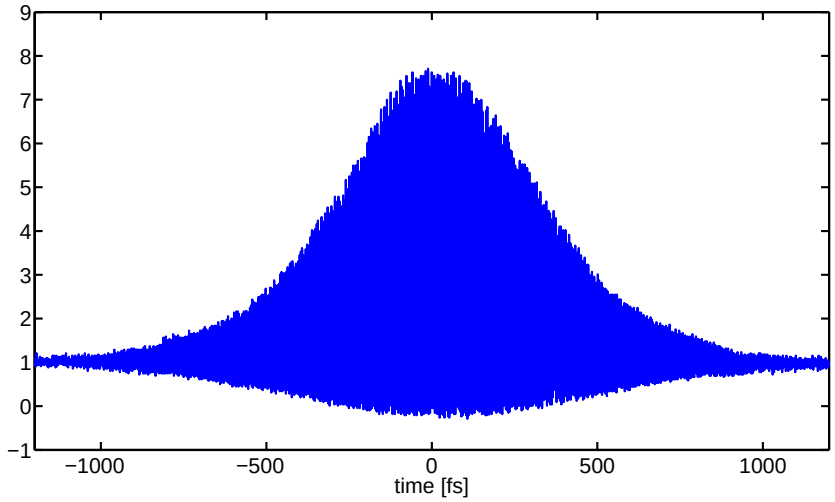

Figure 4-9: Normalised interferometric autocorrelation trace of the pulses at the output of the hollow core photonic crystal fibre. The optical pulse FWHM is 420 fs assuming a sech^2 pulse shape

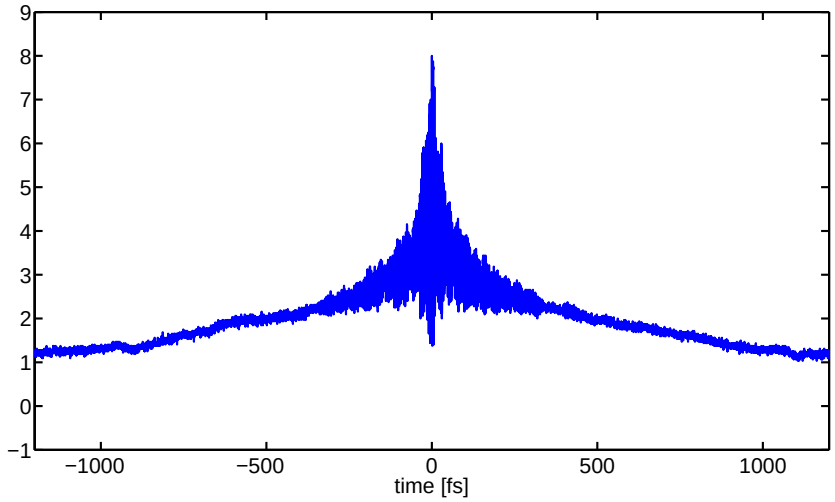

Figure 4-10: Normalised interferometric autocorrelation trace of the supercontinuum pulses generated in 4 cm ND1064. This trace is typical of an autocorrelation of a chirped pulse. An estimation of the pulse length can be obtained from the pedestal, which has an autocorrelation length of approximately 1 ps

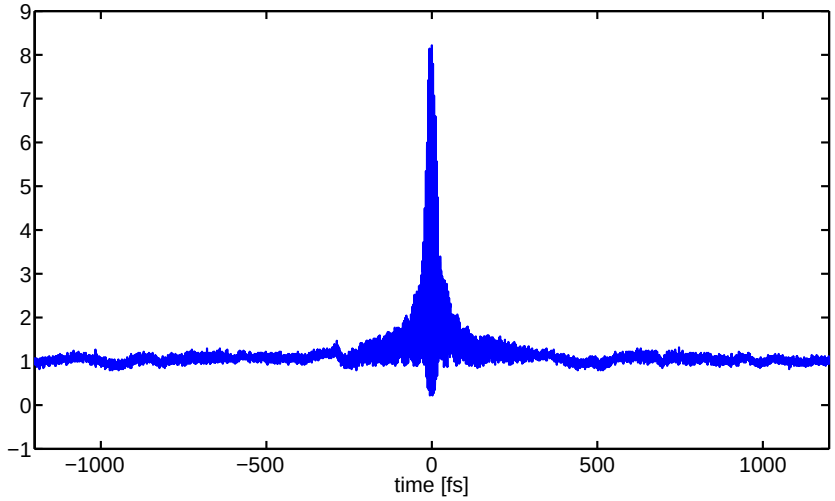

Figure 4-11: Normalised interferometric autocorrelation trace of the supercontinuum pulses generated in 4 cm ND1064, re-compressed using an SF11 prism pair compressor. The optical pulse FWHM is 26 fs, assuming a sech^2 pulse shape. The transform limited optical pulse FWHM is 14 fs

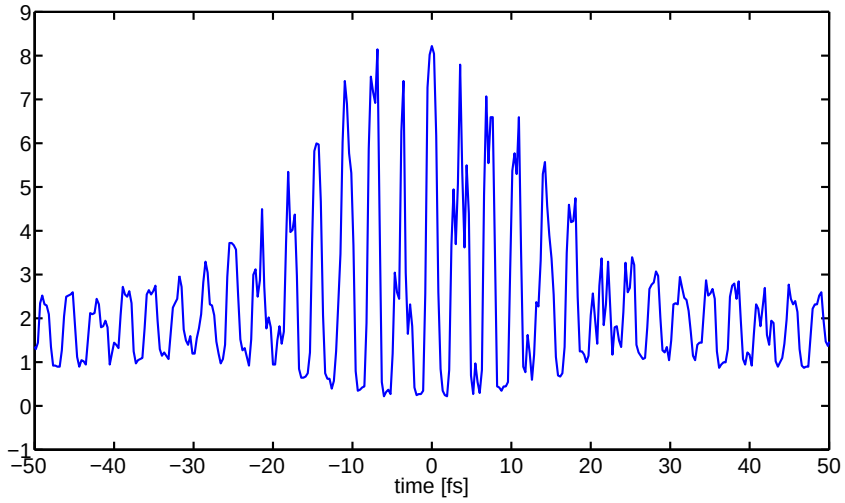

Figure 4-12: Same data plotted in figure 4-11, this time plotted over a narrower range to show fully resolved interference fringes

The transform limit of the measured spectrum, calculated by setting the phase to zero and performing a Fourier transform, is approximately 14 fs. This is shorter than the measured pulse by almost factor of two. The reason for this discrepancy is limitations in the prism alignment method in the experiment. The difference in the insertion of the second prism required to compress a 26 fs pulse to 14 fs is approximately 130 μm. During the experiment the insertion of the second prism was adjusted by sliding the prism manually. Whilst viewing the autocorrelation trace, the position was optimised to obtain the shortest pulse. The accuracy with which the prism can be moved using this method was insufficient to obtain a transform limited pulse. The accuracy of the insertion of the second prism could be improved by mounting it on a micrometer stage.

4.3.3 Simulations

Simulations were carried out to provide insight into the limits of pulse compression for supercontinua. The supercontinuum generated in 4 cm ND1064 was simulated in section 4.2.2, showing good agreement with the measured spectrum. Using the data from this simulation, the transform limited pulse was modelled by setting the spectral phase to zero and taking the Fourier transform. The simulated temporal profile was transformed into an intensity autocorrelation trace, shown in figure 4-13. An intensity autocorrelation FWHM is the same as an interferometric autocorrelation FWHM for a given pulse. In an intensity autocorrelation measurement the electric fields do not interfere, and the autocorrelation trace is proportional to the product of the pulse intensities. It is therefore less computationally expensive to calculate an intensity autocorrelation trace from the simulated data than an interferometric autocorrelation trace, because the complex part of the electric field can be ignored. Intensity autocorrelations are explained in more detail in section 5.2.

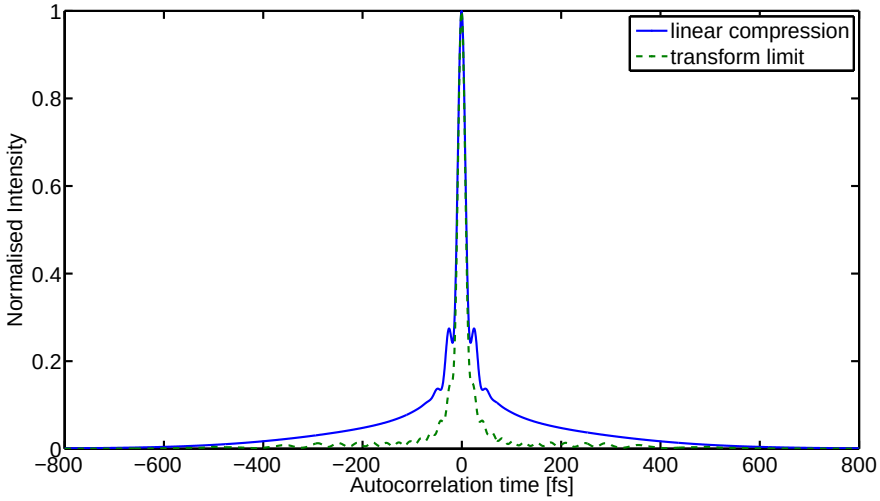

Figure 4-13: Simulated intensity autocorrelation traces of the transform limit, and optimised linear compression of supercontinuum pulses generated in 4 cm ND1064

The simulation data was used to simulate the effect of linear compression on the supercontinuum, also plotted in 4-13. The amount of linear chirp applied was optimised to produce the shortest pulse. Both the transform limited and linearly compressed pulses have a FWHM of 14 fs. The transform limited pulse has shoulders which are a result of the spectral structure. The linearly compressed pulse has larger shoulders, which are a result of both the spectral structure, and the uncompensated higher order dispersion. Spectrograms of the uncompressed and linearly compressed pulses were calculated to illustrate this, and are plotted in figure 4-14. The uncompressed pulse in (a) has linear chirp across the central temporal region of the pulse, and the pulse tails have nonlinear chirp. Therefore when applying linear chirp compensation, the central temporal region of the pulse is compressed, leaving the tails uncompressed, and remaining as shoulders. This can be seen in figure 4-14 (b).

a)

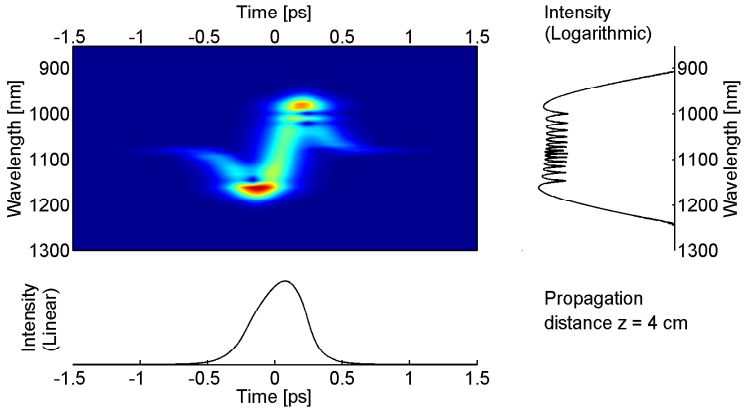

b)

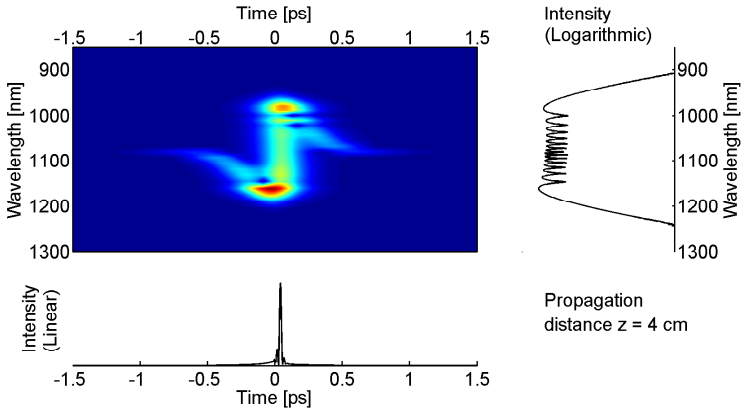

Figure 4-14: Simulated spectrograms of supercontinuum generated in 4 cm ND1064 with a) no re-compression, b) linear chirp compensation optimised to obtain the shortest pulse

Simulations were also carried out for 4 cm of the anomalous dispersion PCF [51] using the same input pulse conditions. A spectrogram of the output is shown in figure 4-15. The pulse is separated into distinct solitons, which are shifted in such a way that no amount of linear chirp compensation can shorten the pulse. In order to compress this spectrum, a SLM would be needed. Also the effect of pump jitter on the spectral phase is significant. The spectral phases of ten individual shots with random quantum noise seeds for both anomalous and normal PCF are plotted in figure 4-16. The spectral phase of the anomalous dispersion supercontinuum changes from shot to shot, meaning that to truly compensate the phase a SLM would have to adapt between each shot, which is not possible with current technology. The normal dispersion supercontinuum phase is stable from shot to shot, enabling effective re-compression.

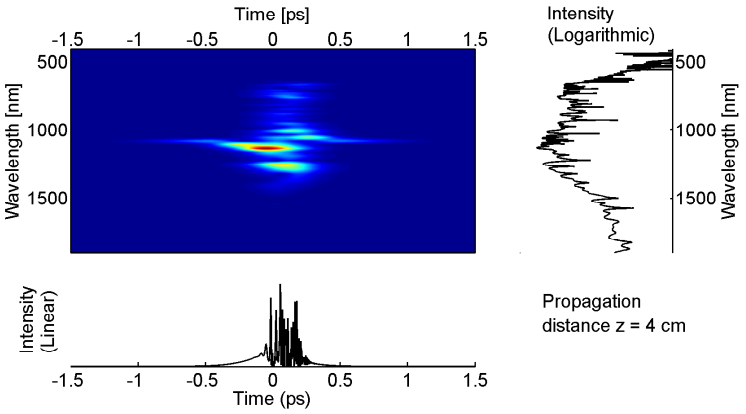

Figure 4-15: Simulated spectrogram showing supercontinuum pulse generated in 4 cm anomalous dispersion fibre. The pulse is split into smaller pulses, and the chirp is complex so it cannot be re-compressed using linear chirp compensation

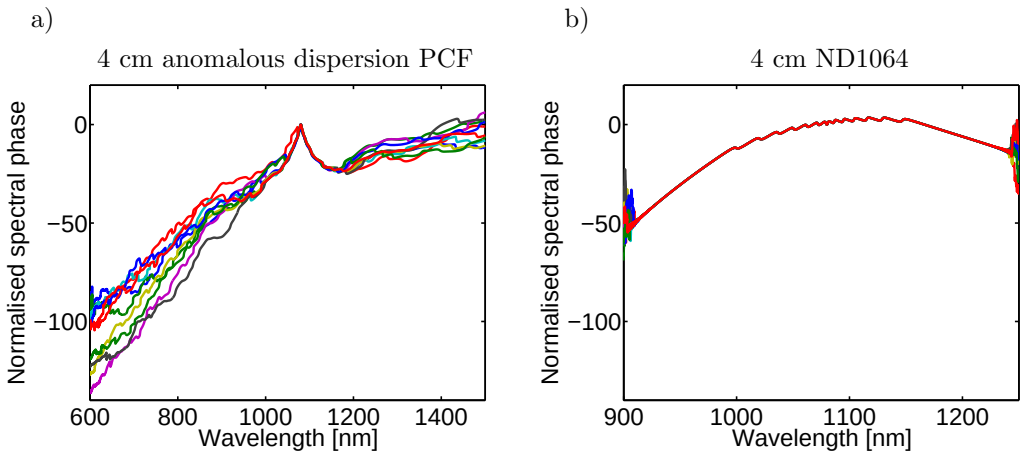

Figure 4-16: Simulated spectral phase of ten independently generated supercontinua with random quantum noise seed, generated in a) 4 cm anomalous dispersion PCF, and b) 4 cm ND1064

To investigate the possibility of linearly compressing a broader supercontinuum generated in a longer piece of all-normal dispersion fibre, the spectrum generated in 25 cm ND1064 was simulated using the same input pulse conditions. The linearly compressed and transform limited simulated intensity autocorrelations are plotted in figure 4-17. The linearly compressed pulse has broader shoulders than the linearly compressed pulse from 4 cm fibre, because there is a larger amount of higher order dispersion accumulated. The nonlinear chirp of the uncompressed supercontinuum pulses can be seen in the spectrogram plotted in 4-18 (a), and the pulse after linear compression is plotted in 4-18 (b). To fully re-compress this pulse, a SLM would be required. Compression using a SLM would not be limited by instability or SLM resolution due to the high spectral coherence and stability, and the smooth spectral structure of the all-normal dispersion supercontinuum.

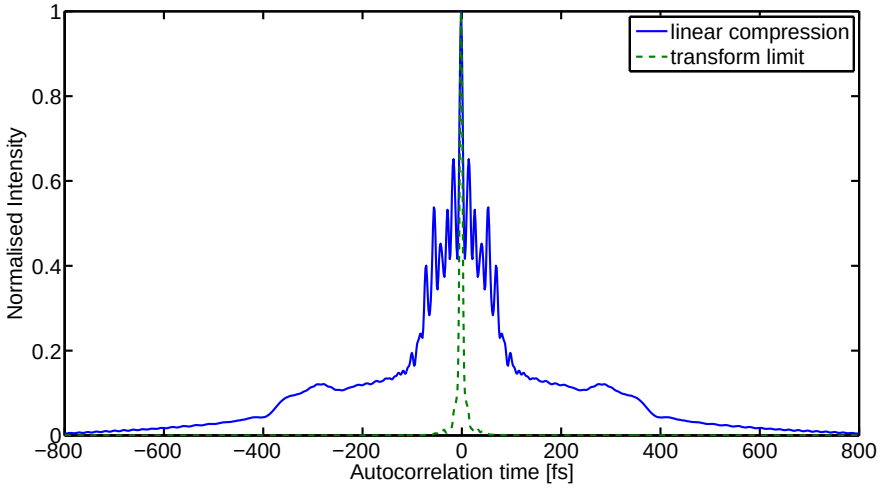

Figure 4-17: Simulated intensity autocorrelation traces of the transform limit, and optimum linear compression of supercontinuum pulses generated in 25 cm ND1064

a)

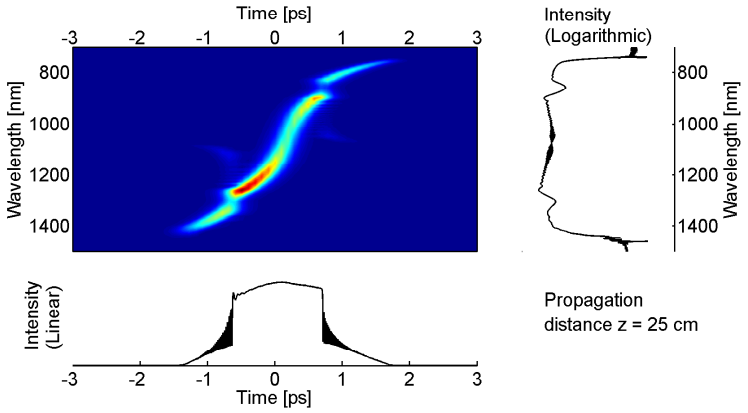

b)

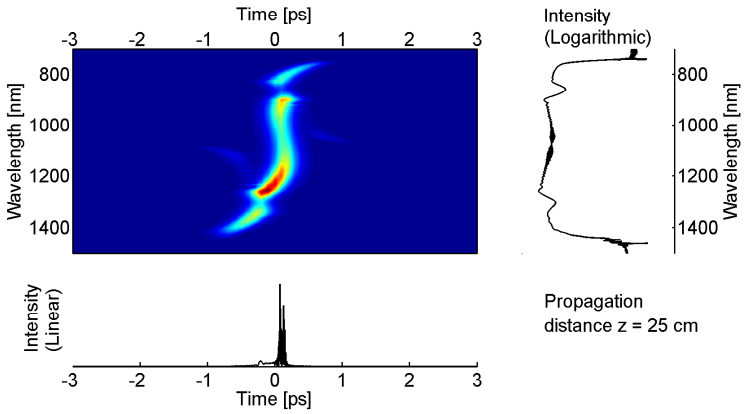

Figure 4-18: Simulated spectrograms of supercontinuum generated in 25 cm ND1064 with a) no re-compression, b) linear chirp compensation optimised to obtain the shortest pulse

4.4 Conclusions and future outlook

The results obtained in this chapter demonstrate that the all-normal dispersion supercontinuum has a high degree of spectral coherence compared with the supercontinuum generated in an equivalent length of anomalous dispersion PCF, for the input pulses used. Supercontinuum pulses with a bandwidth of 200 nm were generated in 4cm of ND1064 PCF using 400 fs FWHM pump pulses centred at 1080 nm. Using linear chirp compensation in a prism pair compressor the supercontinuum pulses were re-compressed to 26 fs FWHM assuming a sech^2 pulse shape. This is within a factor of two of the transform-limited pulse FWHM calculated from the measured spectrum (14 fs). However, simulations showed that the supercontinuum before compression has an almost linear chirp, and therefore using linear compression it should be possible to reach a pulse which is close to the transform limited duration. The discrepancy between the measured and theoretical values is within the estimated error of the experimental

procedure.

Simulations were carried out which demonstrated that supercontinuum pulses generated in the same length of an anomalous dispersion PCF would not be re-compressible using linear chirp compensation. This is due to the complex and nonlinear chirp induced by the spectral broadening mechanisms, and the fibre dispersion. The pulses could be re-compressed using a SLM, but the compression would be limited because of shot-to-shot phase fluctuations and complex spectral structure. Simulations also showed that supercontinuum pulses generated in 25 cm of ND1064 would not be fully re-compressible using linear chirp compensation. They could however be successfully compressed using a SLM, because the spectral phase is stable from shot to shot, and the spectral structure is relatively smooth. Since this work was carried out, a demonstration of re-compression of all-normal dispersion supercontinuum using active phase shaping was published [94]. Almost transform limited pulses were achieved.

The pump pulses used in this study were approximately 400 fs FWHM, much longer than the 15 fs pump pulses used in subsequently published pulse re-compression demonstrations using all-normal dispersion PCF [59, 94]. For such short pump pulses, the spectral coherence of a supercontinuum is likely to be high even for anomalous dispersion pumping. In this case, the advantage of using all-normal dispersion PCF is the near-linear chirp and smooth spectral structure. The research presented in this chapter is unique because it demonstrates the high spectral coherence and stability of the all-normal dispersion supercontinuum. Existing experimental set-ups currently using anomalous dispersion supercontinuum PCF and pump pulses >100 fs may benefit from higher stability by switching to all-normal dispersion PCF, provided the spectral bandwidth is sufficient.

Chapter 5

Coherent widely tunable sub-picosecond laser source

5.1 Introduction

Supercontinuum generated in all-normal dispersion PCF has high coherence and stability, and is therefore an attractive candidate for use as a broadband tunable laser source. In this chapter a tunable, coherent source of sub-picosecond pulses is demonstrated by spectrally filtering the all-normal dispersion supercontinuum. Some of the experimental and simulated results contained in this chapter were published in [65]. The experimental work and simulations were carried out by the author, with some contributions from Peter Mosley.

Tunable ultra-short lasers have applications in spectroscopy and microscopy. Time-resolved pump probe experiments require pump and probe wavelengths to be carefully selected in order to probe resonances within the sample or chemical label being used. These pulses must also be very stable in order to maintain high accuracy and resolution in the measurements.

There are various ways in which to generate tunable ultra-short pulses. Ti:sapphire lasers can allow tuning over hundreds of nanometres in the visible to near infra-red [104]. The spectral range of Ti:sapphire oscillators can be extended using frequency doubling in second harmonic generation crystals, or by pumping an optical parametric oscillator to reach into the mid or far-infra red. A downside of these systems are that they are bulky and not easily transportable.

Nonlinear effects in highly nonlinear fibres can be used to generate tunable sources of ultrashort pulses. One method is to generate solitons, which Raman shift to longer wavelengths. The Raman shift can be varied by changing the input power or polarisation [102, 105]. Octave spanning Raman shifted solitons have recently been achieved in a special low OH fibre [106]. Solitons can also be frequency doubled [107]. However, because the soliton shift is power-dependent, intensity fluctuation of the pump pulses will reduce spectral coherence.

A very simple way to create a tunable source is to generate supercontinuum, and spectrally filter pulses at the desired wavelengths. Tunable sources based on broadband supercontinua

generated in bulk or anomalous dispersion PCF have been used for spectroscopy [55, 77, 108, 109]. However, all of these publications reported limitations due to the amplitude fluctuations of the supercontinuum.

Supercontinua generated in all normal dispersion fibre are coherent, and have stable spectral intensity. The pulses do not have the multi-soliton temporal structure characteristic of anomalously pumped supercontinua. Therefore filtering all-normal dispersion supercontinuum will yield short, clean pulses. This chapter contains a comparison of the pulses obtained by spectrally filtering an all-normal dispersion supercontinuum, and an anomalous dispersion supercontinuum.

5.2 Experiment

An amplified mode-locked fibre laser (Fianium Ltd) emits chirped pulses with 5.5 ps duration assuming a Gaussian pulse profile, with a repetition rate of 20 MHz and average power 10 W. This is the same laser used in chapter 4. For this experiment, the chirped pulses from the laser were compressed to 200 fs FWHM assuming a sech^2 pulse shape using a transmission grating pair compressor as described in [110]. The experimental set up is shown in figure 5-1. The grating compressor consists of a pair of blazed transmission diffraction gratings, fabricated from fused silica with 1250 lines/mm. The grating separation can be adjusted to tune the dispersion of the compressor. The return beam is directed above the input beam, and is collected using a flat D-shaped pick-off mirror. The straight edge of the mirror extends to the edge of the mount, allowing it to separate closely spaced beams.

Autocorrelation measurements in this chapter were performed using an APE PulseCheck commercial intensity autocorrelator. This contains an interferometer with one variable delay arm, and the light from both arms is focused into a second harmonic generation crystal. Each arm is incident on the crystal at an angle, and when the pulses are temporally overlapped the sum frequency signal emerges halfway between these angles. For a background-free measurement the sum frequency signal is isolated using an aperture, and measured using a photo-multiplier tube as a function of delay. No interference fringes can be seen because the pulse electric fields do not interfere; only their intensities are multiplied in the nonlinear crystal. The autocorrelation signal is therefore given by

$$I_{\text{ac}}(\tau) \propto \int_{-\infty}^{\infty} I(t)I(t+\tau)dt \tag{5.1}$$

The chirped pulses from the laser have an optical pulse FWHM of 5.5 ps assuming a Gaussian pulse shape. An intensity autocorrelation of the pulse directly from the laser is plotted in figure 5-2 (a). After passing through the grating pair compressor the optical pulse duration is 200 fs FWHM (assuming a sech^2 profile), an intensity autocorrelation of which is plotted in figure 5-2 (a), and again over a smaller time scale in figure 5-2 (b). For optimum compression the grating separation is approximately 2 cm. After the grating compressor the average power is 6 W. The compressed pulse has shoulders which are due to higher order dispersion in the laser which is

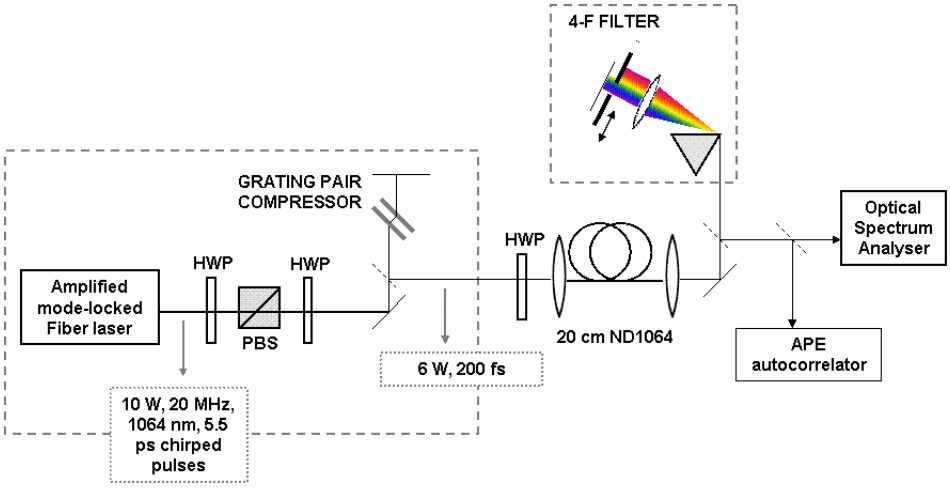

Figure 5-1: Set up for filtering supercontinuum. HWP, half wave plate; PBS, polarising beam splitter. The pulses are delivered to the optical spectrum analyser using a multi-mode fibre cable

not compensated for by the grating pair. The uncompressed part of the pulse was sufficiently long and weak that it did not make a significant contribution to spectral broadening in the supercontinuum PCF.

Two supercontinuum PCFs were tested using the same set up, one was all-normal dispersion PCF with low normal dispersion at the pump wavelength (ND1064) and the other was a supercontinuum PCF with anomalous dispersion at the pump wavelength [51]. The measured dispersion profiles of both fibres are plotted in figure 5-3.

The compressed pulses were coupled into ND1064 with coupling efficiency 50%, giving an average output power of approximately 400 mW. As in the previous chapter, above an input power of around 800 mW the fibre end was damaged. The evolution of the spectrum with length is plotted in figure 5-4. The spectrum in 4 cm of ND1064 has a bandwidth of approximately 600 nm, which is broader than the spectrum generated in 4 cm ND1064 presented in chapter 4 which spanned only 200 nm. This is because here the input pulse duration is shorter (200 fs FWHM) than in chapter 4 (400 fs FWHM), so the peak power is higher despite the average power being the same. For longer fibre lengths, the spectrum continues to broaden, reaching a bandwidth of 800 nm. Most of the spectral structure flattens out, except for a dip on the short wavelength side of the pump. This dip is formed between the SPM-generated central region of the spectrum, and the OWB-generated side-bands. In the previous chapter, simulated spectra in long fibre lengths pumped using 350 fs pulses displayed two dips, one each side of the pump wavelength (figure 4-7). The dip on the short wavelength side is slightly more prominent, due to self steepening. The spectra presented here are generated using shorter pulses, for which self steepening is more significant, resulting in more asymmetric spectra.

The minimum fibre length which produced a supercontinuum with the maximum bandwidth and a smooth spectral profile was approximately 20 cm. After 20 cm of propagation no further

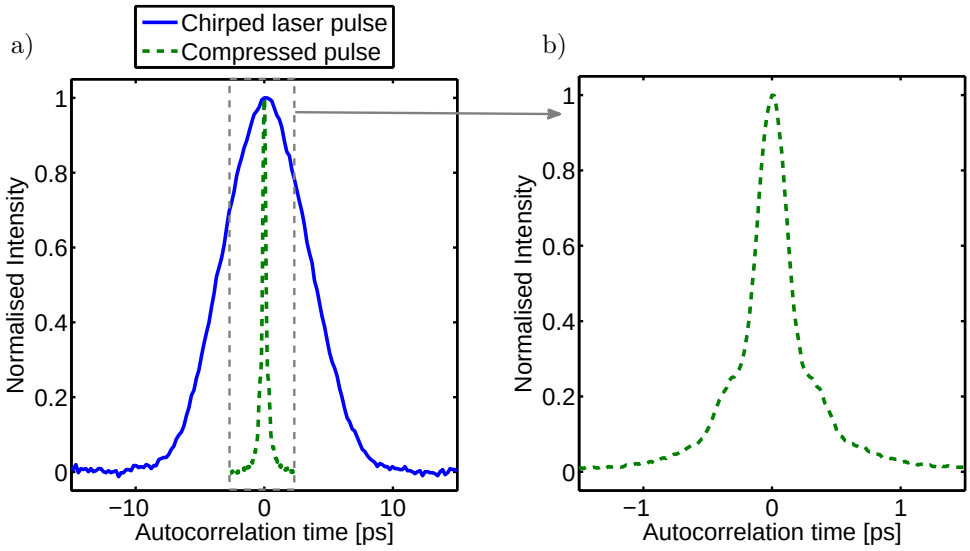

Figure 5-2: a) Intensity autocorrelation measurements of the chirped fibre laser pulse before compression (solid), with a 5.5 ps FWHM duration assuming a Gaussian pulse shape, and the pulse after the grating compressor (dashed), with a 200 fs FWHM duration assuming a sech^2 pulse shape, b) the pulse after the grating compressor, plotted over a narrower range to make shoulders visible

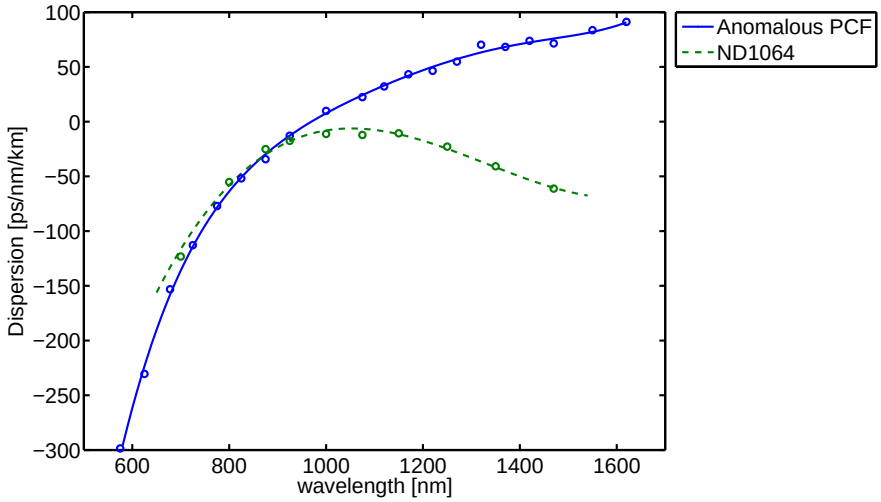

Figure 5-3: Measured dispersion profiles of two supercontinuum fibres tested: an anomalous dispersion PCF [51] and all-normal dispersion PCF, ND1064. Circles show two-point differences measured from group delay data. Lines show derivative of 6th order polynomial fit to the group delay data for anomalous fibre, and 4th order polynomial fit to group delay data for ND1064

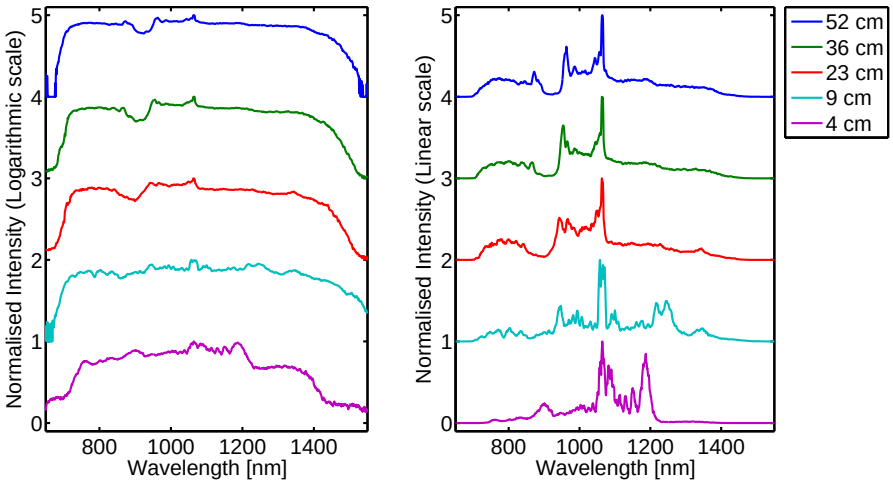

Figure 5-4: Evolution with length of supercontinuum spectra generated in ND1064 pumped with 200 fs FWHM grating compressed pulses, plotted on a logarithmic scale (left) and a linear scale (right). Each spectrum is offset from the spectrum below by one normalised intensity unit

spectral broadening occurs, and further smoothing is negligible. The pulse simply broadens in time, which is undesirable for the production of short pulses when spectrally filtering. Therefore, a 20 cm length of ND1064 was used for the experiment, and the same length of anomalous dispersion PCF was used to enable direct comparison.

For the filtering experiment, the compressed pulses were coupled into the supercontinuum fibre under test, and the generated supercontinuum pulses were filtered using a 4-f filter (see figure 5-1). An SF11 prism provides angular dispersion, a lens is placed one focal length from the prism, and the light is incident on an adjustable slit which is also placed one focal length from the lens (ie. in the Fourier plane). A silver mirror is situated directly behind the adjustable slit. This system has lower loss than a similar system using gratings which has been used to filter supercontinuum in other experiments [55, 105, 108]. Once again the return beam is above the input beam and is collected using a D-shaped mirror. The temporal profile of the filtered supercontinuum "slice" is then analysed using the APE PulseCheck commercial intensity autocorrelator. For each PCF this was done over a range of central wavelengths and bandwidths.

5.3 Results

The spectrum generated in 20 cm of ND1064, with 360 mW average output power, is plotted in figure 5-5 (a). It spans from 700 nm to 1450 nm, so the average spectral power density is approximately 0.5 mW/nm. The spectrum has a characteristic shape of SPM in the central region, and at the spectrum edges there are side bands which are formed through OWB. The spectral intensity profile was observed to be highly dependent on input polarisation. The input

polarisation was set using the half wave plate before the fibre input to produce the broadest spectrum, and was kept constant throughout the experiment. Some examples of the filtered spectra are also plotted in figure 5-5 (a).

a)

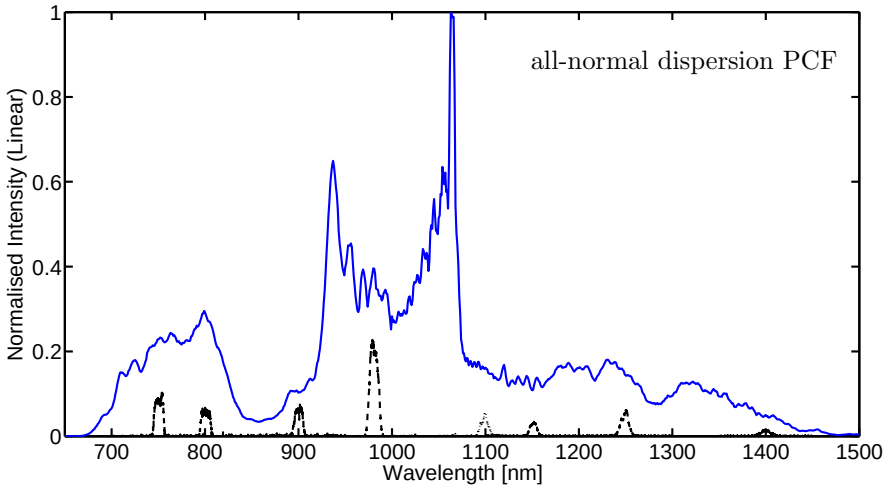

b)

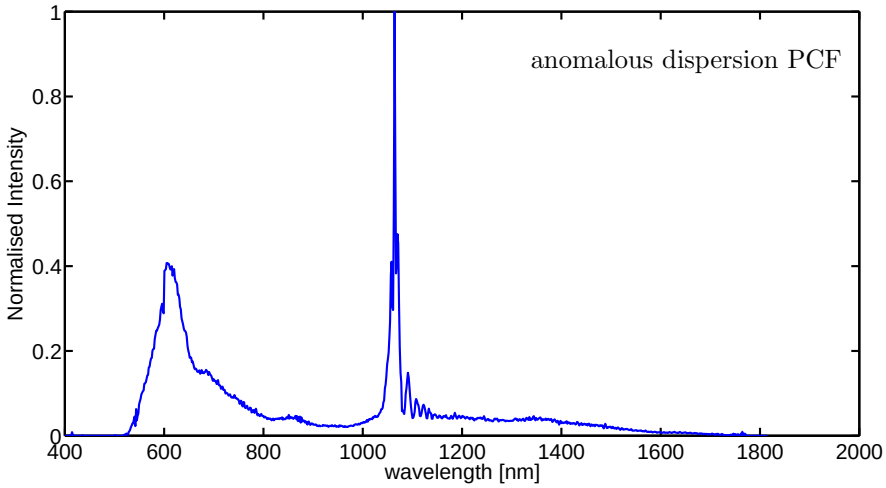

Figure 5-5: Spectra generated using pump pulses centred at 1064 nm with 200 fs FWHM assuming a sech^2 profile with 20 MHz repetition rate in a) 20 cm ND1064 with 360 mW average output power, and b) 20 cm anomalous dispersion PCF, with average output power 650 mW. Dashed lines in a) are examples of filtered spectra

For the anomalous dispersion PCF, the maximum average input power before fibre end damage was 1.2 W, and the average output power was 650 mW. The spectrum generated is plotted in figure 5-5 (b). The spectrum spans 600 to 1700 nm, but the energy is not evenly distributed across the spectrum, with most of the light being in a peak at 600 nm, and at the pump wavelength. The large amount of residual pump on the spectra from both PCFs is the uncompressed part of the pump which does not contribute to spectral broadening.

The supercontinua generated in both PCF were simulated using the GNLSE code described in chapter 2, to study their expected temporal and spectral properties. The input pulse used in the simulation was a 200 fs FWHM sech^2 pulse with average power matching that measured experimentally. All nonlinear effects were included in the simulation. For each PCF, 20 independently generated supercontinua were calculated, with 5% intensity noise added. This is the variation in amplitude of the fibre laser pulses, measured using a fast photodiode and oscilloscope. The simulated supercontinuum temporal profiles and spectra are plotted in figure 5-6. The simulated average spectra are similar to the measured spectra, with the ND1064 spectrum showing many of the same spectral features, and the anomalous dispersion supercontinuum having a peak around 600 nm. In general, both the measured spectra have lower intensity on the long wavelength side than the simulated spectra. This due to variation of coupling efficiency with wavelength into the multi-mode fibre cable used for delivering pulses to the OSA.

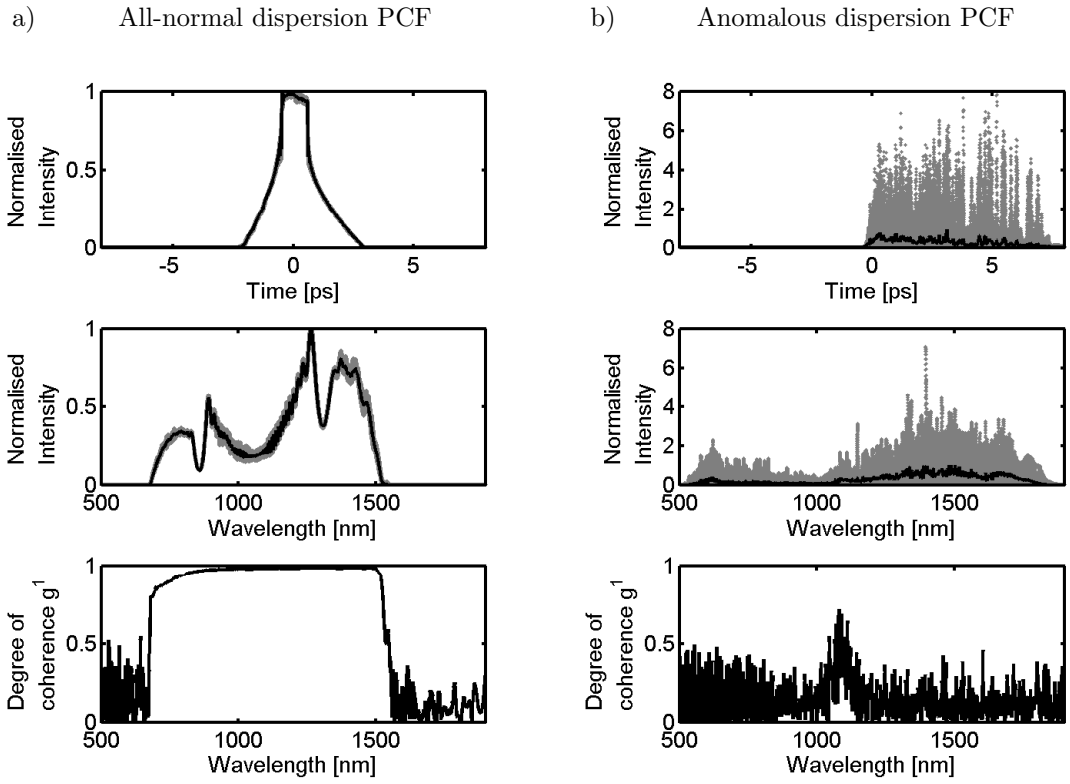

Figure 5-6: Top to bottom: Simulated temporal profiles, spectra and degree of coherence over ensemble of 20 independently generated supercontinua with 5% intensity noise generated in a) 20 cm ND1064 and b) 20 cm anomalous dispersion supercontinuum PCF. Each of the 20 independently generated temporal profiles and spectra are plotted in grey, and the average temporal profiles and spectra are plotted in black

Neither the spectral nor temporal intensity of the simulated all-normal dispersion supercontinuum fluctuates significantly from shot to shot, even with 5% intensity noise on the input

pulses. The anomalous dispersion supercontinuum however shows extremely large fluctuations. The degree of coherence calculated for each supercontinuum reflects this; the anomalous dispersion supercontinuum has no coherence away from the pump wavelength, while the all-normal dispersion supercontinuum has high coherence across the whole spectral bandwidth.

Figure 5-7 shows typical experimentally obtained autocorrelation traces resulting from filtering the two types of supercontinuum. The pulses filtered from the ND1064 supercontinuum were always short, single pulses in the time domain. On the other hand, at most wavelengths the pulses filtered from the anomalous dispersion supercontinuum displayed significant side-peaks, separated from the central peak by several picoseconds. These side-peaks were confirmed to be higher order modes, as the separation between pulses matches that predicted by the modelled higher order mode dispersion of a 4 μm silica strand. The multi-mode property of the anomalous dispersion PCF limits its usefulness as a tunable source. The higher order modes could be spatially filtered, however a large proportion of the initial pulse energy would be lost. For the pulse shown in figure 5-7 (b), approximately 60% of the total pulse energy is contained in the higher order modes. The duration of the fundamental mode pulses are also longer than the pulses obtained by filtering the all-normal dispersion supercontinuum, due to the higher magnitude of dispersion in the anomalous supercontinuum PCF.

a)

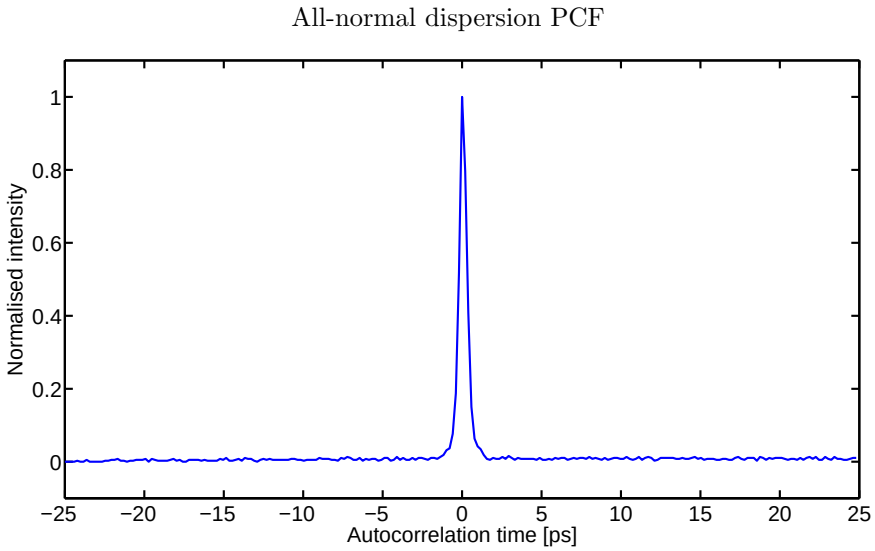

b)

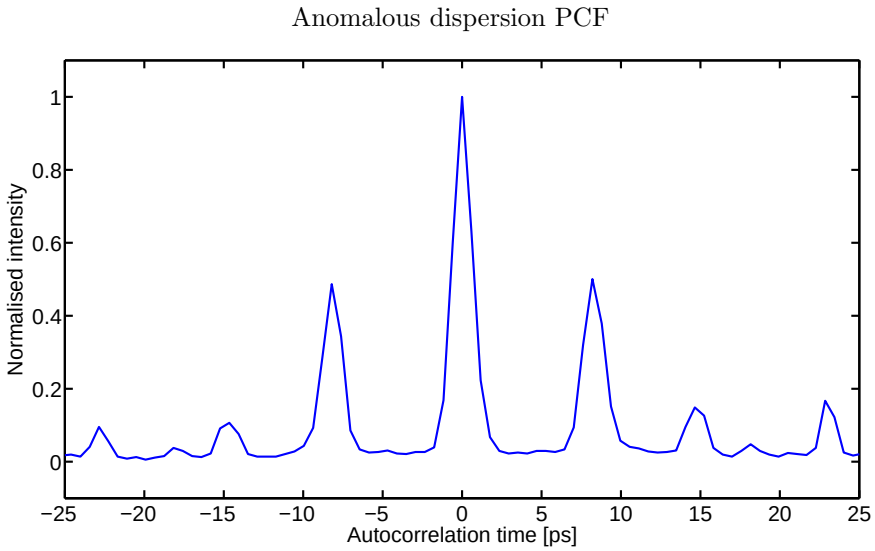

Figure 5-7: Autocorrelation measurement of spectral slices centred at 1100 nm for a) ND1064, with root-mean-square bandwidth 24 nm, 0.7 ps root-mean-square autocorrelation time and b) anomalous dispersion PCF, with root-mean-square bandwidth 22 nm, 1.3 ps root-mean-square autocorrelation time (not including higher order modes)

The measured values of root-mean-square (RMS) autocorrelation time for each spectral slice from the all-normal dispersion supercontinuum are plotted in figure 5-8. The RMS autocorrelation times were calculated based on the definition given in [41], using the following formulae

$$\text{RMS Width } = 2\sqrt{\sigma^2} \tag{5.2}$$

where σ^2 is the second moment of the distribution given by

$$\sigma^2 = \frac{\sum_t (t-\mu)^2 I(t)}{\sum_t I(t)} \tag{5.3}$$

Here t and I represent time and intensity, and μ is the statistical mean. This measure of pulse duration was used because it takes into account the distribution of energy across the pulse. The autocorrelation traces obtained are not well approximated by a sech^2 or Gaussian pulse profiles. The RMS autocorrelation width of the 200 fs FWHM input pulse is 600 fs. To calculate the RMS bandwidth of the spectral slices, t in equation 5.3 was replaced with wavelength.

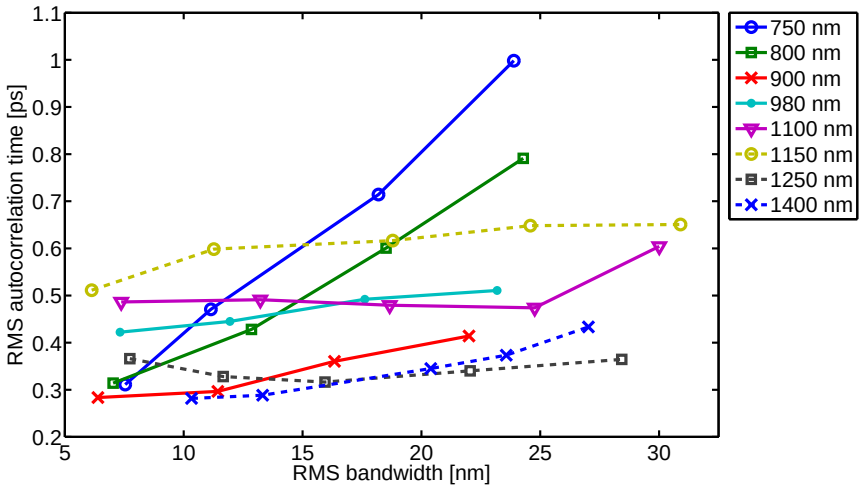

Figure 5-8: Root-mean-square autocorrelation pulse widths of pulses filtered from the all-normal dispersion supercontinuum, and their dependence on central wavelength and root-mean-square spectral bandwidth

The measured autocorrelation times increases with slice bandwidth for all wavelengths except 1250 nm. This suggests that dispersion determines the pulse length, and not the bandwidth. At the short wavelength side of the pump, the shorter the wavelength the higher the dispersion, and the more steep the increase in pulse length with bandwidth. At 1250 nm the autocorrelation time initially decreases with increasing bandwidth, suggesting that for narrow bandwidths the autocorrelation time is determined by the bandwidth rather than by the fibre

dispersion ie. the pulses are transform limited. When filtering at the pump wavelength, the measured pulses had shoulders on them which were several picoseconds in duration, containing the uncompressed part of the pump. The measured RMS autocorrelation times for these are therefore not included in the plot.

The average power in each spectral slice from the all-normal dispersion supercontinuum is plotted in figure 5-9. The slice powers range between 1 mW and 18 mW, and increase with bandwidth as would be expected.

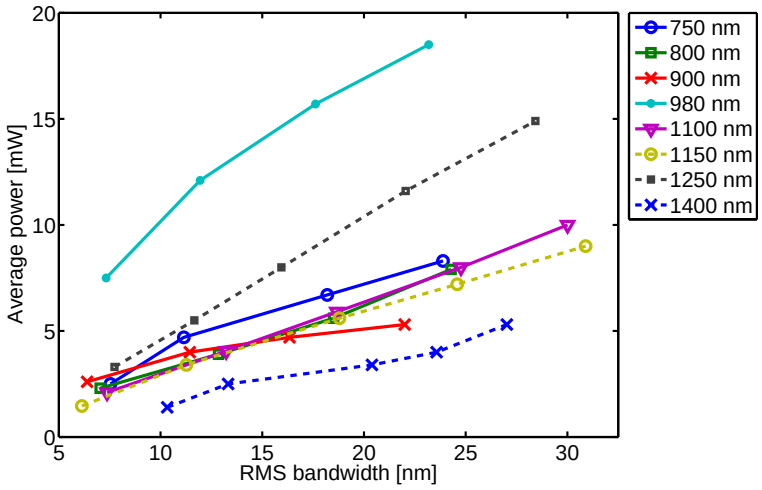

Figure 5-9: Measured average power of pulses filtered from the all-normal dispersion supercontinuum, and their dependence on central wavelength and root-mean-square spectral bandwidth

Intensity autocorrelation measurements were repeated for pulses from both supercontinua over a narrower time range, and higher resolution. The higher resolution allows the shapes of the autocorrelation traces to be studied in more detail. Only the fundamental mode of the pulses filtered from the anomalous dispersion supercontinuum are visible in this range. Autocorrelation traces of pulses obtained by filtering each type of supercontinuum with approximately the same RMS bandwidth (12-13 nm) and central wavelength (1250-1260 nm) are plotted as solid lines in figure 5-10. The anomalous dispersion supercontinuum pulse has significant shoulders on it, which contain the ejected solitons which have been Raman shifted to different wavelengths and therefore dispersed different amounts. The shoulders span almost 2 ps, and contain 52% of the total pulse energy. As a result, the RMS autocorrelation time is 0.90 ps. The all-normal dispersion supercontinuum pulse on the other hand, is clean and short with RMS autocorrelation time 0.33 ps.

Simulated intensity autocorrelation traces were calculated from the spectra plotted in figure 5-6. A Gaussian filter function was applied to each of the twenty independently generated spectra. The Gaussian filter width was optimised to best fit the measured spectrum of the slice. For the all-normal dispersion supercontinuum, a Gaussian filter function with FWHM

20 nm centred at 1250 nm was used, and for the anomalous dispersion simulation a Gaussian filter with FWHM 18 nm centred at 1260 nm was used. The simulated autocorrelation traces are plotted in 5-10, and are the average of the twenty individually calculated autocorrelation traces. For both filtered supercontinua there is a good agreement between the simulated and measured autocorrelation traces.

The autocorrelation traces expected for transform-limited pulses were calculated from the simulated supercontinuum slices, by setting the spectral phase to zero and taking the Fourier transform. These are plotted in figure 5-10. The pulse obtained experimentally from the all-normal dispersion supercontinuum is very close to the calculated transform limited pulse duration. This had been previously suggested by the decrease in pulse duration with increasing bandwidth in figure 5-8, for this wavelength and bandwidth. At the short and long wavelength edges of the spectrum, where the dispersion is high, the filtered pulses are expected to be further from transform limited. The pulse obtained experimentally from the anomalous dispersion supercontinuum is wider than the transform limited pulse. The transform limited autocorrelation trace has low intensity shoulders, which are a result of the complex spectral structure on the pulse. The large shoulders on the measured autocorrelation trace represent the distribution of Raman shifted solitons due to dispersion.

a)

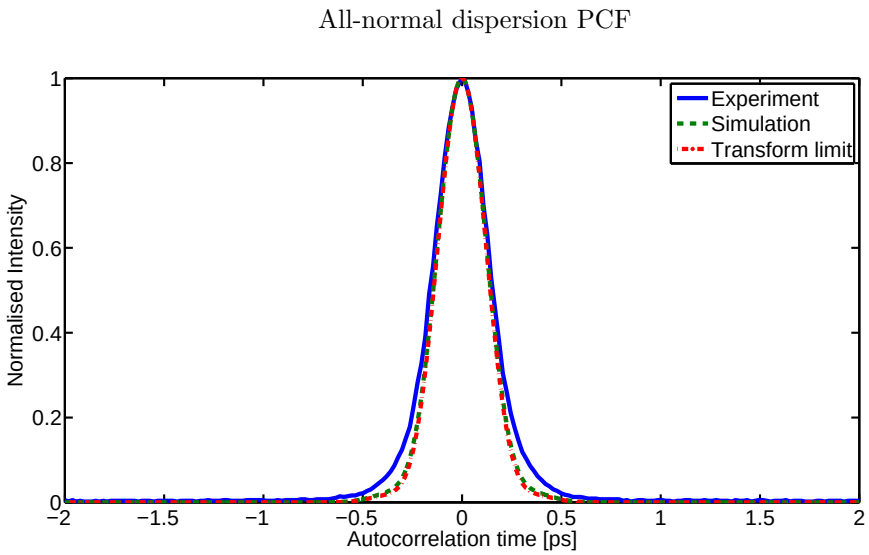

b)

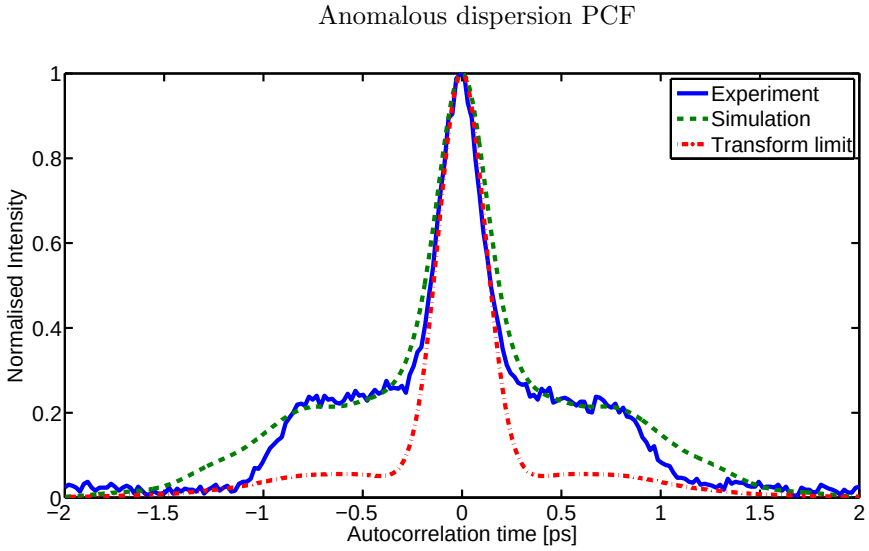

Figure 5-10: Intensity autocorrelation traces of a) spectral slices centred at 1250 nm, with root-mean-square bandwidth 12 nm, from all-normal dispersion supercontinuum, b) spectral slices centred at 1260 nm, with root-mean-square bandwidth 13 nm, from anomalous dispersion supercontinuum. Each plot shows an autocorrelation trace obtained experimentally, a simulated autocorrelation trace and a simulated transform limited autocorrelation trace calculated using the simulated supercontinuum spectra plotted in figure 5-6

Figure 5-11 shows ten of the autocorrelation traces calculated from filtering the twenty independently generated anomalous dispersion supercontinua. These contribute to the average simulated autocorrelation trace plotted in figure 5-10 (b). It is clear that the temporal profile fluctuates a great deal from shot to shot. In contrast, the autocorrelation traces calculated from the normal dispersion supercontinuum simulations have negligible differences from shot to shot.

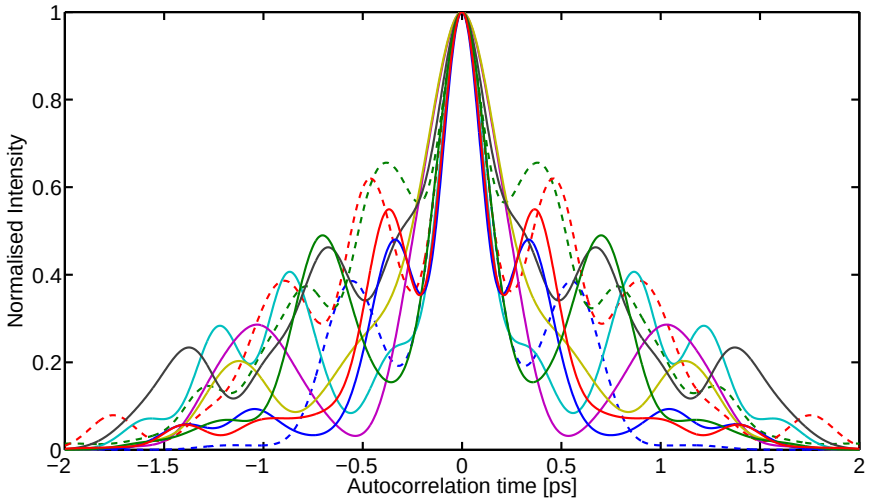

Figure 5-11: Ten autocorrelation traces calculated from ten of the independently generated anomalous dispersion supercontinua plotted in figure 5-6. These contribute to the average simulated autocorrelation trace plotted in figure 5-10 (b)

5.4 Conclusions and future outlook

This chapter contains a demonstration of a coherent tunable sub-picosecond laser source based on spectral filtering of a supercontinuum generated in all-normal dispersion PCF. The filtered pulse properties are shown to be superior to pulses obtained by filtering a supercontinuum generated in the anomalous dispersion regime of a PCF.

Supercontinua were generated in two types of PCF, an all-normal dispersion PCF (ND1064) and PCF with anomalous dispersion at the pump wavelength. The supercontinuum pulses were spectrally filtered, and the resulting pulses were analysed in the time domain using an intensity autocorrelator. The pulses obtained from the all-normal dispersion supercontinuum all had RMS autocorrelation widths of less than 1 ps, and had clean, shoulder-free profiles. Conversely, the pulses obtained from the anomalous dispersion supercontinuum had broad shoulders as a result of Raman shifted solitons, and large side-pulses which were due to higher order modes. Simulations carried out using the GNLSE code agreed well with the measured data. The simulations indicated that the filtered all-normal dispersion supercontinuum pulses are very

stable, whereas the filtered anomalous dispersion supercontinuum pulses are subject to large fluctuations from shot to shot.

In chapter 4, re-compressibility of the all-normal dispersion supercontinuum was demonstrated. The high coherence and stability, and the linear chirp allowed the spectrum generated in a short length of fibre to be re-compressed using only linear chirp compensation. The all-normal dispersion supercontinuum in this chapter was generated in a longer length of PCF, so has a nonlinear chirp. However, the chirp across the narrow bandwidth of the filtered pulses is approximately linear. The filtered pulses could therefore theoretically be compressed to a duration close to their transform limit, using a prism pair compressor or grating pair compressor. The filtered anomalous dispersion supercontinuum pulses would not be re-compressible because of their instability.

Tunable ultra-short pulsed laser systems based on all-normal dispersion supercontinua could be a solution for improving resolution in experiments currently using tunable systems based on anomalous supercontinuum sources. One disadvantage of the all-normal dispersion supercontinuum is the limited bandwidth. One way to increase the bandwidth would be to increase the power which can be coupled into the fibre. End-sealing the input face by collapsing the air holes would increase the fibre end damage threshold. Increased power could extend spectral broadening into the visible, which would open up further applications in microscopy and spectroscopy. The spectral power density would also be increased, so that such a compact ultrafast source centred at 800 nm could rival the more bulky Ti:Sapphire laser systems. The compact set-up could include an acousto-optic filter in place of the 4-f filter, to allow electronic tuning and bandwidth adjustment.

Chapter 6

Coherence measurements

6.1 Introduction

This chapter contains measurements of the mutual spectral coherence of supercontinua generated in all-normal dispersion PCF. The mutual spectral coherence of a supercontinuum is given by equation 2.22, and is exactly equal to the visibility of interference fringes obtained when interfering independently generated supercontinuum pulses. In the experiment described in this chapter, the independently generated supercontinua are generated by consecutive laser pulses.

Supercontinuum noise properties have been studied extensively both theoretically [69, 111, 112] and experimentally. One way to experimentally characterise supercontinuum noise is to study the broadband radio frequency noise [85, 113–115]. Other methods involve measuring the visibility of interference fringes. In one study [74], two supercontinua were independently generated by identical pulses in separate pieces of the same PCF, and the interference fringes viewed spatially using Young's interference [73]. However, this method is unlikely to produce high quality fringes due to the slightly different input coupling conditions for each PCF. The method used to characterise coherence in this chapter is based on the delayed pulse technique described in [79, 116, 117].

An interferometer is used to reduce the delay between consecutive supercontinuum pulses, so that interference can be viewed spectrally using an optical spectrum analyser (OSA). A generic set-up for the delayed pulse method is shown in figure 6-1. It is important to note that the pulses should not be temporally overlapped for spectral interference fringes to be seen. The Fourier spectrum of two closely spaced laser pulses is a spectral interference pattern, with a modulation period equal to the inverse of the pulse separation. The pulse train emitted from a laser with a 76 MHz repetition rate has a pulse separation of 3.95 m, and a spectrum with modulations separated by 76 MHz. However, it is not possible to resolve this fine spectral structure using the OSA. The delayed pulse method decreases the pulse separation to produce resolvable spectral interference. For the OSA used in this experiment, with a minimum resolution of 0.05 nm, fully resolvable fringes occur at a pulse separation of a few 100 μm.

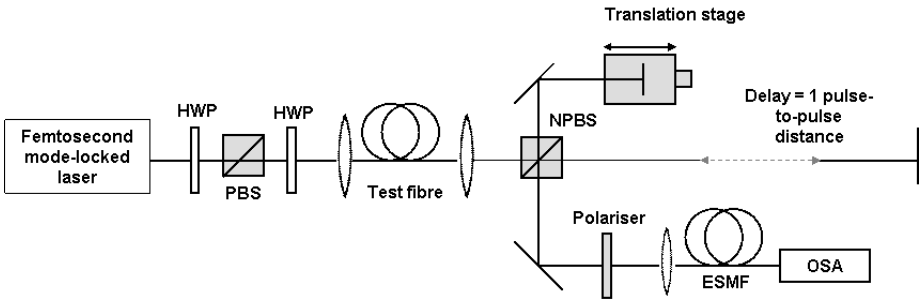

Figure 6-1: Generic set-up for measuring supercontinuum coherence using the delayed pulse method. HWP, half wave plate; PBS, polarising beam splitter; NBPS, non-polarising beam splitter; ESMF, endlessly-single-mode fibre; OSA, optical spectrum analyser

6.2 Coherence measurement of supercontinuum generated in ND1064

6.2.1 Fibre laser

A delayed pulse experiment was set up using the amplified mode-locked fibre laser (Fianium Ltd) used in experiments in chapters 4 and 5. This work was carried out by the author alone. The laser emits chirped pulses with a 5.5 ps FWHM assuming a Gaussian pulse profile, and is centred at 1064 nm. The laser spectrum is plotted in figure 6-2 (a). The repetition rate of the laser is 20 MHz, and so interference of consecutive pulses requires a 15 m free-space delay arm. The experiment was initially set up with the chirped pulses from the laser being compressed to 400 fs FWHM duration in a length of hollow core PCF, as described in chapter 4. Supercontinuum was generated using these pulses in a length of ND1064, and the interference fringes obtained were found to be extremely unstable. To investigate the cause of this noise, the hollow core and supercontinuum fibres were removed from the set-up, and the pulse to pulse interference of pulses directly from the fibre laser were measured. Surprisingly, the fringes obtained were also extremely unstable. An example of the noisy fringes is plotted in figure 6-2 (b). The set-up was not optimised to obtain the highest visibility fringes, and therefore the fringe visibility does not represent the spectral coherence of the pulses.

The interferometer was re-configured so that both arms were short and equal in length, to observe the same-pulse interference. Stable interference fringes were obtained, as in figure 6-2 (c). Again, the set-up was not optimised to obtain the highest visibility fringes. To rule out the possibility of air currents or component vibrations in the 15 m long delay arm contributing to the instability of the pulse-to-pulse fringes, the interferometer was re-built with two 15 m long arms. In this configuration, the interference fringes were stable. Therefore, the conclusion reached was that the fibre laser has unstable phase or timing jitter, making it impossible to carry out the measurement.

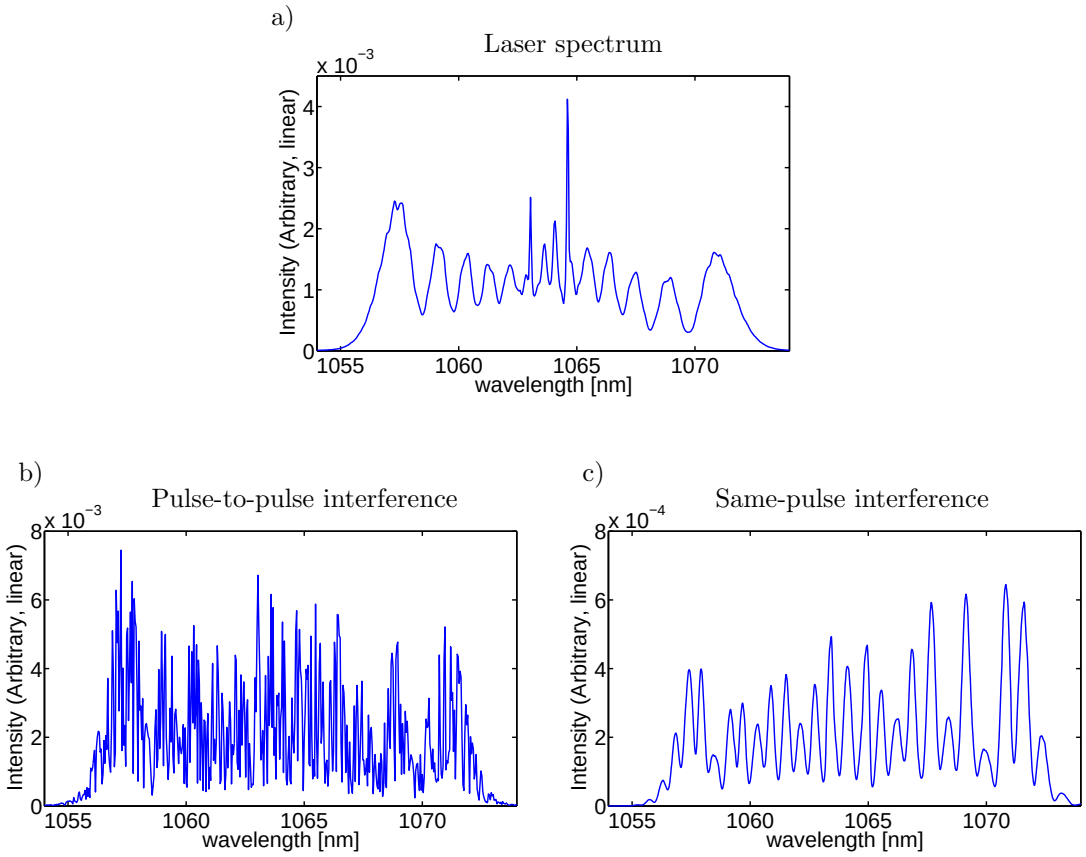

Figure 6-2: a) Measured spectrum of fibre laser output, b) unstable spectral interference fringes obtained from pulse-to-pulse interference, and c) stable spectral interference fringes obtained from same-pulse interference. The pulse-to-pulse interference fringes are noisy as a result of laser pulse instability. The set-up was not optimised to obtain the high visibility interference fringes

6.2.2 Solid state laser

As an alternative to the fibre laser described in the previous section, a solid state diode-pumped Yb:KGW laser was used, which was expected to have high pulse-to-pulse stability. This work was carried out in collaboration with Peter Mosley. The laser emits pulses centred at 1037 nm, with 70 fs FWHM duration, and average power 1 W. The repetition rate of the laser is 76 MHz, which means that the free-space distance between consecutive laser pulses is 3.95 metres.

The maximum average power which could be coupled into the all-normal dispersion PCF in the experiment was 300 mW. The spectrum of the supercontinuum generated in a 4 cm length of ND1064 is plotted in figure 6-3 (a). The spectral interference fringes are plotted in figure 6-3 (b), in blue. The green and red curves are the theoretical maximum and minimum fringe intensities (assuming full spectral coherence), which were calculated using

$$I_{\max} = (\sqrt{I_1} + \sqrt{I_2})^2 \tag{6.1}$$

$$I_{\min} = (\sqrt{I_1} - \sqrt{I_2})^2 \tag{6.2}$$

where $I_{\max}$ and $I_{\min}$ are the maximum and minimum fringe intensities, and I_1 and I_2 are the spectral intensities recorded in each individual arm of the interferometer. The extent of the interference fringes closely matches these maximum and minimum values, indicating high visibility and therefore high spectral coherence.

For comparison, the same experiment was carried out using "white light" supercontinuum PCF with anomalous dispersion at the pump wavelength [51]. This is the same anomalous dispersion PCF used in experiments in chapter 5. The spectrum obtained in 4 cm using these pump pulses is plotted in figure 6-4 (a). The spectral interference pattern, plotted in 6-4 (b) shows good visibility, comparable with the visibility of the all-normal dispersion supercontinuum fringes. The high spectral coherence is a result of the input pulses being short, so that the spectrum broadens before modulation instabilities become dominant. Therefore, the coherence of all-normal dispersion supercontinuum is not superior to anomalous dispersion supercontinuum for the input pulse parameters used in this experiment.

a)

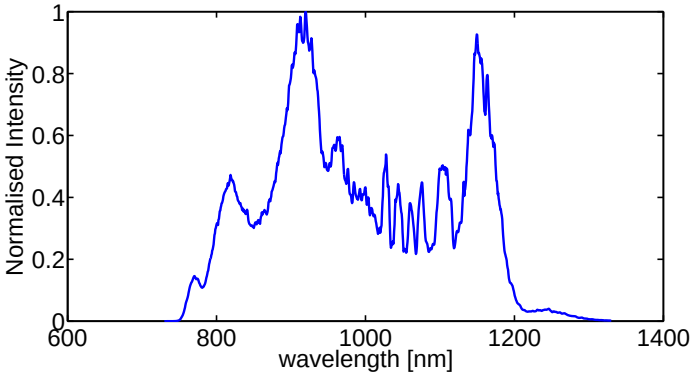

b)

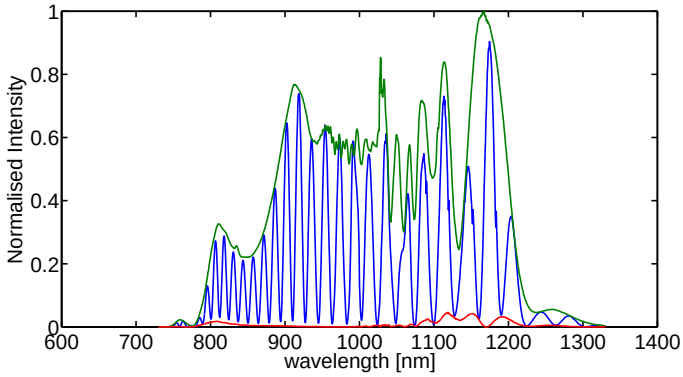

Figure 6-3: a) Spectrum generated in 4 cm ND1064, using 70 fs pulses centred at 1037 nm, with an average output power of 300 mW at a repetition rate of 76 MHz b) Spectral interference fringes (blue) obtained using the delayed pulse method. Green and red curves are theoretical maximum and minimum fringe intensities respectively, calculated using equations 6.1 and 6.2

a)

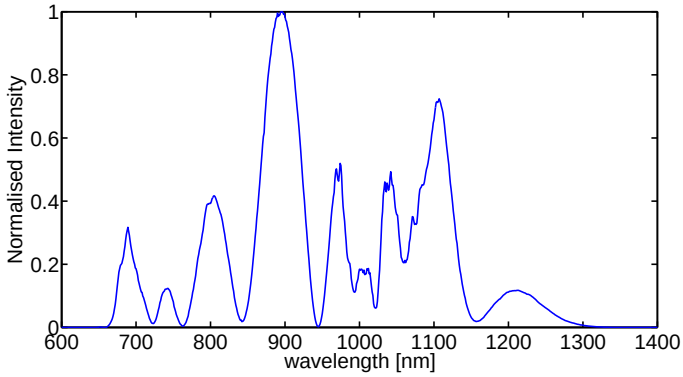

b)

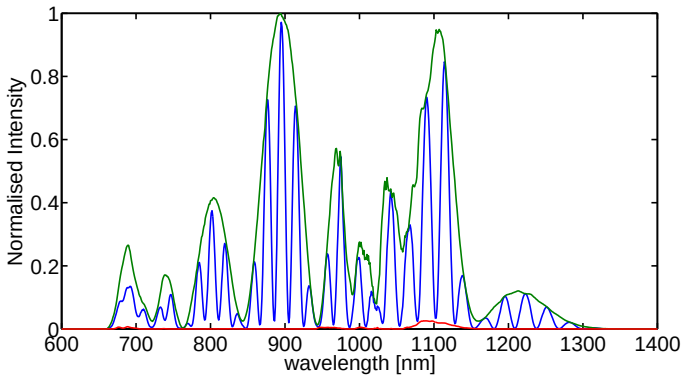

Figure 6-4: a) Spectrum generated in 4 cm anomalous dispersion PCF, using 70 fs pulses centred at 1037 nm, with an average output power of 300 mW at a repetition rate of 76 MHz b) Spectral interference fringes (blue) obtained using the delayed pulse method. Green and red curves are theoretical maximum and minimum fringe intensities respectively, calculated using equations 6.1 and 6.2

6.3 Coherence measurement of supercontinuum generated in ND800

Delayed pulse coherence measurements were also carried out for the supercontinuum generated in ND800 PCF, using a mode-locked Ti:Sapphire laser source. This work was carried out by the author alone. The laser emits 200 fs FWHM transform limited pulses, with an average power of 500 mW at a repetition rate 76 MHz, centred at 800 nm.

The supercontinua generated in various lengths of ND800 are plotted in figure 6-5. All spectra had an average output power of approximately 130 mW. The spectral shape was sensitive to the input polarisation, so the polarisation at the input was optimised to obtain the most linearly polarised output, ie. it was matched with one of the polarisation axes of the fibre. This was kept constant throughout the experiment. After 4 cm the spectrum had a typical SPM shape, with a small side-band on the short wavelength side produced by OWB. After further propagation the spectrum is broader, with OWB occurring on the long wavelength side of the spectrum also, and the SPM modulations flattening.

The ND800 spectra have a dip in the centre, which is not present in the spectra generated in ND1064 in previous chapters. One difference between ND1064 and ND800 is the value of dispersion at the pump wavelength; the dispersion of ND1064 at 1064 nm is approximately -6 ps/nm/km, and the dispersion of ND800 at 800 nm is approximately zero. Simulations were carried out to investigate the effect of the dispersion profile on the spectral structure, and these are plotted in figure 6-6. The pump pulse parameters used in the simulation matched the real pulse parameters used to generate supercontinua in figure 6-5, and all nonlinear effects were included in the simulation. Dispersion curve C is fitted to the measured dispersion of ND800. Dispersion profiles D and E are all-normal, with minimum dispersion values of approximately -10 ps/nm/km and -20 ps/nm/km respectively. Dispersion profiles A and B have two ZDWs, and peak dispersion values of approximately 10 ps/nm/km and 20 ps/nm/km respectively. These dispersion profiles were all generated using the empirical formula. Supercontinua generated in PCF with two ZDWs exhibit a two-peak structure as a result of soliton fission and dispersive wave generation on the normal dispersion side of each ZDW [81]. In all-normal dispersion PCF, solitons do not form and the two-peak structure is a result of OWB. The higher the value of normal dispersion, the sooner the pulse edges become steep and the sooner the onset of OWB. During propagation in a fibre with dispersion E, OWB occurs quickly, and side bands are generated close to the pump wavelength, resulting in a spectrum which is narrow and flat. For dispersion C however, the spectrum broadens by SPM to a broader bandwidth before OWB occurs, so the OWB side-bands are generated further away from the pump.

The set up for the coherence measurement is shown in figure 6-7. The laser repetition rate 76 MHz corresponds to a pulse separation of 3.95 metres. A Mach-Zender interferometer was used to minimise feedback into the laser. 1 m of ND800 was used to generate a smooth supercontinuum. For comparison, the same measurement was carried out for a supercontinuum generated in 1 m PCF with anomalous dispersion at 800 nm. The anomalous dispersion PCF has a 2.5 μm diameter core and a high air filling fraction, so can be modelled as a strand of

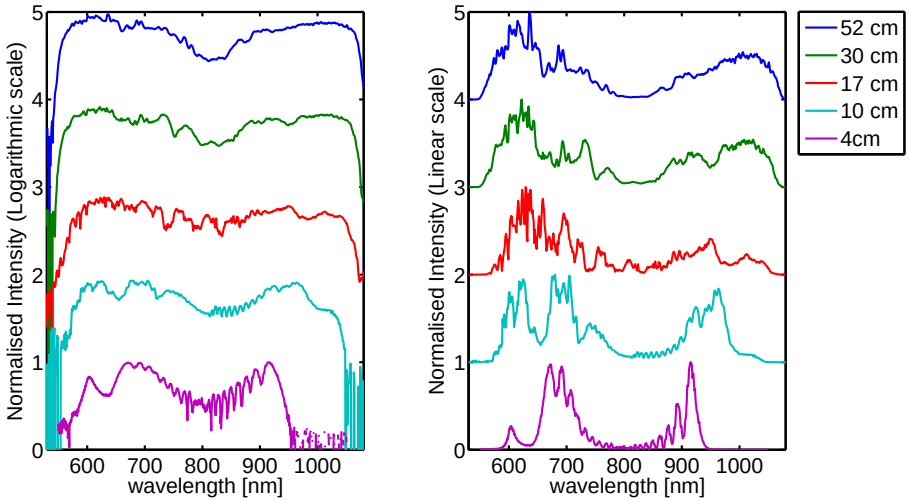

Figure 6-5: Evolution with length of supercontinuum spectra generated in ND800 PCF pumped with Ti:Sapphire laser. Pump pulses were centred at 800 nm, with average output power 130 mW at a repetition rate of 76 MHz. Pulse FWHM is approximately 200 fs. The spectra are plotted on a logarithmic scale (left) and a linear scale (right). Each spectrum is offset from the spectrum below by 1 normalised intensity unit

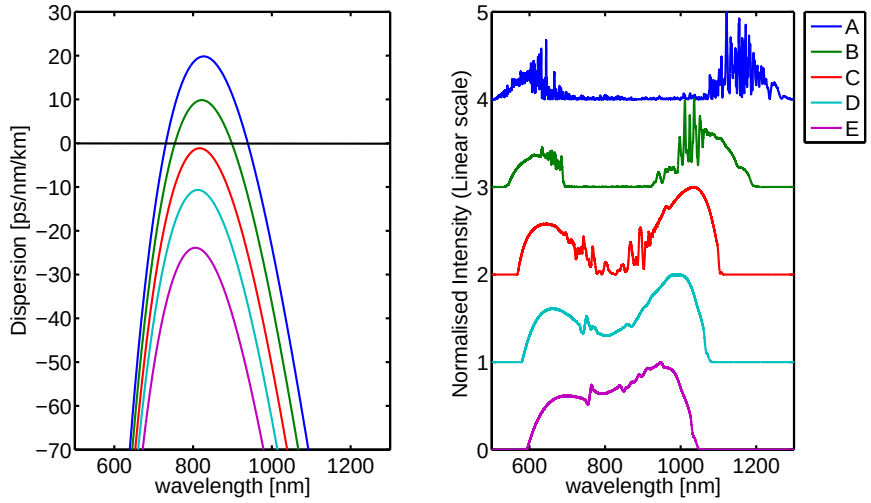

Figure 6-6: Left: Dispersion curves generated using empirical formula for investigating numerically the effect of the dispersion profile on the generated spectrum; Right: Simulated spectra generated in PCF with dispersion curves plotted on the left, showing that a central dip is present in all-normal dispersion supercontinua generated in PCF with a small value of minimum dispersion. Each spectrum is offset from the spectrum below by 1 normalised intensity unit

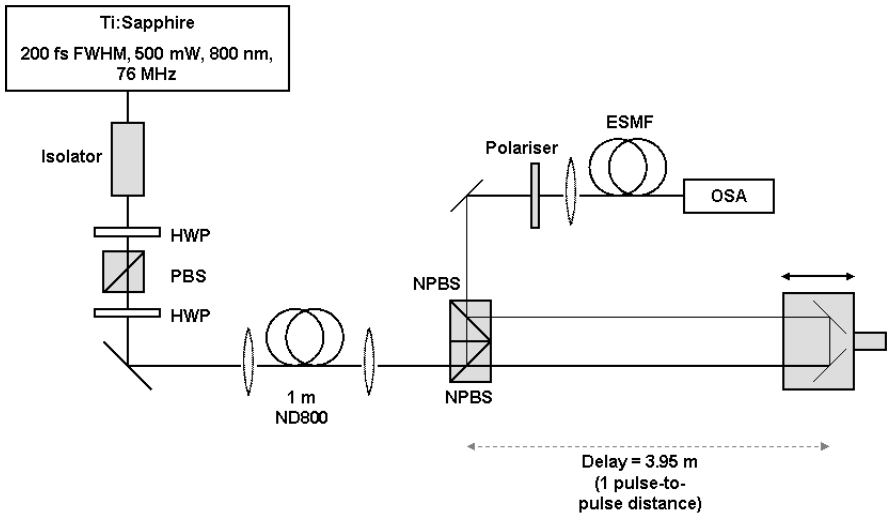

Figure 6-7: Experimental set-up for measuring the coherence of supercontinuum generated in ND800 PCF, pumped with a Ti:Sapphire laser with a 76 MHz repetition rate. HWP, half wave plate; PBS, polarising beam splitter; NBPS, non-polarising beam splitter; ESMF, endlessly-single-mode fibre; OSA, optical spectrum analyser

silica with 2.5μm diameter. The measured dispersion profile of ND800 is compared with the calculated dispersion for a 2.5 μm diameter silica strand in figure 6-8.

After the isolator and power attenuation components, the available power for coupling into the fibre is approximately 350 mW. It is possible to obtain approximately 100 mW output power from each fibre. However, at this power the all-normal dispersion supercontinuum interference exhibits fast time-dependent intensity fluctuations, which are thought to be due to nonlinear polarisation dynamics. Small-core PCF are known to have a weak birefringence originating from distortions during fabrication [91, 118]. If the birefringence is nonlinear then a small drift in the input coupling conditions would cause the polarisation state at the fibre output to fluctuate. The visibility of the interference fringes is dependent on the polarisation of both signals matching, so a changing polarisation would result in oscillations in the fringe visibility. At 50 mW output power this effect is not significant, so this is the output power used for comparing the two fibres. The spectra generated in each fibre at 50 mW output power are plotted in figure 6-9. A wider spectrum is generated in ND800 due to the lower value of dispersion at the pump wavelength.

The isolator used in the set up is designed to operate in the range 700 nm to 900 nm. Some problems were experienced when the spectral broadening in the supercontinuum fibre under test extended beyond this spectral range, and feedback into the laser cavity stopped the laser from mode-locking. This problem was avoided simply by re-cleaving the fibre until there was no feedback into the laser. There is also some time-dependent noise on the spectral interference fringes recorded, which is likely to be due to table vibrations or air currents. Due to time constraints this noise could not be eliminated.

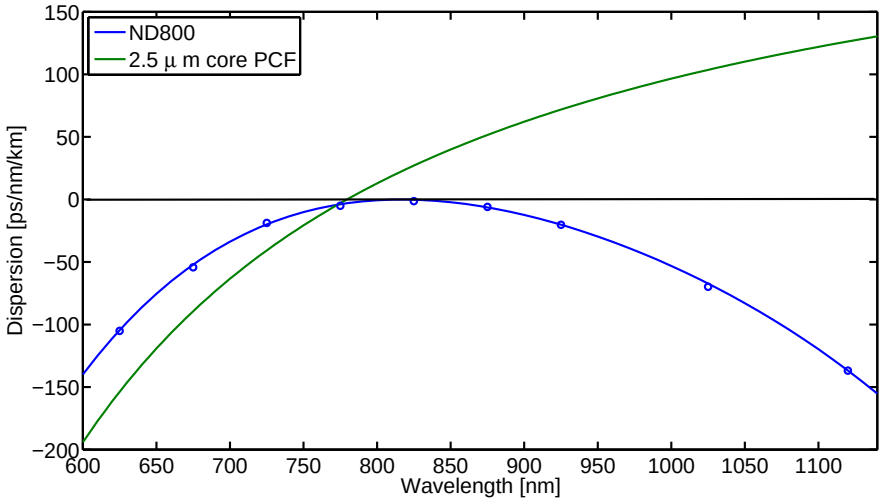

Figure 6-8: Measured dispersion of ND800 and modelled dispersion of a 2.5 μm core PCF with a high air-filling fraction, approximated as a 2.5 μm diameter silica strand suspended in air (calculations by William Wadsworth)

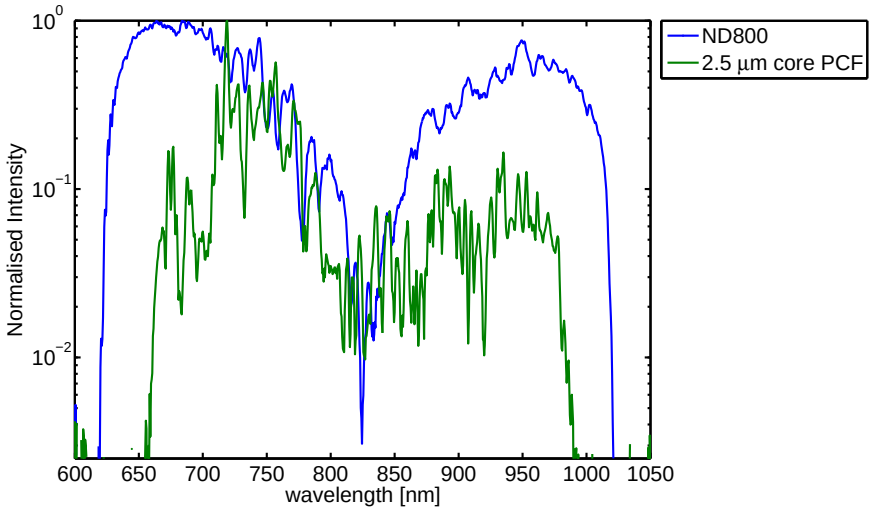

Figure 6-9: Measured supercontinuum spectra generated in 1 m of ND800, and 2.5 μm core PCF, pumped with Ti:Sapphire pulses centred at 800 nm with 50 mW output power at 76 MHz repetition rate

Spectral interference fringes were recorded across the whole bandwidth of the supercontinuum, in 20 nm windows spaced every 50 nm. This was done so that the maximum resolution of the OSA could be used, and the fringe spacing could be made small enough to resolve structure on the supercontinuum spectrum. For each wavelength window, the coupling into the ESMF was adjusted so that the intensities in each arm were approximately equal. This was not always possible because the beam from the long delay arm was more diverged at the ESMF input than the beam from the short arm. To compensate for this, the fringe spectra were normalised with respect to the theoretical maximum and minimum fringe intensities, defined in equations 6.1 and 6.2.

Normalised spectral fringes are plotted in figures 6-10 and 6-11 for ND800 and the 2.5 μm core PCF supercontinua with 50 mW average output power. The fringe visibility is approximately equal to 1 across the entire bandwidth for the all-normal dispersion supercontinuum, demonstrating a high degree of spectral coherence. In comparison, the fringe visibility for the anomalous dispersion supercontinuum is less than 1 over the entire bandwidth, with lowest visibility at the short and long wavelength edges of the spectrum. Physically, this pattern in the coherence arises because the frequencies close to the pump are generated in the initial stage via SPM, so are spectrally coherent. The frequencies further from the pump are generated by soliton fission, SSFS and dispersive wave generation. As the input pulses are relatively long, the soliton fission process is likely to be dominated by MI, resulting in poor coherence.

When the output power from anomalous dispersion fibre is increased to 100 mW, the fringe visibility is reduced overall, and is zero at the spectrum edges. The normalised fringes are plotted in figure 6-12. Increasing the power increases the soliton order, resulting in a more dominant MI contribution to the spectral broadening process, and thus lower spectral coherence. An increase in power for the all-normal dispersion supercontinuum is expected not to have an impact on the spectral coherence, because the broadening mechanisms are not seeded by laser noise. However, this could not be verified experimentally due to the instabilities caused by nonlinear polarisation dynamics.

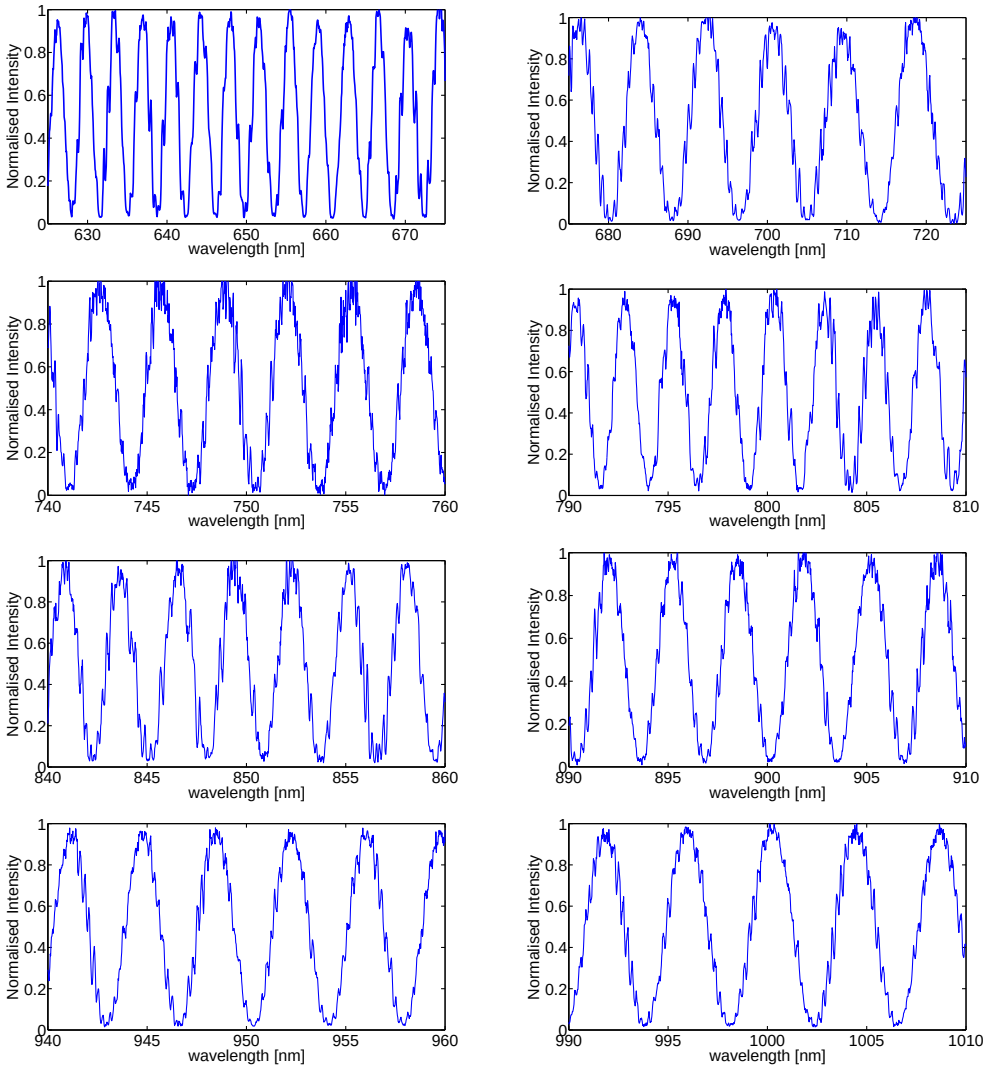

Figure 6-10: Spectral interference fringes of supercontinuum generated in 1 m ND800 PCF, with 50 mW average output power. The interference fringes are normalised with respect to the maximum and minimum fringe intensities expected for full coherence. The optical delay and hence the fringe spacing was adjusted between taking data sets centred at 650 nm and 700 nm, and again between data sets centred at 750 nm and 800 nm

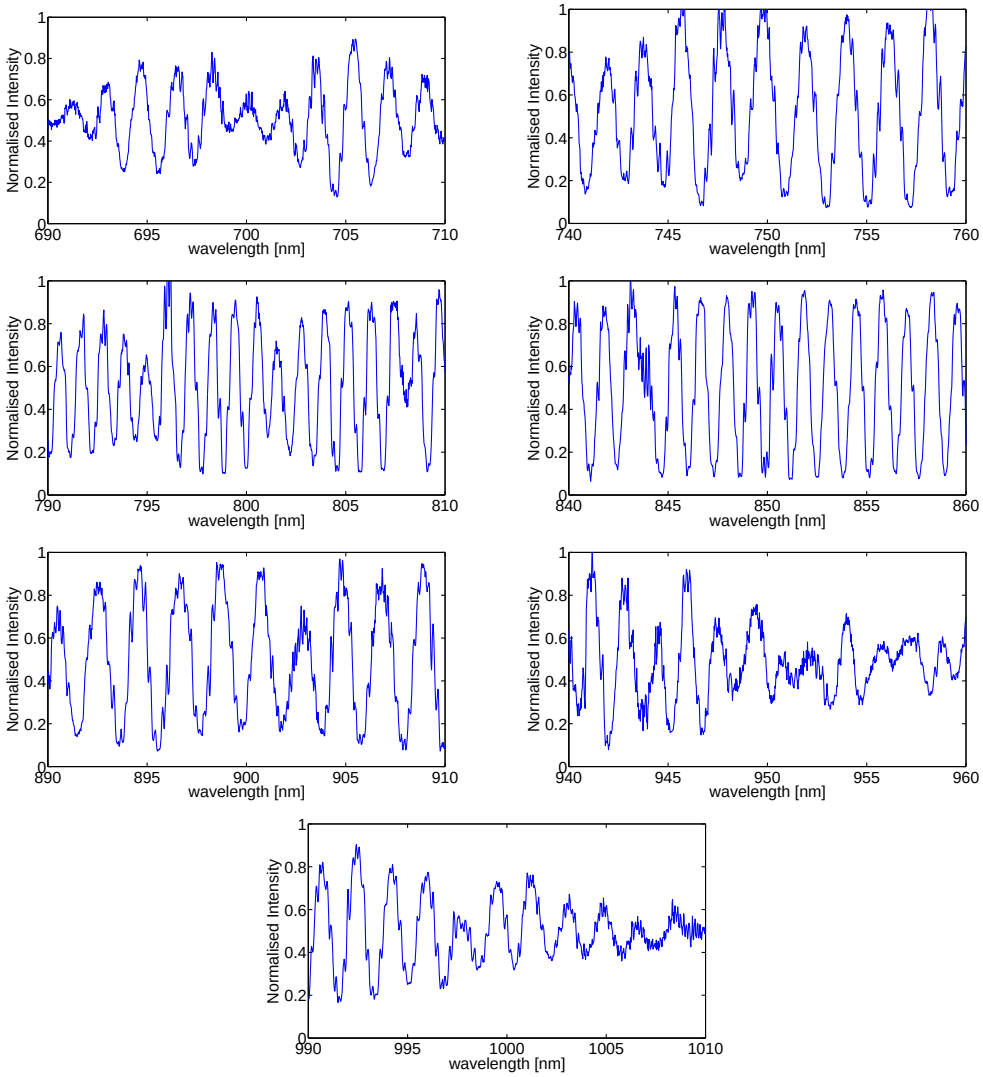

Figure 6-11: Spectral interference fringes of supercontinuum generated in 1 m 2.5 μm core PCF, with 50 mW average output power. The interference fringes are normalised with respect to the maximum and minimum fringe intensities expected for full coherence. The optical delay and hence the fringe spacing was adjusted between taking data sets centred at 750 nm and 800 nm

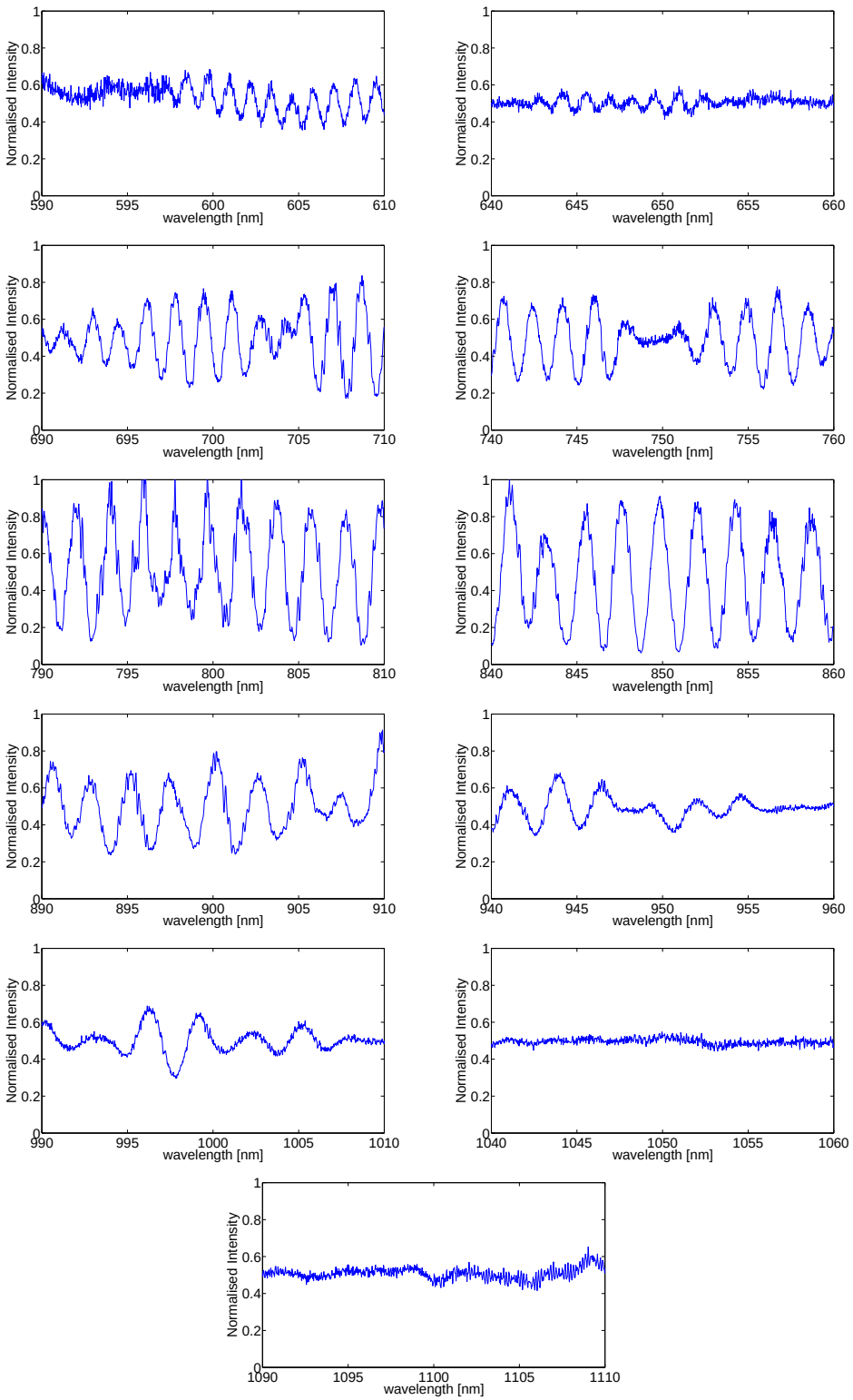

Figure 6-12: Spectral interference fringes of supercontinuum generated in 1 m 2.5 μm core PCF, with 100 mW average output power. The interference fringes are normalised with respect to the maximum and minimum fringe intensities expected for full coherence

6.4 Conclusions and future outlook

In this chapter it was demonstrated experimentally that the supercontinua generated in all-normal dispersion PCF have high spectral coherence. A delayed pulse method was used to view the spectral interference between supercontinuum pulses generated by consecutive laser pulses. Measurements could not be carried out using the 1064 nm fibre laser (Fianium Ltd) used to generate supercontinua in chapters 4 and 5, because the pulse-to-pulse stability was not sufficient. A delayed pulse experiment using a solid state Yb:KGW laser emitting 70 fs pulses centred at 1030 nm was carried out. The supercontinuum generated in 4 cm of ND1064 using these pulses had high quality interference fringes across the whole bandwidth, demonstrating high coherence. For comparison, the interference of supercontinuum generated in a 4 cm length of PCF with anomalous dispersion at the pump wavelength was measured. The fringe visibility in this case was also high, because the short duration of the pump pulses causes the soliton fission spectrum to broaden quickly, before modulation instability becomes significant.

Another delayed pulse measurement was carried out for supercontinuum generated in 1 m of ND800 using 200 fs FWHM Ti:sapphire pulses centred at 800 nm. The spectral interference fringes had high visibility across the full bandwidth, demonstrating high spectral coherence. This was compared with the spectral interference of supercontinuum pulses generated in PCF with anomalous dispersion at 800 nm. The fringe visibility in this case was less than 1 across the whole bandwidth, and was lowest at the short and long wavelength edges of the spectrum. These measurements support the trend in coherence predicted by simulations. The all-normal supercontinuum maintains high coherence across the full spectrum for all pump pulse parameters. The anomalous dispersion supercontinuum maintains coherence for short pump pulses, but coherence is reduced for long pump pulses because MI dominates the soliton break-up process.

The delayed pulse experiment was sensitive to laser noise, because small fluctuations in pulse separation cause large changes in the appearance of the spectral interference fringes. To carry out such a measurement it is vital to use a laser with high pulse-to-pulse stability, and to minimise vibrations and air currents in the set-up. The interference fringes recorded for experiments carried out using the Ti:Sapphire laser have some small time-dependent oscillations on them. This noise may be reduced by eliminating table vibrations and air currents.

The supercontinua generated in ND800 PCF using the Ti:Sapphire pulses were highly dependent on input polarisation. In addition, some instabilities of the spectral fringes were observed at high power, suggesting a nonlinear polarisation effect. PCFs with small core sizes are known to have a weak value of birefringence [91, 118]. The stability in the experiment would be improved by fabricating a highly-birefringent polarisation-maintaining all-normal GVD PCF. This would allow stable interference fringes to be observed at higher powers.

Chapter 7

Conclusions and future outlook

The research described in this thesis provides theoretical and experimental evidence to support the proposal that PCF with all-normal dispersion profiles can be used to generate supercontinua with high coherence and intensity stability. The results obtained also demonstrate the applicability of such a supercontinuum source to the field of ultra-short pulse compression, and as a broadband tunable ultra-short laser source.

PCFs with all-normal dispersion profiles were successfully fabricated with low dispersion for pumping at 800 nm (ND800), and at 1064 nm (ND1064). The supercontinua generated in these fibres have very different properties to more common supercontinua generated in the anomalous dispersion regime of PCFs. In the normal dispersion regime spectral broadening occurs via self phase modulation, and optical wave breaking, resulting in a symmetrical and flat spectrum, which has high spectral coherence. In the anomalous dispersion regime however, the spectrum is broadened by a process of soliton break-up and SSFS, which results in a complex spectral structure. The process is very sensitive to laser pulse fluctuations, and can be influenced by MI, which results in poor spectral coherence. The spectra obtained experimentally were in good agreement with simulations carried out using the GNLSE code.

In chapter 4 it was shown that supercontinuum generated in all-normal dispersion fibre can be compressed using only linear chirp compensation from a prism pair. High coherence and stability is essential for successful pulse re-compression. This was the first demonstration of pulse re-compression from all-normal dispersion supercontinuum. Initial input pulses with 400 fs FWHM and were broadened in a 4 cm length of ND1064 to 200 nm bandwidth. This pulse was compressed to 26 fs FWHM, which is within a factor of two of the spectrum transform limit. This demonstrates the high spectral coherence, stability, and linear chirp of the supercontinuum generated in a short length of all-normal dispersion fibre. The compression factor of 16 exceeds that which other groups have achieved since [59, 94]. Theoretically it is possible to re-compress close to the transform limited duration using only linear chirp compensation, with some shoulders remaining from the uncompensated higher order dispersion. However, the accuracy of the experimental set-up used was not sufficient to obtain a shorter pulse. Simulations showed that linear re-compression of a supercontinuum generated in the

anomalous dispersion regime would be limited by not only the nonlinear chirp, but also by the unstable spectral phase, and temporal jitter. A SLM can be used to compensate for nonlinear chirp, but re-compression would still be limited by the shot-to-shot phase fluctuations. On the other hand, supercontinuum generated in a longer piece of the all-normal dispersion fibre could theoretically be fully compressed using a SLM.

In chapter 5 a compact broadband tunable source of ultra-short pulses was obtained by spectrally filtering an all-normal dispersion supercontinuum. A supercontinuum spanning 750 nm was generated in a 20 cm length of ND1064. The supercontinuum was spectrally filtered, and the pulses obtained were analysed in the time domain using an autocorrelator. A range of bandwidths and central wavelengths were measured, and the filtered pulses were all less than 1 ps in duration. An anomalous dispersion PCF supercontinuum was used for comparison, which yielded slightly longer pulses which had a large fraction of their energy contained in the shoulders and in higher order modes. The bandwidth of the all-normal dispersion fibre supercontinuum is limited, but it is advantageous for obtaining high spectral power density. The laser source in this case was a compact fibre laser, and the supercontinuum bandwidth extended to 800 nm, so this system could be used as a compact and portable alternative to commonly used Ti:sapphire laser sources. Simulations have shown that the filtered slices would be re-compressible by simple linear chirp compensation, improving the peak power. The peak power and bandwidth could be improved by increasing the amount of power coupled into the fibre. The input power was limited in the experiments by damage to the fibre end-face. This could be improved by treating the fibre end-face ie. collapsing the air-holes. Obtaining frequencies further into the visible would be useful for applications such as Raman microscopy, and fluorescence microscopy. A broader bandwidth might also be achieved by using shorter pump pulses, or by flattening the dispersion [119].

In chapter 6 the high spectral coherence of the all-normal dispersion supercontinuum was demonstrated using a delayed-pulse interference technique. A spectrum spanning 400 nm was generated in 1 m of ND800 using a Ti:Sapphire laser source. The supercontinuum pulses were passed through an interferometer which brought consecutive pulses close together temporally. Interference fringes were measured spectrally, and found to have high visibility, and thus high coherence, at all wavelengths. A supercontinuum generated in a PCF with anomalous dispersion at 800 nm was also tested using this system, and the fringe visibility was reduced away from the pump wavelength. These results support the theory and the numerical modelling presented in chapter 3. The shape of the spectra obtained using both all-normal GVD fibres were found to be highly dependent on input polarisation. In the interferometric coherence measurement, at high power, instability in the fringes was observed which made the measurement impossible. This is likely to be due to nonlinear polarisation dynamics [118]. To solve this problem, a highly birefringent polarisation-maintaining all-normal dispersion PCF could be fabricated.

The high coherence and stability of the all-normal dispersion supercontinuum makes it ideal for frequency comb generation. However, the obtainable bandwidth is a limitation for this application. The supercontinuum would also be ideal for many types of microscopy and spectroscopy, especially those which are time-resolved such as pump-probe spectroscopy.

All-normal dispersion PCFs are of interest for self-similarity experiments. A careful balance of nonlinearity, dispersion and gain in a high power fibre amplifier can cause the shape of an arbitrary input pulse to converge to a self similar pulse shape. These self similar pulses are known as optical similaritons, and are more stable at high power than optical solitons. Therefore they could be of use for high power pulse amplification in optical fibres [120, 121], and work is currently underway with the Wise Group at Cornell to pursue this avenue.

List of acronyms

CW - continuous wave

ESMF - endlessly single mode fibre

FWHM - full-width half-maximum

FWM - four wave mixing

GNLSE - Generalised nonlinear Schrödinger equation

GVD - group velocity dispersion

HC-PCF - hollow core photonic crystal fibre

ID/OD - inner diameter/outer diameter

MI - modulation instability

OWB - optical wave breaking

PCF - photonic crystal fibre

RMS - root-mean-square

SEM - scanning electron microscope

SLM - spatial light modulator

SPM - self phase modulation

SSFS - soliton self frequency shift

XPM - cross phase modulation

ZDW - zero dispersion wavelength

Publications list

1. L. E. Hooper, P. J. Mosley, A. C. Muir, W. J. Wadsworth, and J. C. Knight. All-normal dispersion photonic crystal fiber for coherent supercontinuum generation. In Conference on Lasers and Electro-Optics, page CTuX4. Optical Society of America, 2010.

2. L. E. Hooper, P. J. Mosley, A. C. Muir, W. J. Wadsworth and J. C. Knight. Low-noise supercontinuum generation in a photonic crystal fiber with all normal dispersion. In Photon 10 (Southampton UK, August 2010), Abstract Book.

3. L. E. Hooper, P. J. Mosley, A. C. Muir, W. J. Wadsworth, and J. C. Knight. Coherent supercontinuum generation in photonic crystal fiber with all-normal group velocity dispersion. Optics Express, 19(6):49024907, 2011.

4. L. E. Hooper, P. J. Mosley, A. C. Muir, J. M. Dudley, W. J. Wadsworth and J. C. Knight. Photonic crystal fibers with all-normal group velocity dispersion for coherent supercontinuum generation. In Fibre and Optical Passive Components (WFOPC), 2011 7th Workshop on, Abstract book.

5. L. E. Hooper, P. J. Mosley, A. C. Muir, F. Yu, B. J. Mangan,W. J.Wadsworth, J. C. Knight, and J. M. Dudley. Coherent widely tunable source of sub-picosecond pulses using all-normal dispersion fiber supercontinuum. In Fibre and Optical Passive Components (WFOPC), 2011 7th Workshop on, pages 1 4, 2011.

6. L. E. Hooper, P. J. Mosley, A. C. Muir, F. Yu, B. J. Mangan,W. J.Wadsworth, J. C. Knight. Direct coherence measurement of supercontinuum generated in all-normal dispersion photonic crystal fibre. *In preparation*

Bibliography

[1] L. Cognolato. Chemical vapour deposition for optical fibre technology. *Journal de Physique IV*, 5(C5):975–987, 1995.

[2] Jeff Hecht. *City of Light*. Oxford University Press, 1999.

[3] C. W. Hansell. U.S. Patent 1,751,584 "Picture Transmission", 1930.

[4] National Research Council. "Brian O'Brien.". In *Memorial Tributes: National Academy of Engineering, volume 7*. The National Academies Press, Washington, DC., 1994.

[5] E. Hecht. *Optics*. Addison Wesley Longman, Inc., 3rd edition, 1998.

[6] T. H Maiman. Stimulated optical radiation in ruby. *Nature*, 187:493–494, 1960.

[7] AT&T. Milestones in AT&T network history, 2011. url: http://www.corp.att.com/history/nethistory/milestones.html, accessed 12/12/11.

[8] J. Bland-Hawthorn and P. Kern. Astrophotonics: a new era for astronomical instruments. *Optics Express*, 17(3):1880–1884, 2009.

[9] J. López-Higuera. *Handbook of optical fibre sensing technology*. John Wiley and Sons, 2002.

[10] P. Urquhart. Review of rare earth doped fibre lasers and amplifiers. *IEE Proceedings*, 135(6):385–407, 1988.

[11] Fianium Ltd. url: http://www.fianium.com/, accessed 09/12/11.

[12] G. P. Agrawal. *Nonlinear fiber optics*. Academic Press, London, 4th edition, 2007.

[13] J. C. Knight, T. A. Birks, P. St. J. Russell, and D. M. Atkin. All-silica single-mode optical fiber with photonic crystal cladding. *Optics Letters*, 21(19):1547–1549, 1996.

[14] J. M. Senior. *Optical fiber communications: principles and practice*. Pearson Education Limited, Harlow, 3rd edition, 2009.

[15] B. J. Mangan, A. C. Muir, and J. C. Knight. Photonic bandgap fiber with multiple hollow cores. *Journal of Lightwave Technology*, 28(9):1287–1290, 2010.

[16] S Brustlein, P Berto, R Hostein, P Ferrand, C Billaudeau, D Marguet, A C Muir, J C Knight, and H Rigneault. Double-clad hollow core photonic crystal fiber for coherent Raman endoscope. *Optics Express*, 19(13):12562–12568, 2011.

[17] C. M. B. Cordeiro, E. M. dos Santos, and C. H. Brito Cruz. Side access to the holes of photonic crystal fibers - new sensing possibilities. In *Optical Fiber Sensors*, page ThE68. Optical Society of America, 2006.

[18] J. C. Travers, W. Chang, J. Nold, N. Y. Joly, and P. St. J. Russell. Ultrafast nonlinear optics in gas-filled hollow-core photonic crystal fibers [Invited]. *Journal of the Optical Society of America B*, 28(12), 2011.

[19] A. Bozolan, C. J. S. de Matos, C. M. B. Cordeiro, E. M. dos Santos, and J. Travers. Supercontinuum generation in a water-core photonic crystal fiber. *Optics Express*, 16(13):9671–9676, 2008.

[20] F. Benabid, J. C. Knight, and P. St. J. Russell. Particle levitation and guidance in hollow-core photonic crystal fiber. *Optics Express*, 10(21):1195–1203, 2002.

[21] M. K. Garbos, T. G. Euser, and P. St. J. Russell. Optofluidic immobility of particles trapped in liquid-filled hollow-core photonic crystal fiber. *Optics Express*, 19(20):19643–19652, 2011.

[22] W H Reeves. *Photonic crystal fibre : the ultra-flattened dispersion regime*. PhD thesis, University of Bath, 2003.

[23] H. Ebendorff-Heidepriem and T. M. Monro. Extrusion of complex preforms for microstructured optical fibers. *Optics Express*, 15(23):15086–15092, 2007.

[24] A.W. Snyder and J. D. Love. *Optical waveguide theory*. Chapman and Hall, New York, 1983.

[25] J. C. Knight. Photonic crystal fibres. *Nature*, 424(6950):847–851, 2003.

[26] T. A. Birks, J. C. Knight, and P. St. J. Russell. Endlessly single-mode photonic crystal fiber. *Optics Letters*, 22(13):961–963, 1997.

[27] J. C. Knight and W. J. Wadsworth. Silica fibres for supercontinuum generation. In J. M. Dudley and J. R. Taylor, editors, *Supercontinuum Generation in Optical Fibers*, chapter 5, pages 62–81. Cambridge University Press, 2010.

[28] K. L. Sala, G. A. Kenney-Wallace, and G. E. Hall. CW Autocorrelation Measurements of Picosecond Laser Pulses. *IEEE Journal of Quantum Electronics*, 16(9):990–996, 1980.

[29] L. G. Cohen, C. Lin, and W. G. French. Tailoring zero chromatic dispersion into the 1.5-1.6 μm low-loss spectral region of single-mode fibres. *Electronics Letters*, 15(12):334–335, 1979.

[30] J. K. Ranka, R. S. Windeler, and A. J. Stentz. Visible continuum generation in air silica microstructure optical fibers with anomalous dispersion at 800 nm. *Optics Letters*, 25(1):25–27, 2000.

[31] W. H. Reeves, J. C. Knight, P. St. J. Russell, and P. J. Roberts. Demonstration of ultra-flattened dispersion in photonic crystal fibers. *Optics Express*, 10(14):609–613, 2002.

[32] K. Saitoh and M. Koshiba. Empirical relations for simple design of photonic crystal fibers. *Optics Express*, 13(1):267–274, 2005.

[33] L. G. Cohen. Comparison of single-mode fiber dispersion measurement techniques. *Journal of Lightwave Technology*, 3(5):958–966, 1985.

[34] I. Gris-Sánchez, B. J. Mangan, and J. C. Knight. Reducing spectral attenuation in small-core photonic crystal fibers. *Optical Materials Express*, 1(2):179–184, 2011.

[35] T. P. White, B. T. Kuhlmey, R. C. McPhedran, D. Maystre, G. Renversez, C. M. de Sterke, and L. C. Botten. Multipole method for microstructured optical fibers. I. Formulation. *Journal of the Optical Society of America B*, 19(10):2322–2330, 2002.

[36] T. P. White, B. T. Kuhlmey, R. C. McPhedran, D. Maystre, G. Renversez, C. M. de Sterke, and L. C. Botten. Multipole method for microstructured optical fibers. I. Formulation: errata. *Journal of the Optical Society of America B*, 2003.

[37] H. Ademgil and S. Haxha. Design and optimisation of photonic crystal fibres for applications in communication systems. In *Proceedings of the World Congress on Engineering 2007*, volume I, 2007.

[38] P. St. J. Russell. Photonic crystal fibers. *Science*, 299:358–362, 2003.

[39] N. M. Litchinitser, S. C. Dunn, B. Usner, B. J. Eggleton, T. P. White, R. C. McPhedran, and C. M. de Sterke. Resonances in microstructured optical waveguides. *Optics Express*, 11(10):1243–1251, 2003.

[40] A. Ortigosa-Blanch, J. C. Knight, W. J. Wadsworth, J. Arriaga, B. J. Mangan, T. A. Birks, and P. St. J. Russell. Highly birefringent photonic crystal fibers. *Optics Letters*, 25(18):1325–1327, 2000.

[41] A. M. Weiner. *Ultrafast optics*. John Wiley and Sons, 2009.

[42] W. M. Tolles, J. W. Nibler, J. R. McDonald, and A. B. Harvey. A review of the theory and application of coherent anti-Stokes Raman spectroscopy (CARS). *Applied Spectroscopy*, 31(4):253–271, 1977.

[43] C. Kendall, J. Day, J. Hutchings, B. Smith, N. Shepherd, H. Barr, and N. Stone. Evaluation of Raman probe for oesophageal cancer diagnostics. *The Analyst*, 135(12):3038–3041, 2010.

[44] J. H. Lee, J. van Howe, C. Xu, and X. Liu. Soliton self-frequency shift: experimental demonstrations and applications. *IEEE Journal of Selected Topics in Quantum Electronics*, 14(3):713–723, 2008.

[45] R. R. Alfano and S. L. Shapiro. Emission in the region 4000 to 7000 $\AA$ via four-photon coupling in glass. *Physical Review Letters*, 24(11):584–588, 1970.

[46] R. R. Alfano and S. L. Shapiro. Observation of self-phase modulation and small-scale filaments in crystals and glasses. *Physical Review Letters*, 24(11):592–594, 1970.

[47] C. Lin and R. H. Stolen. New nanosecond continuum for excited-state spectroscopy. *Applied Physics Letters*, 28(4):216, 1976.

[48] R. H. Stolen, C. Lee, and R. K. Jain. Development of the stimulated Raman spectrum in single-mode silica fibers. *Journal of the Optical Society of America B*, 1(4):652–657, 1984.

[49] D. Mogilevtsev, T. A. Birks, and P. St. J. Russell. Group-velocity dispersion in photonic crystal fibers. *Optics Letters*, 23(21):1662–1664, 1998.

[50] S. Coen, A. H. L. Chau, R. Leonhardt, J. D. Harvey, J. C. Knight, W. J. Wadsworth, and P. St. J. Russell. White-light supercontinuum generation with 60-ps pump pulses in a photonic crystal fiber. *Optics Letters*, 26(17):1356–1358, 2001.

[51] J. M. Stone and J. C. Knight. Visibly "white" light generation in uniform photonic crystal fiber using a microchip laser. *Optics Express*, 16(4):2670–2675, 2008.

[52] A. K. Abeeluck, S. Radic, K. Brar, J.-C. Bouteiller, and C. Headley. Supercontinuum generation in a highly nonlinear fiber using a continuous wave pump. In *Optical Fiber Communication Conference*, page ThT1. Optical Society of America, 2003.

[53] T. A. Birks, W. J. Wadsworth, and P. St. J. Russell. Supercontinuum generation in tapered fibers. *Optics Letters*, 25(19):1415–1417, 2000.

[54] K. Tada and N. Karasawa. Broadband coherent anti-stokes raman scattering spectroscopy using a quasi-supercontinuum light source. In *Conference on Lasers and Electro-Optics*, page JTuD72. Optical Society of America, 2010.

[55] M. Ulman, D. W. Bailey, L. H. Acioli, F. G. Vallee, C. J. Stanton, E. P. Ippen, and J. G. Fujimoto. Femtosecond tunable nonlinear absorption spectroscopy in $Al_{0.1}Ga_{0.9}As$. *Physical Review B*, 47(16):10267–10278, 1993.

[56] H. Kano and H. Hamaguchi. Ultrabroadband (> 2500 cm^{-1}) multiplex coherent anti-Stokes Raman scattering microspectroscopy using a supercontinuum generated from a photonic crystal fiber. *Applied Physics Letters*, 86:121113, 2005.

[57] K. Isobe, A. Suda, M. Tanaka, H. Hashimoto, F. Kannari, H. Kawano, H. Mizuno, A. Miyawaki, and K. Midorikawa. Single-pulse coherent anti-Stokes Raman scattering microscopy employing an octave spanning pulse. *Optics Express*, 17(14):11259–11266, 2009.

[58] I. Hartl, X. D. Li, C. Chudoba, R. K. Ghanta, T. H. Ko, J. G. Fujimoto, J. K. Ranka, and R. S. Windeler. Ultrahigh-resolution optical coherence tomography using continuum generation in an air-silica microstructure optical fiber. *Optics Letters*, 26(9):608–610, 2001.

[59] A. M. Heidt, J. Rothhardt, A. Hartung, H. Bartelt, E. G. Rohwer, J. Limpert, and A. Tünnermann. High quality sub-two cycle pulses from compression of supercontinuum generated in all-normal dispersion photonic crystal fiber. *Optics Express*, 19(15):13873–13879, 2011.

[60] H. Tu, Y. Liu, D. Turchinovich, and S. A. Boppart. Compression of fiber supercontinuum pulses to the Fourier-limit in a high-numerical-aperture focus. *Optics Letters*, 36(12):2315–2317, 2011.

[61] H. Li, I. Pastirk, B. Xu, T. Gunaratne, and M. Dantus. Automated supercontinuum pulse compression from ultrafast fiber lasers using MIIPS. *OSA CLEO/QELS 2010*, 2010.

[62] J. M. Dudley and S. Coen. Fundamental limits to few-cycle pulse generation from compression of supercontinuum spectra generated in photonic crystal fiber. *Optics Express*, 12(11):2423–2428, 2004.

[63] B. Schenkel, R. Paschotta, and U. Keller. Pulse compression with supercontinuum generation in microstructure fibers. *Journal of the Optical Society of America B*, 22(3):687–693, 2005.

[64] L. E. Hooper, P. J. Mosley, A. C. Muir, W. J. Wadsworth, and J. C. Knight. Coherent supercontinuum generation in photonic crystal fiber with all-normal group velocity dispersion. *Optics Express*, 19(6):4902–4907, 2011.

[65] L. E. Hooper, P. J. Mosley, A. C. Muir, F. Yu, B. J. Mangan, W. J. Wadsworth, J. C. Knight, and J. M. Dudley. Coherent widely tunable source of sub-picosecond pulses using all-normal dispersion fiber supercontinuum. In *Fibre and Optical Passive Components (WFOPC), 2011 7th Workshop on*, pages 1 –4, 2011.

[66] Y. Takushima and K. Kikuchi. 10-GHz, over 20-channel multiwavelength pulse source by slicing super-continuum spectrum generated in normal-dispersion fiber. *IEEE Photonics Technology Letters*, 11(3):322–324, 1999.

[67] T. Udem, R. Holzwarth, and T. W. Hänsch. Optical frequency metrology. *Nature*, 416:233–237, 2002.

[68] S. A. Diddams, D. J. Jones, J. Ye, S. T. Cundiff, J. L. Hall, J. K. Ranka, R. S. Windeler, R. Holzwarth, T. Udem, and T. W. Hänsch. Direct link between microwave and optical frequencies with a 300 THz femtosecond laser comb. *Physical Review Letters*, 84(22):5102–5105, 2000.

[69] J. M. Dudley, G. Genty, and S. Coen. Supercontinuum generation in photonic crystal fiber. *Reviews of Modern Physics*, 78(4):1135–1184, 2006.

[70] K. J. Blow and D. Wood. Theoretical description of transient stimulated Raman scattering in optical fibers. *IEEE Journal of Quantum Electronics*, 25(12):2665–2673, 1989.

[71] B. Kibler, J. M. Dudley, and S. Coen. Supercontinuum generation and nonlinear pulse propagation in photonic crystal fiber: influence of the frequency-dependent effective mode area. *Applied Physics B*, 81:337–342, 2005.

[72] J. M Dudley and S. Coen. Coherence properties of supercontinuum spectra generated in photonic crystal and tapered optical fibers. *Optics Letters*, 27(13):1180–1182, 2002.

[73] M. Bellini and T. W. Hänsch. Phase-locked white-light continuum pulses: toward a universal optical frequency-comb synthesizer. *Optics Letters*, 25(14):1049–1051, 2000.

[74] X. Gu, M. Kimmel, A. P. Shreenath, R. Trebino, J. M Dudley, S. Coen, and R. S. Windeler. Experimental studies of the coherence of microstructure-fiber supercontinuum. *Optics Express*, 11(21):2697–2703, 2003.

[75] X. Gu, L. Xu, M. Kimmel, E. Zeek, P. O'Shea, A. P. Shreenath, R. Trebino, and R. S. Windeler. Frequency-resolved optical gating and single-shot spectral measurements reveal fine structure in microstructure-fiber continuum. *Optics Letters*, 27(13):1174–1176, 2002.

[76] F. Druon and P. Georges. Pulse-compression down to 20 fs using a photonic crystal fiber seeded by a diode-pumped Yb:SYS laser at 1070 nm. *Optics Express*, 12(15):3383–3396, 2004.

[77] G. McConnell. Confocal laser scanning fluorescence microscopy with a visible continuum source. *Optics Express*, 12(13):2844–2850, 2004.

[78] E. R. Andresen, H. N. Paulsen, V. Birkedal, J. Thøgersen, and S. R. Keiding. Broadband multiplex coherent anti-Stokes Raman scattering microscopy employing photonic-crystal fibers. *Journal of the Optical Society of America B*, 22(9):1934–1938, 2005.

[79] F. Lu and W. H. Knox. Generation of a broadband continuum with high spectral coherence in tapered single-mode optical fibers. *Optics Express*, 12(2):347–353, 2004.

[80] B. R. Washburn and N. R. Newbury. Phase, timing, and amplitude noise on supercontinua generated in microstructure fiber. *Optics Express*, 12(10):2166–2175, 2004.

[81] M. H. Frosz, P. Falk, and O. Bang. The role of the second zero-dispersion wavelength in generation of supercontinua and bright-bright soliton-pairs across the zero-dispersion wavelength. *Optics Express*, 13(16):6181–6192, 2005.

[82] M. L. V. Tse, P. Horak, F. Poletti, N. G. R. Broderick, J. H. Price, J. R. Hayes, and D.J. Richardson. Supercontinuum generation at 1.06 μm in holey fibers with dispersion flattened profiles. *Optics Express*, 14(10):4445–4451, 2006.

[83] K. M. Hilligsøe, T. V. Andersen, H. N. Paulsen, C. K. Nielsen, K. Mølmer, S. Keiding, R. Kristiansen, K. P. Hansen, and J. J. Larsen. Supercontinuum generation in a photonic crystal fiber with two zero dispersion wavelengths. *Optics Express*, 12(6):1045–1054, 2004.

[84] P. Falk, M. H. Frosz, and O. Bang. Supercontinuum generation in a photonic crystal fiber with two zero-dispersion wavelengths tapered to normal dispersion at all wavelengths. *Optics Express*, 13(19):7535–7540, 2005.

[85] M. Nakazawa. Coherence degradation in the process of supercontinuum generation in an optical Fiber. 4:215–223, 1998.

[86] N. Brauckmann, M. Kues, P. Groß, and C. Fallinch. Noise reduction of supercontinua via optical feedback. *Optics Express*, 19(16):14763–14778, 2011.

[87] N. Nishizawa and J. Takayanagi. Octave spanning high-quality supercontinuum generation in all-fiber system. *Journal of the Optical Society of America B*, 24(8):1786–1792, 2007.

[88] L. E. Hooper, P. J. Mosley, A. C. Muir, W. J. Wadsworth, and J. C. Knight. All-normal dispersion photonic crystal fiber for coherent supercontinuum generation. In *Conference on Lasers and Electro-Optics*, page CTuX4. Optical Society of America, 2010.

[89] A. M. Heidt. Pulse preserving flat-top supercontinuum generation in all-normal dispersion photonic crystal fibers. *Journal of the Optical Society of America B*, 27(3):550–559, 2010.

[90] NKT Photonics. NL-1050-NEG-1. url: http://nktphotonics.com/files/files/NL-1050-NEG-1-100409.pdf, accessed 02/01/12.

[91] H. Tu, Y. Liu, J. Lægsgaard, U. Sharma, M. Siegel, D. Kopf, and S. A. Boppart. Scalar generalized nonlinear Schrödinger equation-quantified continuum generation in an all-normal dispersion photonic crystal fiber for broadband coherent optical sources. *Optics Express*, 18(26):27872–27884, 2010.

[92] A. M. Heidt, A. Hartung, E. G. Rohwer, and H. Bartelt. Infrared, visible, and ultraviolet broadband coherent supercontinuum generation in all-normal dispersion fibers. In *2nd Workshop on Specialty Optical Fibers and Their Applications (WSOF-2), Proc. SPIE 7839, 78390X*, Oaxaca, Mexico, 2010.

[93] A. M. Heidt, A. Hartung, G. W. Bosman, P. Krok, E. G. Rohwer, H. Schwoerer, and H. Bartelt. Coherent octave spanning near-infrared and visible supercontinuum generation in all-normal dispersion photonic crystal fibers. *Optics Express*, 19(4):3774–3787, 2011.

[94] S. Demmler, J. Rothhardt, A. M. Heidt, A. Hartung, E. G. Rohwer, H. Bartelt, J. Limpert, and A. Tünnermann. Generation of high quality, 1.3 cycle pulses by active phase control of an octave spanning supercontinuum. *Optics Express*, 19(21):20151–20158, 2011.

[95] NKT Photonics. FemtoWHITE CARS supercontinuum device for coherent anti-Stokes Raman scattering. url: http://www.nktphotonics.com/files/files/FWCARS-090612.pdf, accessed 04/12/11.

[96] G. Humbert, W. J. Wadsworth, S. Leon-Saval, J. C. Knight, T. A. Birks, P. St. J. Russell, M. Lederer, D. Kopf, K. Wiesauer, E. I. Breuer, and D. Stifter. Supercontinuum generation system for optical coherence tomography based on tapered photonic crystal fibre. *Optics Express*, 14(4):1596–1603, 2006.

[97] R. L. Fork, O. E. Martinez, and J. P. Gordon. Negative dispersion using pairs of prisms. *Optics Letters*, 9(5):150–152, 1984.

[98] A. H. Zewail. Femtochemistry: Recent progress in studies of dynamics and control of reactions and their transition states. *The Journal of Physical Chemistry*, 100(31):12701–12724, 1996.

[99] A. V. Brakel, C. Grivas, M. N. Petrovich, and D. J. Richardson. Micro-channels machined in microstructured optical fibers by femtosecond laser. *Optics Express*, 15(14):8731–8736, 2007.

[100] F. Krausz and M. Ivanov. Attosecond physics. *Reviews of Modern Physics*, 81(1):163–234, 2009.

[101] G. Chang, T. B. Norris, and H. G. Winful. Optimization of supercontinuum generation in photonic crystal fibers for pulse compression. *Optics Letters*, 28(7):546–548, 2003.

[102] F. Gèrôme, P. Dupriez, J. Clowes, J. C. Knight, and W. J. Wadsworth. High power tunable femtosecond soliton source using hollow-core photonic bandgap fiber, and its use for frequency doubling. *Optics Express*, 16(4):2381–2386, 2008.

[103] D.T. Reid, M. Padgett, C. McGowan, W. E. Sleat, and W. Sibbett. Light-emitting diodes as measurement devices for femtosecond laser pulses. *Optics Letters*, 22(4):233–235, 1997.

[104] T. M. Fortier, A. Bartels, and S. A. Diddams. Octave-spanning Ti:sapphire laser with a repetition rate >1 GHz for optical frequency measurements and comparisons. *Optics Letters*, 31(7):1011–1013, 2006.

[105] J. Licea-Rodríguez, K. Garay-Palmett, and R. Rangel-Rojo. Soliton filtering from a supercontinuum: a tunable femtosecond pulse source. *Journal of Physics: Conference Series*, 274:012089, 2011.

[106] S. A. Dekker, A. C. Judge, R. Pant, I. Gris-Sánchez, J. C. Knight, C. M. de Sterke, and B. J. Eggleton. Highly-efficient, octave spanning soliton self-frequency shift using a specialized photonic crystal fiber with low OH loss. *Optics Express*, 19(18):17766–11773, 2011.

[107] P. J. Mosley, W. C. Huang, M. G. Welch, B. J. Mangan, W. J. Wadsworth, and J. C. Knight. Ultrashort pulse compression and delivery in a hollow-core photonic crystal fiber at 540 nm wavelength. *Optics Letters*, 35(21):3589–3591, 2010.

[108] M. P. Deboer and H. G. Muller. A systematic study of AC Stark shifts in xenon at super-high laser intensities. *Journal of Physics B: Atomic and Molecular Optical Physics*, 27:721–732, 1994.

[109] J. Palero, V. O. Boer, J. C. Vijverberg, H. C. Gerritsen, and H. J. C. M. Sterenborg. Short-wavelength two-photon excitation fluorescence microscopy of tryptophan with a photonic crystal fiber based light source. *Optics Express*, 13(14):5363–5368, 2005.

[110] T. Clausnitzer, J. Limpert, K. Zöllner, H. Zellmer, H.-J. Fuchs, E.-B. Kley, A. Tünnermann, M. Jupé, and D. Ristau. Highly efficient transmission gratings in fused silica for chirped-pulse amplification systems. *Applied Optics*, 42(34):6934–6938, 2003.

[111] G. Genty, M. Surakka, J. Turunen, and A. T. Friberg. Complete characterization of supercontinuum coherence. *Journal of the Optical Society of America B*, 28(9):2301–2309, 2011.

[112] G. Genty, M. Surakka, J. Turunen, and A. T. Friberg. Second-order coherence of supercontinuum light. *Optics Letters*, 35(18):3057–3059, 2010.

[113] K. L. Corwin, N. R. Newbury, J. M. Dudley, S. Coen, S. A. Diddams, K. Weber, and R. S. Windeler. Fundamental noise limitations to supercontinuum generation in microstructure fiber. *Physical Review Letters*, 90(11):1–4, 2003.

[114] T. M. Fortier, J. Ye, S. T. Cundiff, and R. S. Windeler. Nonlinear phase noise generated in air-silica microstructure fiber and its effect on carrier-envelope phase. *Optics Letters*, 27(6):445–447, 2002.

[115] F. Lu and W. H. Knox. Low noise wavelength conversion of femtosecond pulses with dispersion micro-managed holey fibers. *Optics Express*, 13(20):8172–8178, 2005.

[116] D. Türke, S. Pricking, A. Husakou, J. Teipel, J. Herrmann, and H. Giessen. Coherence of subsequent supercontinuum pulses generated in tapered fibers in the femtosecond regime. *Optics Express*, 15(5):2732–2741, 2007.

[117] I. Zeylikovich, V. Kartazaev, and R. R. Alfano. Spectral, temporal, and coherence properties of supercontinuum generation in microstructure fiber. *Journal of the Optical Society of America B*, 22(7):1453–1460, 2005.

[118] H. Tu, Y. Liu, X. Liu, D. Turchinovich, J. Lægsgaard, and S. A. Boppart. Nonlinear polarization dynamics in a weakly birefringent all-normal dispersion photonic crystal fiber: toward a practical coherent fiber supercontinuum laser. *Optics Express*, 20(2):1113–1128, 2012.

[119] H. Xu, J. Wu, K. Xu, Y. Dai, C. Xu, and J. Lin. Ultra-flattened chromatic dispersion control for circular photonic crystal fibers. *Journal of Optics*, 13:055405, 2011.

[120] J. M. Dudley, C. Finot, D. J. Richardson, and G. Millot. Self-similarity in ultrafast nonlinear optics. *Nature Physics*, 3:597–603, 2007.

[121] B. G. Bale, S. Boscolo, K. Hammani, and C. Finot. Effects of fourth-order fiber dispersion on ultrashort parabolic optical pulses in the normal dispersion regime. *Journal of the Optical Society of America B*, 28(9):2059–2065, 2011.